



**HAL**  
open science

# Contrôle et optimisation d'une expérience de condensation de Bose-Einstein

David Rey

► **To cite this version:**

David Rey. Contrôle et optimisation d'une expérience de condensation de Bose-Einstein. Mathematical Physics [math-ph]. Université Paris-Nord - Paris XIII, 2023. English. NNT : 2023PA131027 . tel-04382520

**HAL Id: tel-04382520**

**<https://theses.hal.science/tel-04382520v1>**

Submitted on 9 Jan 2024

**HAL** is a multi-disciplinary open access archive for the deposit and dissemination of scientific research documents, whether they are published or not. The documents may come from teaching and research institutions in France or abroad, or from public or private research centers.

L'archive ouverte pluridisciplinaire **HAL**, est destinée au dépôt et à la diffusion de documents scientifiques de niveau recherche, publiés ou non, émanant des établissements d'enseignement et de recherche français ou étrangers, des laboratoires publics ou privés.

UNIVERSITÉ SORBONNE PARIS NORD  
INSTITUT GALILÉE  
LABORATOIRE DE PHYSIQUE DES LASERS

Thèse présentée par

David Rey

Pour obtenir le grade de

Docteur de l'Université Sorbonne Paris Nord

Sujet :

Control and Optimization of a Bose-Einstein  
condensation experiment

Soutenue le 24 janvier 2023 devant le jury composé de :

Mme	Caroline CHAMPENOIS	Rapporteuse
M.	Vincent JOSSE	Rapporteur
Mme	Agnès MAÎTRE	Examinatrice
M.	Frédéric DU-BURCK	Examineur
Mme	Hélène PERRIN	Directrice de thèse
M.	Laurent LONGCHAMBON	Membre invité - co-encadrant



# Contents

<b>Acknowledgements</b>	<b>v</b>
<b>General Introduction</b>	<b>1</b>
<b>I State of the art and improvement</b>	<b>5</b>
<b>1 Elements of Bose-Einstein condensation in radiofrequency dressed trap.</b>	<b>7</b>
1.1 Trapping atoms with combined magnetic fields and RF fields . . . . .	7
1.1.1 An angular momentum coupled to a radiofrequency field . . . . .	8
1.1.2 The dressed quadrupole trap . . . . .	13
1.2 Elements of a Bose-Einstein condensate in an oblate trap . . . . .	19
1.2.1 Bose-Einstein condensation . . . . .	19
1.2.2 Quasi-2D regime . . . . .	24
<b>2 Experimental setup: the <math>^{87}\text{Rb}</math> BEC machine</b>	<b>27</b>
2.1 The laser cooling system . . . . .	27
2.1.1 The Rubidium and its magnetic sub-level . . . . .	27
2.1.2 The laser sources . . . . .	28
2.1.3 Magneto-optical traps . . . . .	29
2.2 Magnetic transport, trapping and Bose-Einstein condensate production . . . .	30
2.2.1 Transport: how and why? . . . . .	30
2.2.2 RF evaporative cooling in a magnetic quadrupole trap: 1 problem with 2 distinct solutions . . . . .	31
2.3 Radio-frequency fields and dressed trap loading . . . . .	33
2.4 Imaging the atomic cloud . . . . .	35
2.4.1 Horizontal imaging . . . . .	37
2.4.2 Vertical imaging . . . . .	37
2.4.3 Stern-Gerlach procedure . . . . .	37
2.4.4 Conclusion . . . . .	38

<b>3 Gravity compensation in the dressed quadrupole trap: spontaneous appearance of a ring-shaped BEC</b>	<b>39</b>
3.1 Gravity compensation mechanism and first results . . . . .	39
3.1.1 Gravity compensation mechanism . . . . .	39
3.1.2 Spontaneous formation of ring shaped Bose-Einstein condensate . . . . .	40
3.2 Experimental sequence and measurements . . . . .	41
3.2.1 Strategy and sequence description . . . . .	41
3.2.2 Calibration of the radiofrequency field . . . . .	43
3.2.3 Calibration of the magnetic gradient of the quadrupole trap . . . . .	46
3.3 Results exploitation . . . . .	48
3.3.1 Improved numerical model . . . . .	48
3.3.2 Comparison with analysis . . . . .	49
3.3.3 Slightly inhomogeneous ring . . . . .	52
3.4 Conclusion . . . . .	53
<b>II New control system and its applications</b>	<b>55</b>
<b>4 The control system: Implementation of the Labscript-Suite</b>	<b>57</b>
4.1 The new control system: Labscript-Suite . . . . .	58
4.1.1 General architecture . . . . .	58
4.1.2 Runmanager . . . . .	59
4.1.3 BLACS . . . . .	61
4.1.4 Lyse . . . . .	62
4.1.5 Runviewer . . . . .	64
4.2 Hardware control . . . . .	65
4.2.1 The clock . . . . .	66
4.2.2 Numerical and analog outputs . . . . .	67
4.2.3 Radio-frequency generation . . . . .	68
4.2.4 Camera workflow . . . . .	69
4.3 Adaptation of the software to our requirements . . . . .	69
4.3.1 Transcription of the sequence . . . . .	70
4.3.2 Data Analysis . . . . .	72
4.4 Conclusion and future improvements . . . . .	73
<b>5 Optimization of the experiment via machine-learning algorithms</b>	<b>75</b>
5.1 Implementation specificity . . . . .	75
5.1.1 M-LOOP and its interaction with the Labscript-Suite . . . . .	75
5.1.2 Construction of a cost to minimize . . . . .	77
5.2 Presentation of the algorithms . . . . .	78
5.2.1 Differential evolution . . . . .	78
5.2.2 Gaussian Process Regression . . . . .	79
5.3 Results obtained using machine-learning algorithms . . . . .	84
5.3.1 Transfer from the hybrid trap to the dressed trap: Identification of an important parameter . . . . .	84
5.3.2 Pre-transport phases: an optimization with numerous parameters . . . . .	87
5.4 Conclusion on machine learning uses . . . . .	90

**CONTENTS**

---

**iii**

**Conclusion**

**91**

**Bibliography**

**95**



# Acknowledgements

Tout d'abord, j'aimerais remercier H el ene Perrin pour avoir dirig e ma th ese. Sa disponibilit e ainsi que sa patience et son travail attentif et minutieux ont rendu ce travail possible malgr e un contexte sanitaire plus que troubl e. De m eme, merci  a Laurent Longchambon, mon co-encadrant, pour aide en salle d'exp erience et pour son  coute attentive qui aura assur ement rendu les heures de prises de mesures plus agr eables, ainsi que ces conseils p edagogiques qui m'ont  et e pr ecieux pour mes premiers pas en tant que charg e de TD.

J'adresse tous mes remerciements aux membres du jury qui me font l'honneur de lire et d' evaluer cette th ese. Je remercie Caroline Champenois et Vincent Josse pour avoir accept e d' etre les rapporteurs de mon manuscrit et Fr ed eric Du-Burck et Agn es Ma tre pour avoir accept e d' etre dans mon jury en tant qu'examinateur. Je souhaite adresser un remerciement particulier  a Agn es Ma tre qui m'a orient e vers l' equipe BEC et le LPL, et sans qui je n'aurais pas fait de th ese.

De m eme, les conseils avis es de Romain Dubessy ainsi que son aide pendant le changement de syst eme et les mesures prises pendant ces trois ann ees ont  et e d ecisives pour la mener  a bien de ces travaux. Je tiens  a lui adresser mes remerciements ainsi qu' a Thomas Badr pour sa disponibilit e et son aide sur l'exp erience. L'exp erience est maintenant entre les mains de Rishabh auquel je souhaite bon courage. Pour finir  a propos de l' equipe Condensat de Bose-Einstein, j'aimerais remercier Aur elien Perrin et Manon Ballu pour les discussions durant les repas et/ou les qui ont pour s ur rendu ces trois ann ees et quelques mois plus agr eables.

Ensuite j'aimerais remercier Maryse Medina, Carole Grangier, Alexandre Sourie et Bela id Na t-Sidnas pour leur disponibilit e et leur aide dans les d emarches administratives. De m eme, j'aimerais exprimer toute ma gratitude envers Alexandra L epine pour ton aide, son  coute et sa disponibilit e qui ont permis de r esoudre bien des probl emes.

La th ese a  et e aussi l'occasion de rencontr e de nombreuses personnes dans la vie quotidienne et je remercie Yanliang Guo pour son accueil sur la manip', Jo Seaward pour son accueil au sein de l' equipe et ses discussions autour d'un caf e. Je remercie aussi Simon Thomas pour ces discussions et son aide en salle d'exp erience. Les autres doctorants ont aussi aid e  a rendre la th ese plus agr eable et je remercie ainsi Pierre Bataille, Louis Lecordier, Karim Manamanni, Marylise Saffre, Anthony Dall'Agnol, Biplab Dutta, Nicolas Cahuzac, Andr ea Litvinov, Ali Beydoune, Julien Lecoffre, Charles Garcion et les autres doctorants du laboratoire. Pour finir, j'aimerais dire un immense merci  a Tatiana Steshchenko pour son  coute et sa bienveillance durant la r edaction qui ont  et e d'un grand aide!

Merci  a mes amis hors du laboratoire : Thibault, pour nos discussions, son aide, ses



conseils avisés et ses recommandations jeux vidéo que je vais (enfin !) pouvoir découvrir. À mes amis de lycée pour leur discussion durant le confinement et les moments inoubliables en vacances quand les conditions le permettaient, je remercie Aline, Alexandra, Sam, Lee, Luc, Alexandre, Victor, Solène et Maxime. Je remercie aussi Camille et Pierre pour leurs conseils et les échanges durant ces trois dernières années. Et enfin, merci à Marianna et Jean-Philippe pour les moments qu'on a pu partager.

Enfin, la thèse est un exercice absorbant et pouvoir sortir la tête de l'eau est nécessaire. À ce titre, je remercie ma compagne Axelle pour son aide, ces conseils avisés et le soutien psychologique pendant ces trois dernières années. Ma famille m'a aussi permis de pouvoir de m'aérer l'esprit (et de me nourrir) et à ce titre je remercie ma soeur Diane, mon frère Dante, mon père Jean-Michel, ma mère Myriam, ma grand-mère Violette et mon grand-père Michel.

# General Introduction

Bose-Einstein condensation is a particular state of matter due to the quantum nature of particles. It arises when a system of bosonic particles reaches a temperature threshold below which a macroscopic fraction of the ensemble shares the same quantum ground-state wavefunction. This fraction is called the Bose-Einstein condensate (BEC). First predicted by Bose and Einstein as a direct consequence of quantum statistics [1,2], Bose-Einstein condensation was soon after proposed to be at the origin of two spectacular effects displaying a temperature threshold: the flow without friction of liquid helium and the cancellation of the electrical resistivity of some metals.

The former phenomenon, called superfluidity, was first observed in 1938 by Kapitza [3], Allen and Misener [4] simultaneously. That same year, London [5] used the BEC model to explain the superfluidity of liquid bosonic  $^4\text{He}$  and to describe some of its transport properties.

The latter, superconductivity, was discovered by Kamerlingh Onnes in 1911 [6], and it took longer to build a satisfactory quantum theory by Bardeen, Cooper, and Schrieffer in 1957 [7]. In the BCS theory, superconductivity arises from the Bose-Einstein condensation of bosonic pairs of conduction electrons.

Even if Bose-Einstein condensation is at the core of superfluidity and superconductivity, it is difficult to test the seminal BEC theory from their experimental study. Indeed, this theory was describing the behavior of noninteracting bosons like photons, a situation very different from the one encountered in a liquid or a solid. This is the reason why a sustained theoretical and experimental effort has been developed in order to produce a dilute Bose-Einstein condensate. In such a BEC, the effect of the interactions is weak and well described. Bogolyubov in 1947 proposed a semi-classical description of this situation, followed by a mean-field theory by Gross and Pitaevskii [2].

It is during the 1980s that the techniques for trapping and cooling atoms were developed. Magneto-optical traps combine radiation pressure and Doppler cooling [8–10] to simultaneously trap and cool atoms, which are later transferred to a conservative trap, usually magnetic or optical or a combination of the two. The last step is evaporative cooling [11], where the phase-space density of the sample is increased by the selective removal of the most energetic atoms.

First motivated by the quest for polarized hydrogen condensation, these techniques eventually led to the first experimental evidence of Bose-Einstein condensation in a trapped gas of alkali atoms [12, 13].

This achievement allowed to accurately study superfluidity via the observation of vortices of quantized circulation [14, 15] and the observation of a critical velocity for frictionless motion [16]. The confirmation of the Berezinskii-Kosterlitz-Thouless mechanism [17, 18] for superfluidity in a two-dimensional BEC [19] also illustrates the potential of dilute gases for fundamental studies. Indeed, in cold atoms experiments, the environment of the system is well controlled; for example, the trap parameters and the collisional properties can be known or controlled with high accuracy. It allows to compare quantitatively experimental results to the underlying quantum theory; for example the mean-field approach of Gross and Pitaevskii explains very well many properties of the condensate. [2].

This high degree of control also makes cold atomic systems the ideal platforms to perform what is called quantum simulation [20]. In this situation, the cold atom experiment is a controlled system simulating a given Hamiltonian, which is usually very difficult to compute. A particular measurement in the system gives the result of the simulation. For example, one can place a BEC in an optical lattice [21]: the Hamiltonian of the system is the Bose-Hubbard Hamiltonian, the same which approximates the situation of Cooper pairs in a superconducting system. Other quantum systems that can be studied are dipolar gases with anisotropic interactions [22], where one can create a supersolid [23], an exotic state of matter. Other many-body phenomena in condensed matter could benefit from cold atoms experiments, like the study of the quantum Hall effect [24]. Another recently developing field of research is atomtronics [25], where one builds circuits of ultracold atoms in order to perform the equivalent of electronic circuits, but with phase-coherent particles instead of electrons. Such devices enable, for example, to build an atomic equivalent of a SQUID with a BEC [26]: where the magnetic flux sensitivity is replaced by rotation rate detection.

Recently, there has been a renewed interest in the cold atom community for the properties of a superfluid spread at the surface of an hollow spheroid [27]. In the case of a BEC in such a trap, the collective modes have been theoretically studied, and their modifications at the transition between a hollow and a conventional topology characterized [28]. The curvature of the trap and the topology should lead to qualitatively different behavior of the quantized vortices associated with rotation: pairs of vortices at polar-opposite points should only exist, and their dynamics should be affected by the local curvature [29]. This topology has not been experimentally achieved yet for a BEC because in such traps on Earth, gravity usually pulls the atoms down, preventing them from occupying the whole space available. To circumvent this effect, one can take advantage of a microgravity environment; this is the case for the Cold Atom Laboratory on board the International Space Station, where an experiment which successfully condensed rubidium atoms [30] has been launched.

In the Bose-Einstein condensation experiment at the LPL, a BEC is studied under gravity in a hollow trap made of an adiabatic RF-dressed shell trap [31]. In such a trap, the atoms are put into a static quadrupolar magnetic field and coupled to a radiofrequency field, resulting in a bubble-shaped trap oblate along the vertical axis [32, 33]. Because of gravity, the BEC is located at the bottom of the shell, strongly flattened in the vertical direction. If the vertical confinement is strong enough, only the ground state of the vertical harmonic oscillator is populated, and the Bose-Einstein condensate enters a special regime called quasi-2D. In this regime, the LPL group has studied collective excitations of the BEC [34] and was able to see the onset of the quasi-2D regime via the modification of the monopole mode frequency [32]. They also studied in this regime a type of mode particular to superfluids, the scissors mode [35], and were able to observe a local transition from normal to superfluid via

the scissors mode's frequency modification and link the transition to the BKT theory. Using a rotating deformation of the trap, they were able to impart rotation to the BEC up to 18 times the superfluid critical velocity [36]. At such speed, the centrifugal force makes the atoms climb up the walls of the shell until they form a ring; in that situation, the atoms ventured for the first time out of the trap bottom. This was made possible by two very interesting features of the dressed trap: its smoothness and the very good control of its rotational invariance. In addition, a vertical force from the RF coupling is always present in the trap, usually smaller than gravity, and can be increased either by reducing the size of the bubble, or by increasing the amplitude of the RF field. This led the group to propose a scheme to compensate for gravity in the shell trap on Earth in the laboratory [37].

All these studies required the accumulation of a series of data in the form of pictures of the atomic cloud. These pictures are analyzed to extract the relevant physical parameters, which are usually the number of atoms, the temperature of the sample, the center-of-mass position, or the shape of the cloud. The number of images in the series varies from tens to hundreds, especially if one has to perform statistics on the data.

Therefore, in order to accumulate enough data per day, it is useful to automatize as much as possible the experimental process, especially because a single experimental run lasts typically one minute. The programming and control of an experimental sequence are done by a computer, which ensures the communication with the different devices in the laboratory. At first, the different teams developed their own internal control systems. The BEC team at LPL has, for example, used since the first experimental setups a C++ software written by Jakob Reichel. It allowed to perform all the experiments cited above but could only work on out-of-date hardware and was eventually lacking in versatility. Meanwhile, other experimental teams put a strong effort into developing very complete software for cold atom experiments, incorporating data analysis framework [38], and some of these projects have been distributed [39, 40]. The BEC team decided to choose one of them for their new experiment control system.

One has to recall that cold atom experiments are complex ones, and the optimization of all the parameters is a long process, and a new feature in these recent projects is that they allow for machine-learning based optimization. These algorithms are used in different scientific communities such as quantum information [41, 42], cosmology [43–45], and even in medical studies to detect pathologies [46]. For example, in the evaporative cooling phase, one has to set the radio frequency ramp by maximizing the phase-space density of the cloud in the trap, using a trial-and-error procedure. In order to have an automatic determination of the best ramp signal, physicists started to use machine-learning algorithms to optimize all kinds of processes in experiments [47–49] such as the size of the cloud in a magneto-optical trap or the image analysis [50, 51]. The first algorithms used were simple genetic algorithms, which aim at mimicking the natural selection process [52] but more complex ones have been used, like Gaussian process regression or neural networks [53].

There have been three axes treated during my time as a PhD student. I have implemented the new control system on the experiment, and tested the optimization of some phases in the sequence with machine learning, along with the experimental study of gravity compensation in the shell trap. The study of gravity compensation in the dressed-quadrupole trap is the conclusion of the experimental investigation started during Yanliang Guo's PhD. The experimental sequence had been rethought and led to systematic studies on the different intermediate stages of gravity compensation. In parallel, a fully numerical model has been developed to

be compared to the experimental results. For the change of the control system, all the functionalities of the former system have been re-implemented in order to take advantage of the features of the new control system, including the easy implementation of machine-learning algorithms in order to perform automatic optimization.

The document is divided into five chapters :

- Chapter 1 provides the reader with a description of the system studied in this thesis. Firstly, the dressed trap used in the experimental setup is described, and its geometrical properties are detailed. Secondly, elements of Bose-Einstein condensation are given, including the specificity of the quasi two-dimensional regime.
- Chapter 2 describes the experimental setup and the sequence needed to achieve Bose-Einstein condensation in the dressed trap. It begins with a reminder of the properties of the rubidium atom and the lasers needed to cool it down. Then the cooling procedure is described, along with the necessary equipment. Ultimately, the imaging system is described.
- Chapter 3 describes the experimental work on gravity compensation. It starts with a description of the mechanism that allows to cancel the effect of gravity in the dressed quadrupole trap. Then the experimental sequence is described, with a particular emphasis on the fine tuning of the RF polarization to obtain the most rotationally symmetric trap possible. The ring shaped form of the condensate that appears when gravity is overcompensated is explained by the zero-energy point of the transverse confinement, and a comparison of the observations with an improved numerical model is given.
- Chapter 4 is dedicated to the presentation of the Labscript suite, the new control system installed on the experiment. It begins with the introduction of the four different pieces of software in the suite. Then the interaction between the different devices and the control system is detailed. This is followed by a description of the implementation of the Labscript Suite. This chapter ends with a list of proposals for future improvements to the new control system.
- The final chapter 5 describes the use of machine-learning algorithms in the experimental sequence. It starts by explaining how the algorithms are implemented, and the construction of the cost to optimize is detailed. The different algorithms used are presented, and the different optimization attempts done during the PhD are detailed and analyzed.

## Part I

# State of the art and improvement



# Chapter 1

## Elements of Bose-Einstein condensation in radiofrequency dressed trap.

This first chapter aims at giving a brief description of the fundamental physics motivating the experimental work done in this thesis. There are two distinct elements to introduce: first, the trapping of atoms in an adiabatic potential using a radio frequency field, and second, a description of the Bose-Einstein condensation. These two notions will be introduced in this order.

To start, the RF-induced adiabatic trapping of atoms provides a highly versatile trap for atoms: the principle is to couple Zeeman substates in a magnetic field. This creates an avoided crossing, hence trapping the atoms on an isomagnetic surface. It was proposed in 2001 by O. Zobay and B. M. Garraway [54] and the first implementation in the LPL group dates back to 2003 [55]. By controlling both the magnetic and radiofrequency fields, one can access different types of geometry, such as a double well [56], a ring-shape [57, 58], and a lattice [59, 60], to name a few. This part of the chapter closely follows Ref. [61]. A presentation of the quadrupole dressed trap used on the experimental work of the thesis will be presented. A reader willing to know more about this trapping technique is encouraged to read Ref. [33].

As the experiment does not trap only one atom but a collection of atoms at low temperatures, a description of the Bose-Einstein condensation [2] will be presented. It will start by describing the Bose-Einstein condensation. As the experiment conducted for this thesis was done in a quasi-2D system, the last section of this chapter will be dedicated to this regime.

### 1.1 Trapping atoms with combined magnetic fields and RF fields

The specificity of the experimental setup is the ability to trap atoms using a static magnetic field and a radio-frequency field. This section aims at describing the principle of this interaction. The question is: How to trap atoms at a position chosen by the experimentalist using a static magnetic field and an oscillating magnetic field?



### 1.1.1 An angular momentum coupled to a radiofrequency field

In this part, a brief description of the principle of this trap will be given. To start, there is a static magnetic field along the  $z$ -axis  $\mathbf{B}_0(r) = B_0(\mathbf{r})\mathbf{e}_z$ , by definition of the  $z$ -axis (chosen along the field).

#### Atoms in a static magnetic field

The first step to describing the behavior of atoms in our trap is to describe the interaction between the atom and a magnetic field. Let us consider an atom having a total angular momentum  $F$  immersed in a static magnetic field. The total angular momentum is an operator noted  $\hat{\mathbf{F}}$ , and represents the sum of the nuclear angular momentum, the orbital angular momentum, and the electronic spin. The quantization axis is given by the direction of the field. There exists a basis where both the modulus square of  $\mathbf{F}$ , noted  $\hat{F}^2$ , and the projection of  $\mathbf{F}$  along the  $\mathbf{e}_z$ , noted  $\hat{F}_z$  are diagonal. This basis represents the eigenstates of our system with eigenvalues:

$$\hat{F}_z |F, m_F\rangle = m_F \hbar |F, m_F\rangle \quad \hat{F}^2 |F, m_F\rangle = \hbar^2 F(F+1) |F, m_F\rangle \quad (1.1)$$

Where  $F$  is the quantum number associated to  $\hat{F}^2$  and  $m_F$  is the quantum number associated to  $\hat{F}_z$  which is the spin projection on the  $z$ -axis, and  $m_F \in \{-F, -F+1, \dots, F-1, F\}$ . The energy of the interaction between the spin and the magnetic field is formalized by the following Hamiltonian:

$$\hat{H}_0 = \frac{g_F \mu_B}{\hbar} \mathbf{B}_0 \cdot \hat{\mathbf{F}} = \frac{g_F \mu_B}{\hbar} B_0(\mathbf{r}) \hat{F}_z \quad (1.2)$$

In this expression,  $g_F$  is the Landé factor of the state, and  $\mu_B$  is the Bohr magneton. The eigenstates of this Hamiltonian are called Zeeman states and are the  $|F, m_F\rangle$  formalised previously. The eigenenergy associated with this state is given by:

$$E_{m_F} = m_F g_F \mu_B B_0(\mathbf{r}) \quad (1.3)$$

As  $m_F$  and  $g_F$  can both be positive or negative, the eigenenergies of each state can be either positive or negative. In order to make the distinction more visible, we introduce the parameter  $s = \frac{g_F}{|g_F|}$ , which represents the sign of the Landé factor. The energy of the states can be rewritten as  $E_{m_F} = s m_F \hbar \omega_0$  where  $\omega_0$  is the Larmor frequency and is given by  $\omega_0 = \frac{|g_F| \mu_B B_0}{\hbar}$  and describes the spacing between Zeeman levels.

For the rubidium in the setup, we are in the situation where  $s = -1$  and  $F = 1$ . This leads to the states  $|m_F\rangle$  characterized by  $m_F < 0$  attracted to regions where there is a minimum of the magnetic field. In that case, we talk about "low-field seeking states". On the contrary, when  $m_F > 0$ , the atom is attracted to the regions with the greatest magnetic field, which are referred to as "high-field seeking states." But Wing's theorem stipulates that no maximum magnetic field exists in free-space [62]. That's why we trapped the atoms in a low-field seeking state.

#### Radiofrequency field

In addition to the static magnetic field, an oscillating magnetic field is shone onto the atoms. A classical description of the oscillating magnetic field is given by:

$$\mathbf{B}(t) = B_x \cos(\omega_{\text{rf}} t + \phi_x) \mathbf{e}_x + B_y \cos(\omega_{\text{rf}} t + \phi_y) \mathbf{e}_y + B_z \cos(\omega_{\text{rf}} t + \phi_z) \mathbf{e}_z \quad (1.4)$$

This is an expression using real numbers, but using complex numbers is more convenient. In such a case, the expression becomes  $\mathbf{B}(t) = \mathcal{B}_1 e^{-i\omega_{\text{rf}}t} \boldsymbol{\epsilon} + c.c.$ , where  $\boldsymbol{\epsilon}$  represents the RF field's complex polarization and  $\mathcal{B}_1$  its complex amplitude. The vector  $\boldsymbol{\epsilon}$  norm is equal to 1. Furthermore, the goal of these formulae is to describe the coupling between the RF-field and the atom in our trap, and the usual basis  $(\mathbf{e}_x, \mathbf{e}_y, \mathbf{e}_z)$  is inconvenient. We prefer to use the spherical basis instead, noted  $(\mathbf{e}_+, \mathbf{e}_-, \mathbf{e}_z)$ , where:

$$\mathbf{e}_+ = -\frac{1}{\sqrt{2}}(\mathbf{e}_x + i\mathbf{e}_y) \quad \mathbf{e}_- = \frac{1}{\sqrt{2}}(\mathbf{e}_x - i\mathbf{e}_y) \quad (1.5)$$

It should be remembered that in our example, the static field is along the  $z$ -axis and provided that  $B_z \ll B_0$ , the effect of the RF field along  $z$  is negligible [33]. Hence, only the radiofrequency field in the plane orthogonal to the  $z$ -axis is considered. The expression of  $B_0$  in the spherical basis using complex amplitude is given by:

$$\mathcal{B}_1 \boldsymbol{\epsilon} = B_+ \mathbf{e}_+ + B_- \mathbf{e}_- \quad (1.6)$$

Where  $B_{\pm} = \mathbf{e}_{\pm}^* \cdot \boldsymbol{\epsilon} \mathcal{B}_1 = \frac{1}{2\sqrt{2}}(\mp B_x e^{-i\phi_x} + i B_y e^{-i\phi_y})$ . When projecting  $\hat{\mathbf{F}}$  on the spherical basis, we obtain:

$$\hat{\mathbf{F}} \cdot \mathbf{e}_{\pm} = \mp \frac{1}{\sqrt{2}} \hat{\mathbf{F}}_{\pm} \quad (1.7)$$

With  $\hat{\mathbf{F}}_+$  as the raising operator and  $\hat{\mathbf{F}}_-$  as the lowering operator. These expressions using the Cartesian basis are:  $\hat{\mathbf{F}}_{\pm} = \hat{\mathbf{F}}_x \pm i\hat{\mathbf{F}}_y$ .

### Coupling between atoms and the radiofrequency field

Now that we have a description of the RF fields, one must describe the coupling between the RF field and the angular momentum of the atom. Because the rf-field is an oscillating magnetic field, the expression (1.2) holds true, and thus:

$$\hat{V}_1 = \frac{s|g_F|\mu_B}{\hbar} \mathcal{B}_1 \boldsymbol{\epsilon} \cdot \hat{\mathbf{F}} e^{-i\omega_{\text{rf}}t} + h.c. \quad (1.8)$$

When writing the field on a spherical basis, we ignored the component of the magnetic field along the  $z$ -axis. This leads us to a new expression of the coupling terms using the ladder operators  $\hat{\mathbf{F}}_{\pm}$ :

$$\begin{aligned} \hat{V}_1 &= s \frac{|g_F|\mu_B}{\hbar} \left[ -\frac{1}{\sqrt{2}} B_+ \hat{\mathbf{F}}_+ + \frac{1}{\sqrt{2}} B_- \hat{\mathbf{F}}_- \right] e^{-i\omega_{\text{rf}}t} + h.c. \\ &= s \left[ \frac{\Omega_+}{2} \hat{\mathbf{F}}_+ e^{-i\omega_{\text{rf}}t} + \frac{\Omega_-}{2} \hat{\mathbf{F}}_- e^{-i\omega_{\text{rf}}t} + \frac{\Omega_+^*}{2} \hat{\mathbf{F}}_- e^{i\omega_{\text{rf}}t} + \frac{\Omega_-^*}{2} \hat{\mathbf{F}}_+ e^{i\omega_{\text{rf}}t} \right] \end{aligned} \quad (1.9)$$

Where  $\Omega_{\pm} = \mp \sqrt{2} \frac{|g_F|\mu_B}{\hbar} B_{\pm}$  represents the complex coupling amplitude. These terms couple the different Zeeman sub-states  $|m_F\rangle$ .

The total Hamiltonian of the system is given by a total of two contributions: the first comes from the atom levels, and the second term describes the way the field and the atom interact with one another:

$$\hat{H} = s\omega_0 \hat{\mathbf{F}}_z + s \left[ \frac{\Omega_+}{2} \hat{\mathbf{F}}_+ e^{-i\omega_{\text{rf}}t} + \frac{\Omega_-}{2} \hat{\mathbf{F}}_- e^{-i\omega_{\text{rf}}t} + \frac{\Omega_+^*}{2} \hat{\mathbf{F}}_- e^{i\omega_{\text{rf}}t} + \frac{\Omega_-^*}{2} \hat{\mathbf{F}}_+ e^{i\omega_{\text{rf}}t} \right] \quad (1.10)$$

Another point of view is that the first term of the Hamiltonian corresponds to a precession of  $\hat{F}$  around the  $z$ -axis, and all the terms in square brackets represent all the different couplings between the Zeeman substates and the RF field. In order to go further, one needs to see that the Hamiltonian in (1.10) is time-dependent with rotating terms. The expression (1.10) is set in the lab frame, which is at rest, and this does not seem practical. The oscillating terms will introduce time dependencies, and it will be of great help to find a formulation that is time-independent. Hence, changing the system to a rotating frame depends on:

- $s$  - the sign of the rotation will be dictated by the sign of the Landé factor.
- $\omega_{\text{rf}}$  - the important frequency one should consider is the RF-field frequency at which the atom is in resonance with.

This corresponds to the following transformation:

$$|\psi\rangle_{\text{rot}} = \hat{R}_z(s\omega_{\text{rf}}t) |\psi\rangle = \exp\left(-i\frac{s\omega_{\text{rf}}t}{\hbar}\hat{F}_z\right) |\psi\rangle \quad (1.11)$$

Where  $\hat{R}_z(s\omega_{\text{rf}}t) = \exp\left(-i\frac{s\omega_{\text{rf}}t}{\hbar}\hat{F}_z\right)$  denotes the rotation corresponding to the transition from the laboratory frame to the rotating frame around the  $z$ -axis at a frequency  $\omega_{\text{rf}}$ . This transformation had to be considered in the system's time evolution. Therefore, the Schrödinger equation giving the time evolution of the system is written as:

$$i\hbar\partial_t(|\psi\rangle) = -i\hbar\hat{R}^\dagger[\partial_t\hat{R}]|\psi\rangle + \hat{R}^\dagger\hat{H}\hat{R}|\psi\rangle = \hat{H}_{\text{eff}}|\psi\rangle \quad (1.12)$$

In this basis, we have to introduce the detuning given by  $\delta = \omega_{\text{rf}} - \omega_0$ . The effective Hamiltonian now reads:

$$\begin{aligned} \hat{H}_{\text{eff}} = -s\delta\hat{F}_z + s\left[\frac{\Omega_+}{2}e^{i(s-1)\omega_{\text{rf}}t}\hat{F}_+ + \frac{\Omega_+^*}{2}e^{-i(s-1)\omega_{\text{rf}}t}\hat{F}_-\right] \\ + s\left[\frac{\Omega_-}{2}e^{-i(s+1)\omega_{\text{rf}}t}\hat{F}_- + \frac{\Omega_-^*}{2}e^{i(s+1)\omega_{\text{rf}}t}\hat{F}_+\right] \end{aligned} \quad (1.13)$$

Regardless of the sign of  $s$ , the behavior will always be the same: there are two coupling terms that don't oscillate in the new frame; these terms are said to be resonant, and the two remaining terms that oscillate at  $\pm 2\omega_{\text{rf}}$ ; known as the oscillating terms. Because the oscillating terms are almost averaged out to 0, we neglect them. This leads us to consider a time scale of order  $\sqrt{\delta^2 + \Omega^2}$ , and this approximation, called the rotating wave approximation, is valid as long as  $\sqrt{\delta^2 + \Omega^2} \ll \omega_{\text{rf}}$ . When this approximation is applied, only two terms remain. Their coupling strengths are  $\Omega_s = \Omega_1$  and  $\Omega_1 = -\frac{\sqrt{2}g_F\mu_B\mathcal{B}_1}{\hbar}$ , resulting in the effective Hamiltonian being:

$$\hat{H}_{\text{eff}} = -s\delta\hat{F}_z + s\frac{\Omega_1}{2}[\hat{F}_+ + \hat{F}_-] = -s\delta\hat{F}_z + s\Omega_1\hat{F}_x = s\sqrt{\delta^2 + \Omega_1^2}\hat{F} \cdot \mathbf{u} \quad (1.14)$$

This corresponds to the Hamiltonian of a particle with angular momentum  $\hat{F}$  coupled to an effective magnetic field  $\mathbf{B}_{\text{eff}} = \frac{\hbar\sqrt{\delta^2 + \Omega_1^2}}{g_S\mu_B}\mathbf{u}_\theta$ . The unitary vector  $\mathbf{u}_\theta$  is given by:

$$\mathbf{u} = \cos(\theta)\mathbf{e}_z + \sin(\theta)\mathbf{e}_x \quad \cos(\theta) = \frac{-\delta}{\sqrt{\delta^2 + \Omega_1^2}} \quad \sin(\theta) = \frac{\Omega_1}{\sqrt{\delta^2 + \Omega_1^2}} \quad (1.15)$$

This expression corresponds to a rotation of angle  $\theta$  around the  $y$ -axis. So the  $\hat{H}_{\text{eff}}$  has its eigenstates  $|\psi'\rangle = \hat{R}_y(\theta) |m_F\rangle$  with the eigenenergies  $E_{m_F} = m_F \hbar \sqrt{\delta^2 + \Omega_1^2}$ . This is the dressed potential seen by the atoms in our trap.

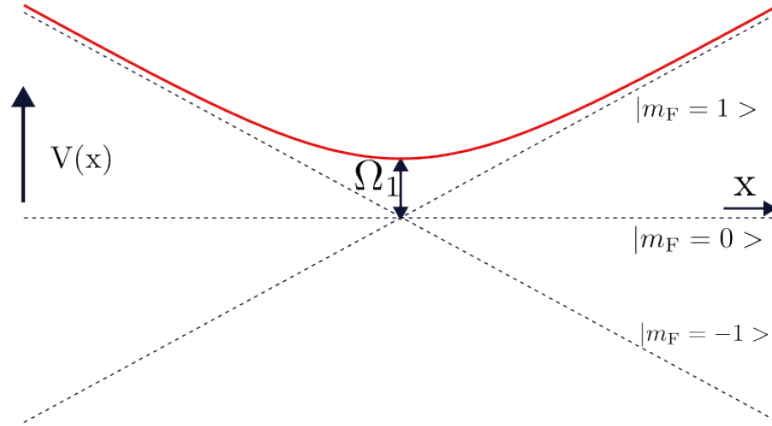


**Figure 1.1** – Representation of the upper dressed state  $F = 1$  (red solid line) and the bare states (black dashed line).

As shown in Fig.1.1, there is a geometrical interpretation of the different terms presented previously. At first, the minimum of potential for the dressed state is located where the coupling is resonant with the RF-field, i.e., where  $\omega_0 = \omega_{\text{rf}}$ . Also, the term  $\Omega_1$  gives the spacing between two dressed states when the coupling is resonant, as indicated in the scheme. Finally, the detuning has a special role: when the detuning is positive, the upper dressed eigenstate is almost the Zeeman state  $|m_F = 1\rangle$ , whereas when the detuning is negative, the eigenstate is almost  $|m_F = -1\rangle$ . One of the rf-field effects on the atom is to flip its angular momentum when it crosses the resonance. This observation will be used when talking about the dressed trap loading in Chap.2.

### Adiabaticity condition

The principle behind the potential studied in this thesis has been set, but one has to be careful because the atoms can move inside the trap and trapping is not homogeneous. In order to simplify our problem, we will look at an atom with  $F = \frac{1}{2}$ , that is, a two level system. This gives the following effective Hamiltonian:

$$\hat{H}_{\text{eff}} = \begin{pmatrix} -\delta(\mathbf{r}) & \Omega_1(\mathbf{r}) \\ \Omega_1(\mathbf{r}) & \delta(\mathbf{r}) \end{pmatrix} \quad (1.16)$$

The description of an atom in a space-dependent system can quickly become mathematically heavy as the position and momentum operators don't commute. We will restrict our study to a semi-classical model. We first have to give some elements of the situation in the trap:

- The atoms are point-like :  $\mathbf{r} = \langle \hat{R} \rangle$  and  $\Delta \mathbf{R} = 0$ .
- $\delta$  and  $\Omega_1$  depends only on space.

- The motion of an atom is done at constant velocity inside the trap, therefore it leads to  $\mathbf{r}(t) = \mathbf{v}t$

The consequence of these statements is that we pass from a problem dependent on  $\mathbf{r}$  to a problem that only depends on time:

$$\hat{H}_{\text{eff}} = \frac{\hbar}{2} \begin{pmatrix} -\delta(t) & \Omega_1(t) \\ \Omega_1(t) & \delta(t) \end{pmatrix} \quad (1.17)$$

Now, for a given time, the Hamiltonian can be diagonalized with a unitary  $\hat{U}(t)$ , and this becomes:

$$\hat{H}_A = \frac{\hbar}{2} \begin{pmatrix} \lambda(t) & 0 \\ 0 & -\lambda(t) \end{pmatrix} = \hat{U}^\dagger(t) \hat{H} \hat{U}(t) \quad (1.18)$$

Where the  $\frac{\hbar}{2}\lambda$  are the eigenenergies, which are now time-dependent. To know the dynamics of the system, we start with the Schrödinger equation:

$$i\hbar \frac{\partial}{\partial t} \Psi(t) = \hat{H}_A \Psi(t) \quad (1.19)$$

With  $\Psi$  being the state of the atom. However, the most convenient formulation would be to use the time-dependent yet diagonal basis of the  $\hat{H}_A$  operator. In this basis, the expression of the state becomes  $\Psi(t) = \hat{U}(t) \Psi_A(t)$ , the Hamiltonian is given by  $\hat{H}_{\text{eff}} = \hat{U}(t) \hat{H}_A \hat{U}^\dagger(t)$ , and to express the Schrödinger's equation in this new basis gives us following expression:

$$i\hbar \frac{\partial}{\partial t} \Psi_A(t) = \hat{H}_A \Psi_A(t) + i\hbar \frac{\partial \hat{U}^\dagger}{\partial t} \hat{U} \Psi_A(t) \quad (1.20)$$

The behavior of the system will be the following: the first term is diagonal, and as long as the second term doesn't become too "large", you will follow the eigenstates of your system. This evolution is called adiabatic. The adiabatic behavior correction, i.e., the last term in the expression (1.20), takes the following form:

$$\frac{\hbar}{2} \begin{pmatrix} 0 & \gamma(t) \\ \gamma^*(t) & 0 \end{pmatrix} \quad (1.21)$$

Where  $\gamma(t)$  denotes the deviation from adiabatic coupling between the  $\hat{A}$  eigenstates. Its expression is:

$$\gamma(t) = -i \frac{\dot{\delta}(t)\Omega_1(t) - \delta(t)\dot{\Omega}_1(t)}{\lambda(t)^2} \quad (1.22)$$

And for the non-adiabatic term to remain small, we have to ensure that it satisfies the adiabaticity condition given by:

$$|\gamma(t)| \ll \sqrt{\Omega_1^2(t) + \delta^2(t)} \quad (1.23)$$

Which, corresponds to the condition  $|\dot{\theta}| \ll \sqrt{\delta^2 + \Omega_1^2}$  or equivalently  $|\dot{\delta}\Omega_1 - \delta\dot{\Omega}_1| \ll (\delta^2 + \Omega_1^2)^{\frac{3}{2}}$  in the case of expression (1.14). There is a particular case close to point out where  $\Omega = 0$ . This means that the RF field isn't coupled to the Zeeman sublevel. In that case, there is necessarily a level crossing leading to spin-flip transitions that results in the loss of atoms in the trap.

### 1.1.2 The dressed quadrupole trap

The principle of trapping atoms with a dressed potential is well established. This is the time to expose the specificity of the trap used for the experimental work in this PhD: the magnetic field arises from two coils in an anti-Helmholtz configuration, generating a quadrupole magnetic field. This part closely follows the Ref. [63]. The specificity of such a setup is a magnetic field that vanishes at the center of the trap. This quadrupole field has the following expression near the trap center:

$$B_0(\mathbf{r}) = b'(x\mathbf{e}_x + y\mathbf{e}_y - 2z\mathbf{e}_z) \quad (1.24)$$

Where  $b'$  is the magnetic field gradient. Arising from the field expression, one can express the Larmor frequency felt by the atoms:

$$l_b(r, z) = \sqrt{x^2 + y^2 + 4z^2} = \sqrt{r^2 + 4z^2} \quad \omega_0(\mathbf{r}) = \alpha\sqrt{x^2 + y^2 + 4z^2} \quad \alpha = \frac{|g_F|\mu_B b'}{\hbar} \quad (1.25)$$

As described in Sec.1.1.1, the atoms are trapped along the isomagnetic surface defined by  $\omega_0 = \omega_{\text{rf}}$ . This condition describes an ellipsoidal surface with a horizontal radius twice as large as its vertical one. The expression on this surface is:

$$x^2 + y^2 + 4z^2 = r_b^2 \quad r_b = \frac{\omega_{\text{rf}}}{\alpha} \quad (1.26)$$

Furthermore, gravity pulls the atoms towards the bottom of the trap. This contribution always aligns with the  $z$ -axis. This results in having a compressed disc of atoms at the very bottom of our trap.

However, an important point has to be raised: the results derived do not take into account the relative orientation of the magnetic field and the polarization of the atoms. All the derivations of Sec.1.1.1 were performed with the magnetic field direction as the quantization axis  $z$ . It is thus necessary to give an expression of the unitary vector along the direction of the magnetic field that we now call  $\mathbf{u}$ :

$$\mathbf{u} = \frac{x\mathbf{e}_x + y\mathbf{e}_y - 2z\mathbf{e}_z}{\sqrt{x^2 + y^2 + 4z^2}} \quad (1.27)$$

#### Local coupling in the trap

As stated in the previous section, the expression of the dressed potential of atoms is:

$$V_{m_F}(\mathbf{r}) = m_F \hbar \sqrt{\delta^2(\mathbf{r}) + \Omega_1^2(\mathbf{r})} \quad (1.28)$$

The difference between the previous expression and this one is the space dependence of the coupling amplitude. The two contributions have significantly different behaviors:

- The detuning's spatial dependence ( $\delta(\mathbf{r})$ ): this term is responsible for locating the minimum of potential on an isomagnetic surface. The expression of the detuning is:

$$\delta(\mathbf{r}) = \omega_{\text{rf}} - \frac{|g_F|\mu_B B_0(\mathbf{r})}{\hbar} \quad (1.29)$$

- The coupling amplitude's spatial dependence ( $\Omega_1(\mathbf{r})$ ): the local coupling amplitude had been computed in the rotating wave approximation, as stated in Sec.1.1.1. To understand this term's dependence, consider the magnetic field's orientation (noted as

$\mathbf{u}$ ) and the RF field polarization (noted  $\boldsymbol{\epsilon}$ ). By taking these parameters into account, the expression is [33] :

$$\Omega_1(\mathbf{r}) = -\sqrt{2}\frac{g_F\mu_B}{\hbar}\mathcal{B}_1\mathbf{e}_s^*(\mathbf{r}) \cdot \boldsymbol{\epsilon}(\mathbf{r}) = -\Omega_{\text{RF}}\mathbf{e}_s^*(\mathbf{r}) \cdot \boldsymbol{\epsilon}(\mathbf{r}) \quad (1.30)$$

$$\Omega_{\text{RF}} = \sqrt{2}\frac{g_F\mu_B}{\hbar}\mathcal{B}_1 \quad (1.31)$$

Because the coupling is affected by the relative orientation of the field and polarization, there may be some points where the coupling vanishes. These points will be referred to as "holes" and they have an important role in the experimental studies conducted in chapter 3. It is important to know where they are because they could act as an atom sink inside our trap, and we would lose atoms if they came too close to them. This section will continue with the calculations done in specific polarization cases.

Also, the polarization is always considered on the x-y plane. The coils that generate the RF field were carefully aligned perpendicular to the  $x$  and  $y$  axes. However, if some small misalignments are observed, they will effectively weaken the Landé factor instead of having a direct effect on the polarization.

### Circularly polarized radiofrequency

At first, the atoms stay at the bottom of the bubble ( $\mathbf{u} = \mathbf{e}_z$ ) and the RF field is polarized circularly along the  $z$ -axis in a  $\sigma^s$  state:

$$\boldsymbol{\epsilon} = -\frac{1}{\sqrt{2}}(s\mathbf{e}_x + i\mathbf{e}_y) \quad (1.32)$$

In such a case, the resonant coupling amplitude is given by:

$$|\Omega_1(\mathbf{r})| = \frac{\Omega_0}{2}\left(1 + s\frac{2z}{l_b(r, z)}\right) \quad (1.33)$$

Where  $\Omega_0$  is the maximum of coupling on the resonant surface and  $l_b(r, z)$  is defined in (1.25). One can see that there are two contributions:

- The minimum of potential is at the very bottom of the bubble. This determines the position where the atom is trapped. When the polarization is  $\sigma^s$  the maximum of coupling is at the bottom of the bubble, whereas when the rf is  $\sigma^{-s}$  polarized, the maximum of coupling is at the top. As we are interested in having the maximum number of atoms at the bottom of the bubble, we set  $s = -1$ .
- On the resonant surface, where the potential is equal to the coupling amplitude, it becomes weaker and weaker as the atom gets closer to the hole. This acts as an attraction felt by the atoms toward the hole.

On top of these contributions, one should add the gravity that pushes the atom at the bottom of the bubble. To stay at the very bottom of the trap, the gravity had to be larger than the variation of the coupling:

$$F\hbar\Omega_0 < Mgr_b \quad (1.34)$$

Where  $r_b$  is defined in (1.29). An alternative formulation of this condition can be set. Let us first define the magnetic gradient to gravity ratio:  $\beta = F\frac{\hbar\alpha}{Mg}$ . The condition can now be reframed as:

$$\frac{\Omega_0}{\omega_{\text{rf}}} < \frac{1}{\beta} \quad (1.35)$$

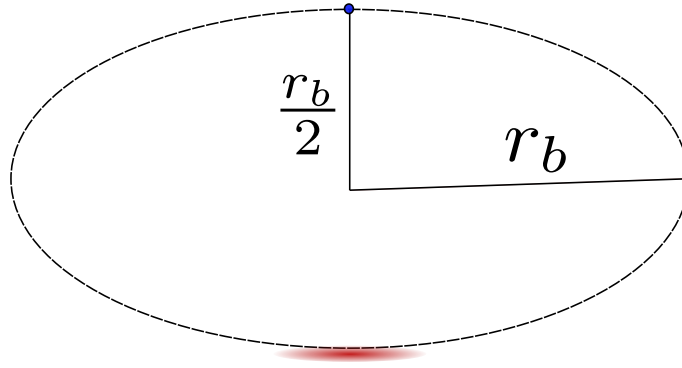


**Figure 1.2** — Transverse view of the bubble trap for circular polarization along  $z$ . The red shade indicates the position of the cloud. The blue dot at the top shows where the hole position is.

Interestingly enough, this condition has to be true for another reason: to stay within the boundary of the rotating wave approximation. Therefore, one has to ensure the gradient of Rabi coupling is strictly inferior to gravity for our atom trap to be well described by the model we have developed so far.

As gravity plays a pivotal role, one has to take it into account to determine the position at which the atoms are at rest in the trap. The gravity will shift downward from the position where the atoms lie in the trap. This position will be given by  $z = -R$  [32] with:

$$R = \frac{r_b}{2} \left( 1 + \frac{1}{\sqrt{4\beta^2 - 1}} \frac{\Omega_0}{\omega_{\text{rf}}} \right) \quad (1.36)$$

Around the minimum of potential, one can consider the trap harmonic and isotropic. The atoms are squeezed at the surface of the bubble along the  $z$ -axis, and the coupling in the  $x$ - $y$  plane is looser. By doing a second order development of the full potential around  $R$ , one can find the oscillation frequencies:

$$\omega_{\perp} = \frac{g}{4R} \left( 1 - \frac{F\hbar\Omega_0}{2MgR} \sqrt{1 - \frac{1}{4\beta^2}} \right)^{\frac{1}{2}} \quad (1.37)$$

$$\omega_z = 2\alpha \sqrt{\frac{F\hbar}{M\Omega_0}} \left( 1 - \frac{1}{4\beta^2} \right)^{\frac{3}{4}} \quad (1.38)$$

Following [64] and for clarity's sake, we introduce  $\gamma$  which describes the coupling gradient to gravity ratio:

$$\gamma = \frac{F\hbar\Omega_0}{MgR} \sqrt{1 - \frac{1}{4\beta^2}} \quad (1.39)$$

This simplifies the expression of  $\omega_{\perp}$ , which now becomes:

$$\omega_{\perp} = \frac{g}{4R} \left( 1 - \frac{\gamma}{2} \right)^{\frac{1}{2}} \quad (1.40)$$

The case where the radiofrequency field is circularly polarized is the one used on the experimental setup. In a normal configuration, the RF frequency is  $\omega_{\text{RF}} = 300$  kHz, the magnetic



field gradient is  $25.3 \text{ kHz} \cdot \mu\text{m}^{-1}$  and a maximum Rabi coupling of  $\Omega_0 = 50 \text{ kHz}$ . This corresponds to  $\omega_{\perp} = 33.6 \text{ Hz}$  and  $\omega_z = 368.35 \text{ Hz}$ . As one can see, there is an important difference between the two oscillation frequencies, which means the trap is highly anisotropic at the bottom of the bubble. This property will be important later on.

### Linearly polarized radio-frequency

As in the previous situation, the atoms stay at the bottom of the bubble ( $\mathbf{u} = \mathbf{e}_z$ ), and the RF field is polarized linearly along the  $x$ -axis ( $\boldsymbol{\epsilon} = \mathbf{e}_x$ ):

$$|\Omega_1(\mathbf{r})| = \frac{\Omega_0}{2} \sqrt{1 - \frac{x^2}{l_b^2(r, z)}} \quad (1.41)$$

There must be  $|x| = r_b$  for the coupling to vanish. Only two points in the system satisfy this condition: the two points on the equatorial plane of the bubble at  $x = r_b$  and  $x = -r_b$ . Furthermore, the minimum of potential, taking gravity into account, is the same as in the circularly polarized case stated in (1.36).

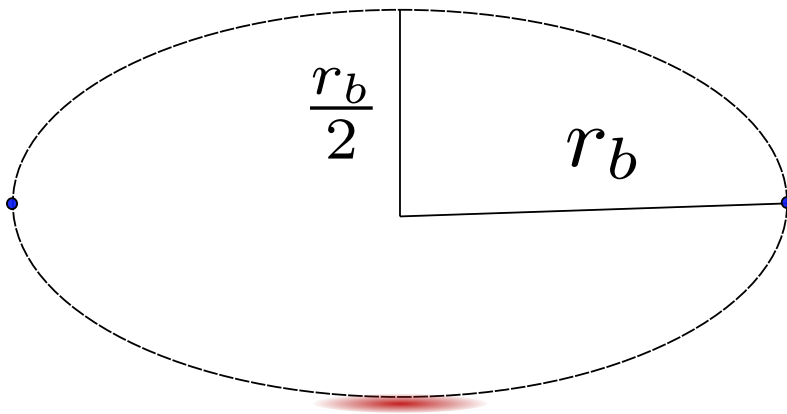


**Figure 1.3** – Transverse view of the bubble trap for linear polarization along  $x$ . The red shade indicates the position of the cloud. The blue dots at the edges show the two hole positions.

However, the oscillation frequencies change. There is no longer an orthogonal plane perpendicular to the  $z$ -axis where the coupling is always the same. The trap frequencies become:

$$\omega_x = \sqrt{\frac{g}{4R}} \left[ 1 - \frac{F\hbar\Omega_0}{mgR} \sqrt{1 - \frac{1}{4\beta^2}} \right]^{\frac{1}{2}} = \sqrt{\frac{g}{4R}} [1 - \gamma]^{\frac{1}{2}} \quad (1.42)$$

$$\omega_y = \sqrt{\frac{g}{4R}} \quad (1.43)$$

$$\omega_z = 2\alpha \sqrt{\frac{F\hbar}{m\Omega_0}} \left( 1 - \frac{1}{4\beta^2} \right)^{\frac{3}{4}} \quad (1.44)$$

### General results for elliptical polarization of the radio-frequency field

Here I will present the derivation of the position of the holes for an arbitrary polarization in the horizontal plane, which can also be found in Ref. [64]. As the elliptical polarization is a

general case, a few qualitative behaviors can be described before giving the formulae. Before going any further, some reflections can be drawn from the linearly and circularly polarized RF field. On the one hand, there is only one hole when the field is circularly polarized along the  $z$ -axis, either at the top for  $\sigma^-$  or at the bottom for  $\sigma^+$ . On the other hand, when the field is linearly polarized, there are two holes on the equatorial plane of the bubble positioned along an axis at the polar opposite position. Furthermore, for the linear polarization case, there is a coupling anisotropy along the polarization axis, and this is something we expect to observe for elliptical polarization. The general expression of the dot product with the orientation and the polarization is given by [33]:

$$\begin{aligned} \mathbf{e}_s^*(\mathbf{r}) \cdot \boldsymbol{\epsilon}(\mathbf{r}) &= |\boldsymbol{\epsilon} \times \mathbf{u} + i s \mathbf{u} \times (\boldsymbol{\epsilon} \times \mathbf{u})| \\ &= \frac{1}{2} \sqrt{1 - |\boldsymbol{\epsilon} \cdot \mathbf{u}|^2 + |\boldsymbol{\epsilon} \times \mathbf{u}|^2 + 2 i s \mathbf{u} \cdot (\boldsymbol{\epsilon} \times \boldsymbol{\epsilon}^*)} \end{aligned} \quad (1.45)$$

Now the elliptical polarization in the plane orthogonal to the  $z$ -axis is given by:

$$\boldsymbol{\epsilon} = \cos \Theta \mathbf{e}_x + e^{i\Phi} \sin \Theta \mathbf{e}_y \quad (1.46)$$

Where  $\Theta$  quantifies the amplitude ratio between the two antennas and  $\Phi$  is the phase difference between these same antennas. As detailed in this section, the trap has a shell-shaped geometry with the atoms confined on the surface. Here is an introduction to new angular coordinates that make the analytical expression simpler. The coordinates of the holes are determined when  $|\Omega_1|^2$  vanishes, and their position is given by:

$$\begin{cases} x = r_b \sin(t) \cos(\phi) \\ y = r_b \sin(t) \sin(\phi) \\ z = \frac{r_b}{2} \cos(t) \end{cases} \quad (1.47)$$

The cartesian coordinates account for the bubble compression along the  $z$ -axis, and the angles  $t$  and  $\phi$  report the position of the holes on a sphere. Also, the parameters that are tuned in the experiment are those related to the RF field; it is therefore important to know how a change in the RF field affects the coordinates of these holes. The relation between the two sets of parameters is given by [64]:

$$\begin{cases} \tan(2\phi) = \tan(2\Theta) \cos(\Phi) \\ \cos(t) = \frac{\sin(2\Theta) \sin(\Phi)}{1 + \sqrt{1 - \sin^2(2\Theta) \sin^2(\Phi)}} \end{cases} \quad (1.48)$$

There are always two solutions for  $\tan(2\phi)$  that are aligned along an axis crossing the  $z$ -axis, and these solutions are  $\phi$  and  $\phi + \pi$ . The  $\phi$  angle represents the angle between the polarization axes and the lab axes. The  $\cos(t)$  expression determines the vertical position of the holes on the bubble, and the results for circularly and linearly polarized RF fields are found. A representation of these two parameters is shown in Fig.1.4.

Now that the hole positions on the ellipsoid are known, having a general formula to estimate the coupling is necessary. By taking into account the expression (1.45), the coupling becomes:

$$\Omega^2 = \frac{\Omega_{\text{RF}}^2}{2} \left( 1 - \frac{r^2 + (x^2 - y^2) \cos(2\Theta) - 2xy \sin(2\Theta) \cos(\Phi)}{2l_b^2} - \frac{2z}{l_b} \sin(2\Theta) \sin(\Phi) \right) \quad (1.49)$$

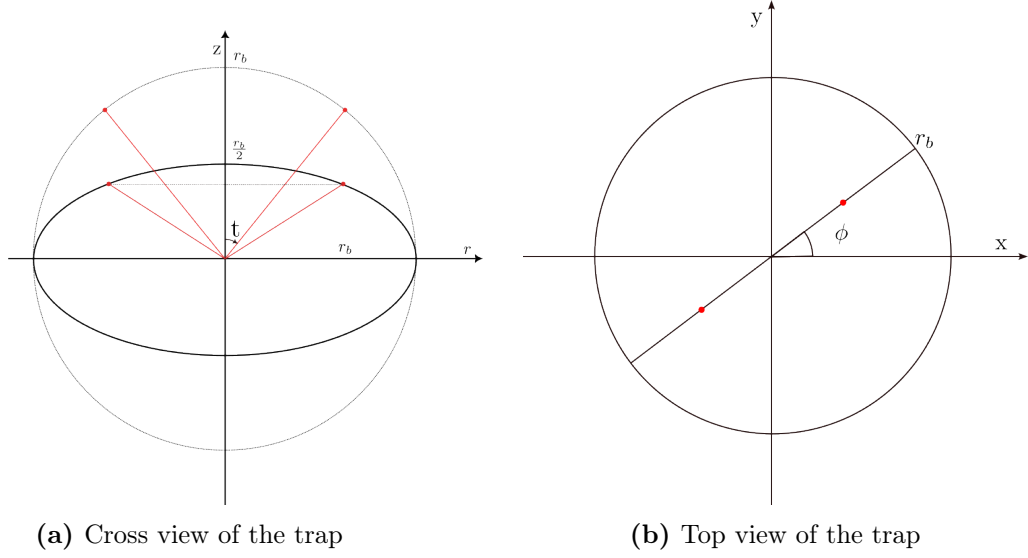


**Figure 1.4** – Schematic representation of the ellipsoid with the holes. The red dots represent the hole. The black solid line represents the ellipsoid trap. The black dashed line on 1.4a represents the associated sphere of radius  $r_b$ .

In order to have a clearer understanding of this expression, one must simplify it:

- Instead of using the  $x$ - $y$  axis, it seems more natural to use a frame oriented along the polarization axes:

$$\begin{cases} x' = \cos(\phi)x + \sin(\phi)y \\ y' = \sin(\phi)x - \cos(\phi)y \end{cases} \quad (1.50)$$

- Let us introduce the coupling anisotropy factor in the  $x$ - $y$  plane:

$$\eta = \frac{1 + \sin(2\Theta) \sin(\Phi)}{2} \quad (1.51)$$

The values taken are between 0 and 1. When the polarization is circular, the values are 0 and 1, whereas  $\eta = \frac{1}{2}$  when the polarization is linear. This anisotropy factor has an effect on the coupling at the bottom of the bubble, which becomes:

$$\Omega_0 = \sqrt{\eta} \Omega_{\text{RF}} \quad (1.52)$$

The coupling expression becomes:

$$\Omega^2 = \frac{\Omega_{\text{RF}}^2}{2} \left( 1 - \frac{r^2 - 2\sqrt{\eta(1-\eta)}(x'^2 - y'^2)}{2l_b^2} - \frac{2z}{l_b}(2\eta - 1) \right) \quad (1.53)$$

The trap frequencies at the bottom of the trap become [64]:

$$\omega_x = \sqrt{\frac{g}{4R}} \left[ 1 - \frac{\gamma}{2} \left( 1 - \sqrt{\frac{1}{\eta} - 1} \right) \right]^{\frac{1}{2}} \quad (1.54)$$

$$\omega_y = \sqrt{\frac{g}{4R}} \left[ 1 - \frac{\gamma}{2} \left( 1 + \sqrt{\frac{1}{\eta} - 1} \right) \right]^{\frac{1}{2}} \quad (1.55)$$

$$\omega_z = 2\alpha \sqrt{\frac{F\hbar}{M\Omega_0}} \left( 1 - \frac{1}{4\beta^2} \right)^{\frac{3}{4}} \quad (1.56)$$

To conclude this part, one last parameter should be mentioned. Even if the coupling anisotropy is a convenient parameter to describe our system, let us not forget that it has a geometrical effect on the atom in the trap. This results in a squeeze in the direction where the coupling is strongest and a looser confinement in the opposite direction. A parameter that describes this fact is the geometrical anisotropy factor:

$$\varepsilon = \frac{|\omega_{x'}^2 - \omega_{y'}^2|}{\omega_{x'}^2 + \omega_{y'}^2} = \frac{\gamma\sqrt{1-\eta}}{2-\gamma} \quad (1.57)$$

## 1.2 Elements of a Bose-Einstein condensate in an oblate trap

Now that the trapping mechanism has been explained for an atom, there are multiple atoms trapped inside. The gas formed by these atoms forms a cloud of  $^{87}\text{Rb}$ , and when this cloud is cold enough, a Bose-Einstein condensate forms. That is why a description of such a phenomenon is needed. The study of Bose-Einstein condensation is closely linked to the study of superfluidity and its dynamical properties, such as the presence of vortices [14].

### 1.2.1 Bose-Einstein condensation

#### The Bose-Einstein condensation - excited states saturation

This starts with the description of  $N$  bosons with no interaction. Because the ensemble is at thermal equilibrium and is best described by the grand-canonical ensemble, the chemical potential  $\mu$  should be introduced. We consider a quantum description of our system with discrete levels, and using the Bose-Einstein statistics, the average number of particles in a given state  $j$  is given by:

$$N_j = \frac{1}{e^{\frac{E_j - \mu}{k_B T}} - 1} \quad (1.58)$$

This number of atoms is positive, and it limits  $\mu$  to  $\mu < \min(E_j)$ . By setting the ground state energy  $E_0$  to 0 and supposing this state is non-degenerate, with  $N_0$  particle in it, the chemical potential must be:

$$\mu < 0 \quad (1.59)$$

In general, the number of particles populating the excited states can be defined by:

$$N_{exc} = N - N_0 = \sum_{j>0} \frac{Z}{e^{\frac{E_j}{k_B T}} - Z} \quad (1.60)$$

Where  $Z = e^{\frac{\mu}{k_B T}}$  is the fugacity, and by definition of the fugacity,  $Z < 1$ . It implies the existence of an upper bound for the excited state:

$$N_{exc} < N_{exc}^{(max)}(T) = \sum_{j>0} \frac{1}{e^{\frac{E_j}{k_B T}} - 1} \quad (1.61)$$

The only tunable parameter by the experimentalist is  $T$ . If there is  $N > N_{exc}^{(max)}(T)$ , all the atoms above  $N_{exc}^{(max)}(T)$  must be in the ground state, resulting in a large population in the ground state of the trap. Because  $N_{exc}^{(max)}(T)$  is dependent on the dimension and the geometry

of our system, it is possible that  $N_{exc}^{(max)}(T)$  will not converge. In such a case, this prevents the condensation from happening in the system.

As the maximum number of atoms in the excited states only depends on the temperature, there exists a certain value of T below which a BEC forms when condensation is possible. This value is referred to as the critical temperature and is noted  $T_c$ .

### Bose-Einstein condensate with interactions

To describe the collection of atoms, the field operator noted  $\hat{\Psi}(\mathbf{r})$  must be introduced. This operator creates a particle in the system at position  $\mathbf{r}$ . To give an expression of such an operator, the single particle states  $\psi_i(\mathbf{r})$  are used alongside the creations operator  $\hat{a}_i$ :

$$\hat{\Psi}(\mathbf{r}) = \sum_i \varphi_i(\mathbf{r}) \hat{a}_i \quad (1.62)$$

A significant portion of the atoms in the "cold" system, that is, below the critical temperature, are in the ground state:  $N_0 \gg 1$ . The previous field operator can be rewritten as:

$$\hat{\Psi}(\mathbf{r}) = \sqrt{N_0} \varphi_0(\mathbf{r}) + \sum_{i>0} \varphi_i(\mathbf{r}) \hat{a}_i \quad (1.63)$$

In the model, the wavefunction associated with the condensate will be defined by the wavefunction of the ground state. In the case of a harmonic trap, this would lead to a gaussian profile of atom density in the trap. But this is not what has been observed experimentally. The reason is that we neglected all atom-atom interaction inside the trap. There is a need to describe the interaction of the Rubidium quantum gas.

Qualitatively, the interactions inside the quantum gas will change the wavefunction's shape. A few more details about the system must be given to describe these interactions:

- The population inside the ground state is large:

$$\int |\varphi_0|^2 d\mathbf{r} = N_0 \gg 1 \quad (1.64)$$

The consequence of this statement is that the non-commutativity of  $\hat{a}_i$  and  $\hat{a}_i^\dagger$  is negligible and therefore ignored. Also, it implies that  $N \approx N - 1$ .

- The interaction inside the BEC is described by "s-wave" collisions. The collision can be modeled by a contact potential that depends only on one parameter, the scattering length [2, 65] noted  $a$ :

$$V_{int}(\mathbf{r}', \mathbf{r}) = g_{int} \delta(\mathbf{r}' - \mathbf{r}) \quad g_{int} = \frac{4\pi \hbar^2 a}{M} \quad (1.65)$$

These interactions can either be attractive or repulsive. This behavior depends on the sign of  $a$ .

By giving the Heisenberg equation to the field operator and replacing it with the ground state wavefunction, a new equation is formulated [2]:

$$i\hbar \frac{\partial \psi(\mathbf{r}, t)}{\partial t} = \left( -\frac{\hbar^2}{2M} \nabla^2 + V_{ext}(\mathbf{r}) + g_{int} |\psi(\mathbf{r}, t)|^2 \right) \psi(\mathbf{r}, t) \quad (1.66)$$

This is the Gross-Pitaevskii equation, a non-linear Schrödinger equation describing accurately an interacting Bose-Einstein condensate in a trap. There are three different terms in this equation: the first term, depending on  $\nabla^2$ , is the kinetic energy; the second term describes the trapping potential; and ultimately, the last term describes the interaction energy. This is a mean-field description of one particle evolving in a field created by  $N-1$  particles. To investigate the time-independent case, we divide the time and spatial dependencies with  $\psi(\mathbf{r}, t) = \phi(\mathbf{r})e^{-i\frac{\mu}{\hbar}t}$  and by plugging this expression into Eq.(1.66), we get:

$$\left(-\frac{\hbar^2}{2M}\nabla^2 + V_{ext}(\mathbf{r}) + g_{int}|\phi(\mathbf{r})|^2\right)\phi(\mathbf{r}) = \mu\phi(\mathbf{r}) \quad (1.67)$$

Solving this equation will give the wavefunction of a condensate at rest.

When dealing with repulsive interactions and a large number of particles in the trap, the kinetic energy becomes negligible. This is called the Thomas-Fermi approximation. In that case, we will compare the kinetic term with the typical extension of the cloud of atoms, which is related to the length scale of the trap:  $d_{trap} = \sqrt{\hbar/M\omega_{trap}^2}$ . As long as  $Na \gg d_{trap}$ , the approximation holds. Rewriting Eq.(1.67) in the Thomas-Fermi regime leads to the following expression of the density profile:

$$n(\mathbf{r}) = |\psi(\mathbf{r})|^2 = \frac{\mu - V_{ext}(\mathbf{r})}{g_{int}} \quad (1.68)$$

More specifically, in a 3D harmonic trap, it leads to a density:

$$n(\mathbf{r}) = n(0)\left(1 - \frac{x^2}{R_x^2} - \frac{y^2}{R_y^2} - \frac{z^2}{R_z^2}\right) \quad (1.69)$$

Where  $n(\mathbf{r})$  is positive, and 0 in all the other positions. The parameters noted  $R_{x,y,z}^2 = 2\mu/M\omega_{x,y,z}^2$  are the Thomas-Fermi profile; they give the full extension of the cloud along each direction. As seen in the description of the quadrupole RF dressed trap, the oscillation frequencies of the trap are vastly different. This leads to an anisotropic trap with strong confinement along the  $z$ -axis.

However, the expression obtained with the Thomas-Fermi approximation has one strong limitation. It implies a discontinuity in the spatial derivative at the very edge of the cloud, and this leads to a divergence of the kinetic energy term. When the density of atom  $n(\mathbf{r})$  is low, this approximation does not describe the system well. An estimation of the size over which the kinetic term becomes non-negligible is:

$$\frac{\hbar^2}{2M\xi^2} = \mu \longrightarrow \xi = \sqrt{\frac{\hbar^2}{2M\mu}} = \frac{1}{\sqrt{8\pi a n}} \quad (1.70)$$

$\xi$  is the healing length, it is the shortest distance over which the wavefunction can change, and it represents the minimal size over which the wavefunction passes from 0 to  $n$ .

### Hydrodynamic formulation

The time-dependent Gross-Pitaevskii equation(1.66) can be reformulated to look a lot closer to a description of a flowing fluid. This is accomplished by multiplying (1.66) by  $\psi^*$  and subtracting its complex conjugate:

$$i\hbar\left(\psi^*\frac{\partial\psi}{\partial t} + \psi\frac{\partial\psi^*}{\partial t}\right) = \frac{\hbar^2}{2M}\left(\psi^*\nabla^2\psi - \psi\nabla^2\psi^*\right) \quad (1.71)$$

By introducing the velocity  $\mathbf{v}$  and the local density  $n$ :

$$\begin{aligned} n(\mathbf{r}, t) &= |\psi(\mathbf{r}, t)|^2 \\ \mathbf{v}(\mathbf{r}, t) &= \frac{\hbar}{2Mi|\psi|^2} \left( \psi^* \nabla(\psi) - \psi \nabla(\psi^*) \right) \end{aligned} \quad (1.72)$$

That are injected in Eq.(1.71), and we obtain the continuity equation:

$$\frac{\partial n}{\partial t} + \nabla \cdot (n\mathbf{v}) = 0 \quad (1.73)$$

Another way to write the wavefunction is to use the amplitude-phase representation:

$$\begin{aligned} \psi(\mathbf{r}, t) &= \sqrt{n(\mathbf{r}, t)} e^{iS(\mathbf{r}, t)} \\ \mathbf{v}(\mathbf{r}, t) &= \frac{\hbar}{M} \nabla(S(\mathbf{r}, t)) \end{aligned} \quad (1.74)$$

Using this formulation in the equation (1.66), multiplying by  $\psi^*$ , and taking the real part of the formula, we get the new equation, which is written:

$$\frac{1}{2} M \mathbf{v}^2 + \frac{\hbar^2}{2M\sqrt{n}} \nabla^2(\sqrt{n}) + g_{int} n + V_{ext} + M \frac{\partial}{\partial t} \left( \frac{\hbar S}{M} \right) = 0 \quad (1.75)$$

This equation describes the dynamics of a quantum fluid. It is very close to the description of a classical fluid, with the addition of a specific term called the quantum pressure term,  $\frac{\hbar^2}{2M\sqrt{n}} \nabla^2(\sqrt{n})$ . It should be stressed out that equations (1.75) and (1.73) are equivalent to equation (1.66).

### Excitation of a Bose-Einstein condensate

So far, we have described a BEC at rest. That is to say, we said nothing about the excitation of a condensate. In an attempt to describe a small variation of the BEC, let's first define what a small perturbation of the wavefunction is:

$$\psi(\mathbf{r}, t) = [\psi_0(\mathbf{r}) + \delta\psi(\mathbf{r}, t)] e^{-i\frac{\mu t}{\hbar}} \quad \delta\psi(\mathbf{r}, t) = A e^{i(\mathbf{k}\cdot\mathbf{r} - \omega t)} \quad (1.76)$$

In this expression,  $\psi_0(\mathbf{r}, t)$  represents a solution of the Gross-Pitaevskii equation at rest, and the perturbation is small. This means  $|\delta\psi| \ll |\psi|$  and the perturbation is regarded as a plane-wave. By linearising equation (1.67) and removing the higher order term in  $\delta\psi$ , we get:

$$i\hbar \frac{\partial}{\partial t} (\delta\psi(\mathbf{r}, t)) = -\frac{\hbar^2}{2M} \nabla^2 \delta\psi + g_{int} n(\mathbf{r}) [\delta\psi^* + 2\delta\psi] - \mu \delta\psi \quad (1.77)$$

This is valid when dealing with a uniform system, so when  $V_{ext} = 0$ . In that case, for a density  $n$ , the excitation spectrum, called the "Bogolyubov spectrum", is given by:

$$E_k = \sqrt{\frac{\hbar^2 k^2}{2M} \left( \frac{\hbar^2 k^2}{2M} + 2g_{int} n \right)} = \frac{\hbar^2 k^2}{2M} \sqrt{1 + \frac{2}{(k\xi)^2}} \quad (1.78)$$

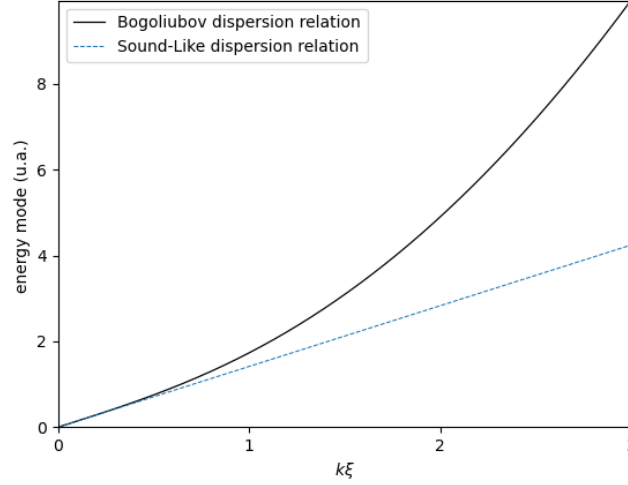


**Figure 1.5** — Graph displaying the Bogolyubov dispersion relation in black solid line and the plane wave dispersion relation in dashed light blue line.

At small energy, one can see that  $E = \hbar ck$  with  $c = \sqrt{\frac{g_{int}n}{M}}$ . This corresponds to the phononic branch of the spectrum: the elementary excitations for low  $k$  behave as soundwaves, and  $c$  is the speed of sound in the condensate. This is depicted in Fig.1.5. When dealing with a non-uniform gas, the situation describing trapped gases, the calculation is modified because of the potential. The low-energy excitations become collective modes with their own dispersion relation [66].

### Critical velocity and superfluidity

Having determined the dispersion relation of the excitation, the question of how to produce it is still open. Let us first describe an impurity flowing inside a Bose-Einstein condensate. The system composed of the BEC and the impurity has a constant energy. The impurity will transfer energy to the fluid by creating elementary excitation as long as it is energetically favorable, so:

$$E_k - \hbar \mathbf{k} \cdot \mathbf{v} < 0 \quad (1.79)$$

According to Eq.(1.79), there is a minimum velocity below which no elementary excitations are allowed to form [2]. This critical velocity is given by:

$$v > v_c = \min_k \left( \frac{E_k}{\hbar k} \right) \quad (1.80)$$

For a uniform gas, the critical velocity is deduced from Eq.(1.78) and corresponds to the speed of sound in the condensate:

$$v_c = \sqrt{g_{int} \frac{n}{M}} \quad (1.81)$$

Another formulation of this problem is that a defect won't interact with the BEC below a certain velocity. This is the definition of superfluidity originally given by Landau [67].



### Rotation of a superfluid - presence of vortex

The BEC can be set to rotate. However, the BEC is a superfluid, and this implies that the expression of the velocity field in Eq.(1.74) directly links the velocity to the phase of the wavefunction. This expression shows the superfluid velocity is irrotational, so:

$$\nabla \times \mathbf{v} = 0 \quad (1.82)$$

A quantity that gives information about how the velocity behaves is the circulation of the velocity over a closed loop:

$$\oint_C \mathbf{v} \cdot d\mathbf{l} = \frac{\hbar}{M} \Delta_C(S) = \frac{\hbar}{M} 2\pi l \quad l \in \mathbb{Z} \quad (1.83)$$

So the velocity circulation is quantized, and if this circulation is not equal to 0, it implies a phase singularity exists at a specific point. In order not to have divergence, the local density of atoms vanishes at this particular point. This is a vortex, an excitation of the system carrying angular momentum to a point where the local density vanishes. Such an excitation cannot be described by the previous excitation description leading to the dispersion relation because a vanishing density cannot be considered a small density variation. It is these vortices that contain the rotation of the superfluid.

### 1.2.2 Quasi-2D regime

The anisotropy of the trap described in Sec.1.1 is large and implies that a change in geometry has to be taken into account when describing the system. First, the criteria for having a two-dimensional gas will be detailed. Then collective modes in this regime will be presented. Ultimately, a brief description of a rotating BEC will be given, and a specific excitation will be presented: the vortex.

#### Criteria for the 2 dimensional regime

When passing from a three-dimensional to a two-dimensional system, this system must be compressed along one direction. This has the effect of freezing the move along the transverse dimension, and the atoms will be assumed to be trapped inside an anisotropic harmonic trap in this section. It implies two different sets of conditions:

- The temperature and the chemical potential have to be too low for any excited state to be populated:

$$k_B T < \hbar\omega_{\perp} \quad \mu < \hbar\omega_{\perp} \quad (1.84)$$

- The interaction in the gas must occur in the plane. As the rubidium BEC has collisions described by s-wave scattering, which is fully described by the scattering length, the ground state spatial extension  $d_z = \sqrt{\hbar/M\omega_z^2}$  has to be smaller than the scattering length:

$$d_z < a \quad (1.85)$$

The second condition is not met with the experimental setup described in this thesis. So the BEC is not strictly 2D. But we did meet the first requirement, meaning that the system is

described by the quasi-2D regime: the system's dynamic is frozen along one dimension but the collisions are still modeled as happening in three dimensions with a modified coupling:

$$g_{2D} = \frac{g_{int}}{\sqrt{2\pi}d_z} = \frac{\hbar^2}{M}\tilde{g} \quad \tilde{g} = \sqrt{8\pi}\frac{a}{d_z} \quad (1.86)$$

The parameter  $\tilde{g}$  is a dimensionless coupling constant. In this regime, the equation (1.66) stays valid as long as we integrate the wavefunction along the perpendicular direction of the plane.

In the quasi-2D regime,  $N_{exc}^{max}$  in Eq.(1.61) does not converge. This condition prevents the Bose-Einstein condensation from happening in the general case for 2D system. However, a phase transition formalized by Berezinskii [68], Kosterlitz and Thouless [18] (BKT transition) describes the appearance of a critical phase-space transition above which a superfluid state appears in the system [69]:

$$\rho\lambda_{dB}^2 = \mathcal{D}_c = \ln\left(\frac{380}{\tilde{g}}\right) \quad (1.87)$$

Where  $\lambda_{dB} = \sqrt{2\pi\hbar^2/Mk_bT}$  is the de Broglie wavelength and T is the temperature. At this point, the superfluid density of the system jumps from 0 to 4, which is called the BKT "universal jump". The appearance of a superfluid density is related to a quantity called the long-range order, which is defined by the first order correlation function of  $\hat{\Psi}$ :

$$g_1(\mathbf{r}, \mathbf{r}') = \langle \hat{\Psi}^\dagger(\mathbf{r})\hat{\Psi}(\mathbf{r}') \rangle \quad (1.88)$$

If a limit exists for  $|\mathbf{r} - \mathbf{r}'| \rightarrow \infty$  and is greater than 0, the condensation can happen. In the case of a 2D system below the critical temperature, the long-range order goes to zero "slowly": the decreasing behavior is algebraic. Therefore, for a system small enough, there is coherence in phase, leading to a superfluid state. This new object is called a quasi-condensate and has phase fluctuations [70].

More specifically, in a 2D harmonic trap, true condensation for non-interacting particles can occur [71]. But the repulsive interactions of rubidium prevent this phenomenon from happening. However, a BKT transition occurs in the following conditions [72]:

$$\frac{N_{c,real}}{N_{0,c}} = 1 + \frac{3\tilde{g}}{\pi^3} \ln^2\left(\frac{\tilde{g}}{16}\right) + \frac{3\tilde{g}}{8\pi^2} \left[15 + \ln\left(\frac{\tilde{g}}{16}\right)\right] \quad (1.89)$$

The quasi-2D regime is of special interest for studying vortices. This is for topological reasons: when the condensate is in two dimensions, the vortex is point-like, whereas with a three-dimensional BEC, the vortex is a line. This leads to complex behaviors related to turbulent flows in the condensate.



# Chapter 2

## Experimental setup: the $^{87}\text{Rb}$ BEC machine

Preparing a Bose-Einstein condensate requires a sequence lasting from 20 s up to a few minutes and the coordination of multiple devices. This chapter intends to present the sequence needed to produce a BEC with the setup at the LPL. First, a presentation of the atomic properties of rubidium will be given. Then the means to cool rubidium with lasers will be presented. After that, the need to transport the cloud of atoms is explained, and the means by which we transport the cloud are detailed. In addition to this, the evaporative cooling processes and their challenges in a magnetic quadrupole trap are presented. This is done to explain how to obtain a BEC and how to load it in the dressed quadrupole trap. Ultimately, the imaging system is described.

A notable exclusion has been made in this chapter: the control system. This is because we changed it during my PhD, and as such, it is the subject of Chap.4.

As the experimental setup started a decade ago, a few PhD theses had already been written [64, 73–76] and defended. A more detailed presentation of the setup is available in these PhDs.

### 2.1 The laser cooling system

#### 2.1.1 The Rubidium and its magnetic sub-level

Rubidium is an alkali metal, that has two isotopes available:  $^{85}\text{Rb}$  and  $^{87}\text{Rb}$ . As presented in Chap.1, the scattering length of an element is the key property to look at for Bose-Einstein condensation. As such, only the isotope 87 can be used to obtain a BEC; the isotope 85 has a negative scattering length, which leads to collapsing Bose-Einstein condensate [77]. The  $^{87}\text{Rb}$  simple electronic structures, combined with its favorable collisional properties, make it a suitable atom for reaching Bose-Einstein condensation. From a historical perspective, it has been one of the first atoms with which physicists observed Bose-Einstein condensation [78].

By taking into account the total angular momentum given in Sec.1.1.1, the ground state is 2-fold degenerate with  $F \in \{0, 1\}$ , and the  $5P_{3/2}$  excited state is 4-fold degenerate with  $F \in \{0, 1, 2, 3\}$ . This transition is particularly interesting because the transition  $|5S_{1/2}, F = 2\rangle \rightarrow |5P_{3/2}, F' = 3\rangle$  is closed with a linewidth of  $\Gamma = 2\pi \times 5.89\text{ MHz}$ . The closed transition is

needed to have a magneto-optical trap (MOT), and the details of such a trapping mechanism will be addressed in Sec.2.1.3. The only details provided here are about the lasers: to trap atoms in MOT, one needs a closed transition and a laser that is red-detuned from the cycling transition. In the case of rubidium, this brings a problem because the laser comes closer to the  $|5S_{1/2}, F = 2\rangle \rightarrow |5P_{3/2}, F' = 2\rangle$ . When an atom is excited in the  $|5P_{3/2}, F' = 2\rangle$  state, it can decay into the  $|5S_{1/2}, F' = 1\rangle$  and is therefore no longer trapped because out of the cycling transition. To prevent this situation from happening, a laser is used to bring back the atoms in the cycling transition, and is referred to as the repumping beam. It is resonant with the  $|5S_{1/2}, F = 1\rangle \rightarrow |5P_{3/2}, F' = 2\rangle$ .

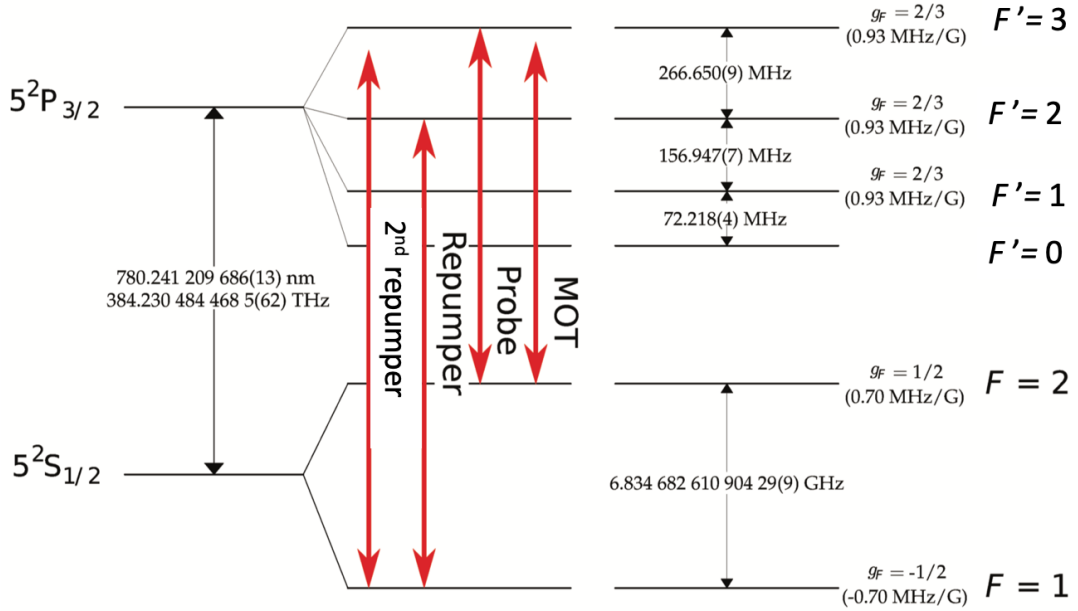


**Figure 2.1** — Hyperfine structure of the  $^{87}\text{Rb}$  D2 line. This is an adaptation of a graph available in ref [79].

To cool the rubidium atoms in a MOT, the following lasers are needed:

- A laser red-detuned from the cycling transition ( $|5S_{1/2}, F = 2\rangle \rightarrow |5P_{3/2}, F' = 3\rangle$ ). This laser will now be referred to as the cooling beam and is shown in Fig.2.1 as the red arrow labeled MOT.
- A laser resonant with the ( $F = 1 \rightarrow F' = 2$ ) transition. This beam will be referred to as the repumping beam, and the need for such a laser is explained in Sec.2.1.3

### 2.1.2 The laser sources

After having assessed the different needs to cool rubidium, here is a description of the different devices used on our experiment.

**MOT cooling laser:** In order to have enough power for magneto-optical trapping, a 10 W telecom laser at 1560 nm is frequency doubled through a single pass PPLN crystal. It delivers 1 W of usable output power at 780 nm. This laser had been developed locally, and the technical details can be found in Ref. [73]. The frequency is controlled using a beat note with a reference laser, enabling us to detune the frequency from resonance to tens of linewidths for cooling purposes. The beam is then divided into a part that goes to the 2D MOT and another part that goes to the 3D MOT. A small leak from a cube is used to produce a pushing beam that will direct the atoms from the 2D MOT chamber to the 3D MOT chamber.

**The reference laser:** A commercial NarrowDiode laser from Radiant Dyes provides a reference in frequency. It is an extended cavity diode laser, and it delivers 25 mW of light resonant with the  $|^5S_{1/2}, F = 2\rangle \rightarrow |^5P_{3/2}, F' = 3\rangle$  transition and a linewidth of 20 kHz. The laser is locked in frequency using a saturated absorption setup. It is also used for imaging purposes.

**Repumping lasers:** To repump the atom into the  $|^5S_{1/2}, F = 2\rangle$  state, the lasers used are Sanyo diode lasers specially calibrated to emit at 780 nm. Each diode delivers 50 mW and is placed in a temperature regulated Thorlabs box. The repumping beam used for the MOT is locked on the  $|^5S_{1/2}, F = 1\rangle \rightarrow |^5P_{3/2}, F' = 2\rangle$  transition via a saturated absorption setup.

### 2.1.3 Magneto-optical traps

These laser sources are used for trapping and imaging. The first type of trap used in the experiment is the magneto-optical trap. The basic idea is to have a magnetic field that depends on the position inside the trap to lift the hyperfine structure degeneracy and a pair of counter propagating lasers along an axis. The two laser beams have opposite circular polarization and are both red-detuned with respect to the cycling transition of the atoms. Because of this detuning, the atoms are not always resonant with the laser beams, which results in the beams pushing the atoms toward the zero of the magnetic field. By using a pair of counter-propagating laser beams in each direction, the experimentalist can trap the atom along each desired direction.

The first MOT is the 2D MOT with the rubidium source: a rubidium cell is heated in an oven at a temperature close to 70 °C. This source is directly linked to our 2D MOT chamber. This device has been designed at SYRTE and is composed of two pairs of elongated coils around the chamber in an anti-Helmholtz configuration and two orthogonal beams with elongated shapes that are retroreflected. The beams are circularly polarized and composed of both the repumping beam and the cooling beam. To direct the atoms from the 2D to the 3D MOT, we use a pushing beam of about 2 mW at the same wavelength as the 2D MOT beams. It results in the atoms being directed to the 3D MOT chamber through a small differential tube between the 2D MOT chamber and the 3D MOT chamber.

The second part of the experiment shown in Fig.2.2 is the vacuum chamber where the 3D MOT is installed. This chamber is an octagonal chamber with windows that let the laser pass through it. This is composed of three pairs of counter-propagating beams that are circularly polarized and come from the same source as the 2D MOT. The beams for the 3D MOT are done using a Shäfte-Kirchhoff fiber port cluster. The aim is to bring the cooling and repumping beam to the fiber port cluster and then mix the two incoming beams to produce three beams. When the MOT is fully loaded, there are around  $10^9$  atoms in the trapped vapor, with a pressure in the octagon close to  $10^{-9}$  mbar. A comprehensive presentation of

the MOT setup can be found in the references [73, 74]. The flow of atoms from the 2D MOT continuously loads the trap when a sequence is not running.

The third part of the experiment is the science cell, where the atoms are transported.

## 2.2 Magnetic transport, trapping and Bose-Einstein condensate production

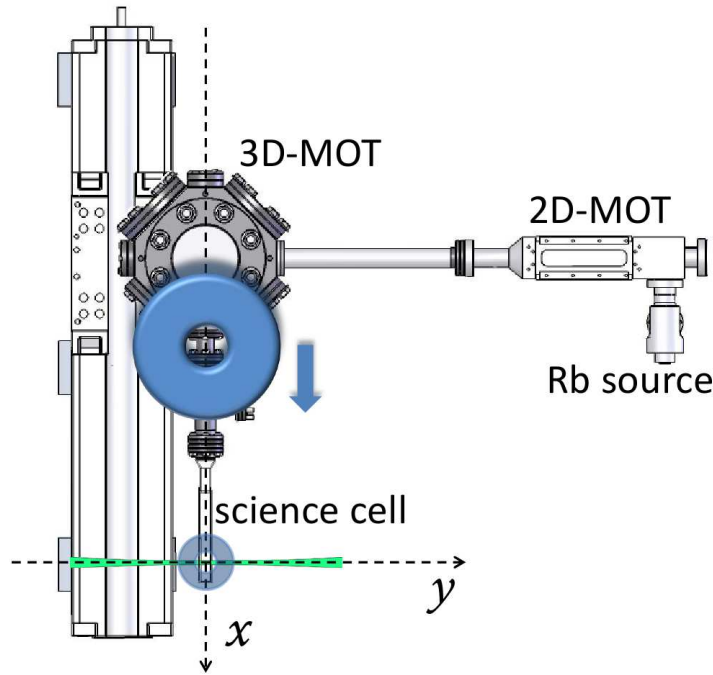


**Figure 2.2** — Sketch top view of the vacuum chambers of the experiment. One can see the connection between the 2D and 3D MOT chambers and the science cell. The blue blurry torus with an arrow next to it represents the MOT quadrupole coils, which slide along to the science cell. The green line represents the plug beam path, which is the same for the dimple beam. Figure taken from Ref. [80].

The science cell is a glass cell manufactured by Starna in quartz with a square section of  $10 \times 10$  mm and a depth of 83.5 mm. Each side has a thickness of 1.25 mm with a non-reflective coating.

### 2.2.1 Transport: how and why?

To obtain a BEC, the sequence lasts for up to a minute. The residual pressure in the 3D MOT chamber is  $10^{-9}$  mbar, ensuring a lifetime of an atom in the trap of 30 s. To improve this lifetime, the atoms are transported to the science cell, as presented in Fig. 2.2. Between the 3D MOT chamber and the science cell, there is a differential tube with a vacuum pump  $20 \text{ L} \cdot \text{s}^{-1}$ . The pressure in the science cell is  $10^{-11}$  mbar, with an associated lifetime of 150 s [73]. The transport is done by using a Parker translation stage 404XR, which can go up to a maximum

speed of  $1.2 \text{ m} \cdot \text{s}^{-1}$ , and has an accuracy of displacement of  $1.3 \mu\text{m}$ . The coils' current is provided by a Delta- Elektronika 15-400 A current supply. Because we are raising the current close to 400 A during one second, we need to cool down the coils. That is why the wires are hollow, and water is flowing through them, enabling efficient cooling.

Before the transport phase, the sequence starts by compressing the MOT by increasing the in-plane gradient from  $5.5 \text{ G} \cdot \text{cm}^{-1}$  (22 A) to  $20 \text{ G} \cdot \text{cm}^{-1}$  (90 A). In parallel, the cooling beam detuning increases, hence decreasing the effective repulsion between atoms due to multiple cycles of emission/absorption of photons inside the cloud. After that, the quadrupole coil current is switched off, and the cooling beam is further detuned in order to cool down atoms via molasses and Sisyphus cooling. Once this is done, the atoms are pumped into the state  $|F = 1\rangle$  by shutting down the repumping beam while the cooling beam is still on. The beams are then shut, and the current is switched back on to be ramped to  $87.5 \text{ G} \cdot \text{cm}^{-1}$  (350 A) in 150 ms. The atoms are ready to be moved to the science cell in a transport session that lasts 1 s. At the end of the transport phase, the atoms are loaded into a different quadrupole trap in the science cell with dedicated coils. After the transfer, the MOT coils slide back to their initial position, where they remain until the beginning of the next sequence. The science cell coils are conical, hollow, and water-cooled. They are close to the cell, allowing a maximum gradient of  $228 \text{ G} \cdot \text{cm}^{-1}$ .

### **2.2.2 RF evaporative cooling in a magnetic quadrupole trap: 1 problem with 2 distinct solutions**

#### **Evaporation in the quadrupole trap**

At the end of the transport phase, when the atoms are transferred to the quadrupole trap, the cloud has a temperature of  $150 \mu\text{K}$ . All the atoms are in the  $|m_F = -1\rangle$  state. This temperature is too high to reach Bose-Einstein condensation. In order to decrease the temperature and increase the phase-space density, two evaporative stages are performed. The evaporative cooling is done by shining a RF field, which couples to the Zeeman substates. When the coupling is resonant with the atoms having the most kinetic energy moving in the trap, these atoms transition to a non-trapping state and are thus ejected from the trap. By lowering the rf-field frequency slowly enough, the most energetic atoms are removed and the cloud rethermalizes to a lower temperature.

The evaporative cooling is split into two parts for a reason detailed in the next paragraph. The first part is done at the high magnetic field gradient value of  $225.9 \text{ G} \cdot \text{cm}^{-1}$ . The RF signal is generated by the same RF source as the dressing signal and is detailed in Sec.2.3 and the antenna is oriented along the  $y$ -axis. This first ramp is linear by part, starts at 65 MHz, finishes at 4 MHz and last 13.6 s. At the end of this stage, the temperature is  $20 \mu\text{K}$ , and we typically have  $8 \times 10^6$  atoms.

#### **Final Evaporation stage**

However, a problem remains: when the temperature of the cloud decreases, the atoms stay closer to the center of the trap, where they experience a smaller magnetic field gradient. In such a situation, the atoms can be lost by spin-flip transition: the magnetic field can not be followed adiabatically by the trapped atoms, resulting in a transition to non-trapping states. These transitions are also referred to as Majorana losses [81]. To avoid this situation, one needs to move the atom away from this region of the trap. There are two solutions: preventing the atoms from accessing this zone or attracting the atoms away from it.



A separate RF source is used, a Stanford SRS DS 345 with an antenna along the  $y$ -axis. The second ramp is linear and depends on the type of laser used to change the type of trap used.

### Repealing atoms from the quadrupole center: the plug technique

This is the first solution chosen to avoid Majorana losses. In our experiment, a blue detuned laser detailed in Sec.2.1.2 repeals the atoms from the center of the trap and therefore avoids Majorana losses around the trap center [81] enabling Bose-Einstein condensation. At the beginning of my PhD, this was done using a 10 W laser source with a waist of  $50\ \mu\text{m}$  in the atomic plane. It was later replaced by a 5 W laser with a beam waist estimated at  $34\ \mu\text{m}$  at the atom's position. The beam propagates along the  $y$ -axis as shown in Fig.2.3, and a comprehensive characterization of the trap is found in [74]. A special care was given to tune correctly the plug position controlled by a mirror with piezoelectric adjusters.

At the start of the evaporation ramp, after the transfer from the transport trap, the gradient is at its highest value at  $225.9\ \text{G}\cdot\text{cm}^{-1}$  (current at 110 A) This is to compress the cloud in order to maximize the collision rate. After a first radio-frequency ramp, the trap is decompressed to  $57.5\ \text{G}\cdot\text{cm}^{-1}$  (28.5 A). This is done to increase the plug effect on the atoms. Once the trap is decompressed, a second RF ramp is shone on the atoms to reach a lower temperature of 200 nK. At this stage, there are around  $4\times 10^5$  atoms total in the trap, with  $2\times 10^5$  condensed atoms.

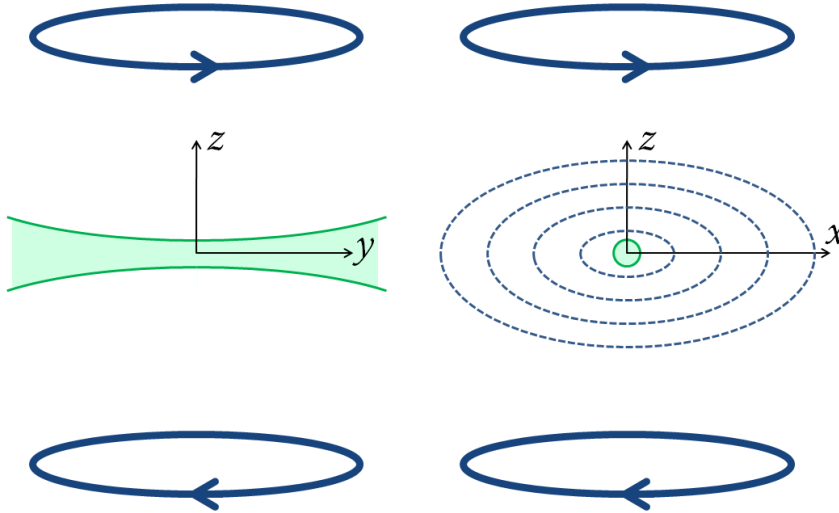


**Figure 2.3** – Representation of the plug beam path. The blue ellipses with arrows represent the quad coils, the dashed ellipses represent the iso-magnetic surface. The green part shows the plug beam which is centered around the center of the magnetic center of the trap. This figure is taken from ref [32].

### Attracting atoms away the quadrupole center: a red laser

Recently, we installed a new laser in the experiment and changed the trapping mechanism. Instead of repealing the atom from the center, a red detuned laser with  $\lambda = 1064\ \text{nm}$  is used to

attract the atom to a position with no Majorana losses. The beam is still propagating in the  $y$  direction and is off-centered with respect to the magnetic zero of our trap, as seen on Fig.2.4. This ensures the atoms are always subjected to a magnetic field sufficient to avoid Majorana losses. The main motivation to change the trapping mechanism was to avoid a shortcoming of the plug technique: the displacement of the cloud during the loading procedure of the dressed trap. As seen on Fig.2.6, the atoms move from point A to point B and this can imprint strong dipolar oscillations. The tuning of the plug position had to take this into consideration, and often the position minimizing the oscillation in the trap was not the one maximizing the number of atoms. This is no longer the case with the dimple beam: as the atoms are below the center of the quadrupole trap, the residual oscillation communicated to the atom during the loading is weak. The beam is slightly anisotrope, the waists are  $w_x=68.4\ \mu\text{m}$  and  $w_z=63.8\ \mu\text{m}$  with an effective power of 3.3 W around the atoms in the science cell. The strategy to have the largest BEC in the dressed trap will be detailed in Chap.5 and so far leads to a  $10^5$  atoms in the condensate and  $10^5$  thermal atoms.

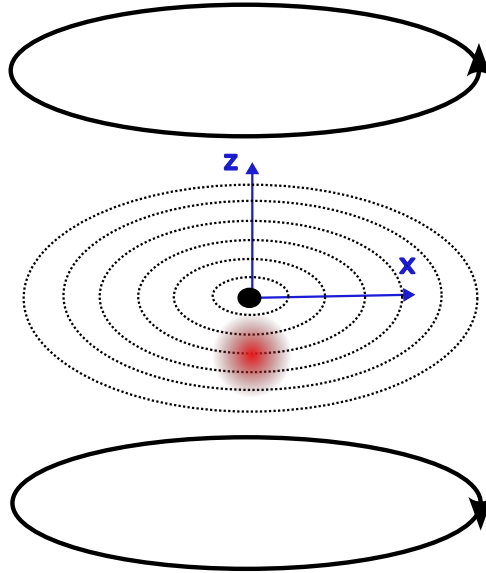


**Figure 2.4** — A sketch of the hybrid trap arising from the dimple beam and the magnetic quadrupole fields. The black ellipses with arrows represent the quad coils, and the dashed ellipses represent isomagnetic surfaces. The red circle represents the dimple beam, and the black spot represents the center of the trap. The dimple attracts the atom away from the center of the trap.

## 2.3 Radio-frequency fields and dressed trap loading

### Experimental setup

The specificity of our experiment is to study a Bose Einstein condensate inside a shell-shaped geometry. To obtain such a geometry, one needs to "dress" the atoms with RF fields as described in Chap.1 with RF fields. The RF field has a  $\sigma^-$  polarization onto the atoms, ensuring the rotational symmetry of the trap and the location of the hole at the very top of the bubble, as detailed in Chap.1. This field is produced via a set of three antennas, one along

each axis of the experiment as shown, in Fig.2.5. The field is obtained by having the two horizontal antennas (H1 and H2) along the x and y axes with a relative phase of  $\frac{\pi}{2}$  and with the same amplitude, which corresponds to a coupling amplitude  $\Omega_0$ . However, due to a slight tilt in the direction of each antenna, it has been proven next to impossible to obtain such an RF field only with the two in-plane antennas. To correct this small vertical component, a vertical antenna referred to as H3 has been installed.

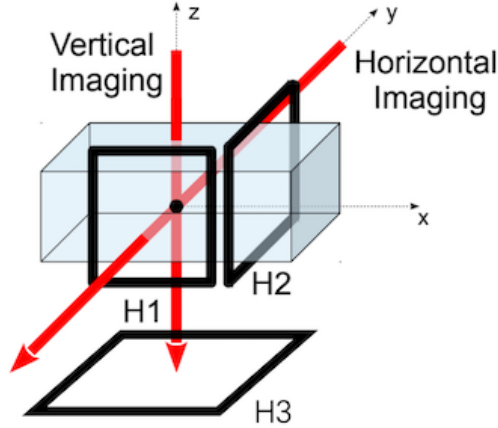


**Figure 2.5** – Representation of the dressing antennas around the science cell. Figure taken from [76].

To be able to load the atoms from the quadrupole trap into the dressed trap, one needs to have precise control over the amplitudes, frequencies, and phases of each signal. The signals are generated using a direct digital synthesizer (DDS) produced by the lab’s electronic workshop. This DDS has 8 channels, each with a 10-bit amplitude resolution, a 14-bit phase resolution, and a 32-bit frequency resolution. More specificities on the DDS control are available in the experiment control Chap.4, and a comprehensive characterization of the DDS can be found in [64].

### Dressed trap loading procedure

In this section, only the loading procedure for the plugged trap will be presented, as the procedure for the dimple trap is still unsettled. Some elements will be introduced in Chap.5, as they have been found using machine-learning algorithms. The numerical values for this section are given for the 5 W source that has been used to produce the results for the Chap.3.

Once a BEC is obtained in the hybrid trap described in Sec.2.2.2, the atomic cloud is transferred to the bubble shaped trap. At the start of the transfer, the atoms are off-centered from the quadrupole center at position A in Fig.2.6. This is due to the plug position: the atoms’ positions result in a trade-off between the magnetic gradient attracting atoms towards the trap center and the plug, which repels them from this center. The RF ramp starts by raising the amplitude in 5 ms while holding the frequency constant at 145 kHz. The atoms are far from the resonant surface of the given RF-field and should also be beneath the RF field’s first harmonic, not to be evaporated away. The cloud is in a position resonant with  $\omega_{rf} = 250$  kHz. The frequency is then ramped from 145 kHz to 490 kHz in 120 ms. The

change in frequency expands the bubble from  $37.7\ \mu\text{m}$  to  $127.4\ \mu\text{m}$ , resulting in the atoms being localized at the surface of the bubble. The RF frequency is decreased to  $300\ \text{kHz}$  in  $175\ \text{ms}$ , which corresponds to a horizontal radius of  $78\ \mu\text{m}$ . In parallel, we decrease the plug power from maximum power to complete shutdown in  $150\ \text{ms}$ ; this ramp starts at the very start of the dressing ramp. At the end of the transfer, the cloud reaches the B position on Fig.2.6. The crucial point during the procedure is to avoid importing dipolar oscillations into the dressed trap during the bubble expansion. This is done through the position tuning of the blue detuned plug beam and the slow second part of the dressing ramp.

On top of the dressing coils, there are three coils dedicated to canceling the residual magnetic fields near the atoms. They are referred to as the compensation coils and have been carefully calibrated. This is because during the evaporative cooling phase, there is a change in the magnetic gradient. If there is an offset in the magnetic field, the positions of the trap centers at high gradient and low gradient are different. This results in exciting the dipolar oscillations of the cloud inside the trap when the magnetic gradient is decreased. After having carefully calibrated the coils, the remaining oscillation amplitude after loading the atoms in the dressed trap is smaller than  $4\ \mu\text{m}$ .

To maintain the cloud at a low temperature, a RF knife is added to the dressing ramp, which is an RF signal of small amplitude added on top of the dressing signal. The RF signal is generated with the same DDS as the dressing signal and is sent to the vertical dressing antenna. It is polarized linearly along the  $z$ -axis with a frequency  $100\ \text{kHz}$  above the dressed trap bottom  $\Omega_0$ . During the first linear ramp of the dressing part, the frequency is lowered to  $20\ \text{kHz}$  above the dressed trap bottom at the end of the ramp.

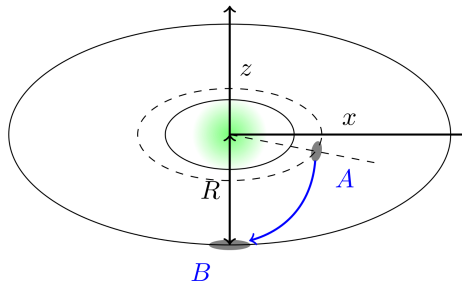


**Figure 2.6** – Schematic representation of the loading procedure with a plugged trap. The atoms start at position A. The bubble expands, and the atoms are resonantly dressed. The atoms fall at the bottom of the trap in position B. Figure taken from [74].

## 2.4 Imaging the atomic cloud

At the end of a sequence, and regardless of the type of cloud, we want to visualize the atomic density. To do so, we are taking an absorption picture that we extract information from. For example, we can extract the number of atoms or the temperature. The main idea here is to be able to compare as accurately as possible an image with atoms and another one without them. To do so, we need to take three pictures: one with atoms and light, one without atoms but with a light pulse, and one with neither atoms nor light pulse to evaluate the noise on the camera. The imaging light pulses are resonant with the ( $|^5S_{1/2}, F = 2\rangle \rightarrow |^5P_{3/2}, F' = 3\rangle$ ) transition, and the beam is circularly polarized. This is the cycling transition used for the

MOT in order to have a two-level system. It should be stressed that this imaging process destroys the BEC.

In the following derivation, the probe is along the  $z$  axis, detuned by  $\delta$  with respect to the transition mentioned previously, which has a spectral width of  $\Gamma = 2\pi \times 5.89$  MHz. The starting point is the Beer-Lambert law along the  $z$ -direction, which gives the optical density  $D_z(x, y)$  in the  $x-y$  plane:

$$D_z(x, y) = -\ln\left(\frac{I_t(x, y)}{I_i(x, y)}\right) \quad (2.1)$$

where  $I_t(x, y)$  is the transmitted intensity and  $I_i(x, y)$  is the incident intensity.

This law relies on the low intensity hypothesis: the incident intensity is smaller than the saturation intensity,  $I_{sat} = \frac{\hbar\omega_{probe}\Gamma}{2\sigma_0}$ . Where the absorption cross-section of a photon is  $\sigma_0 = \frac{3\lambda^2}{2\pi}$  and  $\omega_{probe}$  is the frequency of the transition. All these expressions describe well the dilute media situation: the situation where the interaction between a photon and an atom is independent of the other atoms. It is the case where  $\sigma$  is independent of the intensity  $I$ . In that case, the optical density of the cloud is linked to the atomic density  $n_0$ :

$$D_z(x, y) = \sigma \int n_0(x, y, z) dz = \sigma n(x, y) \quad (2.2)$$

When the intensity of the beam is lower than the saturation intensity ( $I \ll I_{sat}$ ), the effective absorption cross-section of the probe beam is:

$$\sigma = \frac{\sigma_0}{1 + \frac{4\delta^2}{\Gamma^2}} \quad (2.3)$$

Ultimately, one can deduce the atomic integrated density in the  $x-y$  plane as follows:

$$n(x, y) = -\frac{1}{\sigma} \ln\left(\frac{I_t(x, y)}{I_i(x, y)}\right) \quad (2.4)$$

This does not depict accurately the physical situation of the experiment because either a cold atom cloud or a Bose-Einstein condensate can be denser than what is described by the "dilute media hypothesis". The risk here, if you use a low intensity beam probe, is for the beam to be completely absorbed and therefore not have meaningful information to extract. To have a better description, we have to explain what happens when a higher intensity probe is used [64, 75, 82]. In such a situation, the absorption cross-section becomes  $\sigma(I) = \frac{\sigma_0}{c^* + \frac{I}{I_{sat}}}$  in such situation. Following this change, the integrated atomic density becomes:

$$\sigma_0 n(x, y) = -c^* \ln\left(\frac{I_t(x, y)}{I_i(x, y)}\right) + \frac{I_t(x, y) - I_i(x, y)}{I_{sat}} \quad (2.5)$$

There is two different contributions. The first term modifies the Beer-Lambert law by adding a dimensionless constant  $c^*$  that encompasses the deviation from the ideal two-level system [64]. The second term depends directly on the probe beam intensity with and without atoms and takes into account the multiple absorptions of a single photon. A more comprehensive discussion can be found in [64, 75], and to use this expression, one needs to calibrate the  $c^*$ . This procedure is detailed in ref. [64]. The general picture having been set, now we will detail the specificity of the horizontal and vertical imaging systems.

### 2.4.1 Horizontal imaging

Because the atoms are trapped and spin-polarized in the ground state  $|^5S_{1/2}, F = 1\rangle$ , we first need to pump them into the  $|^5S_{1/2}, F = 2\rangle$  state, to probe the cycling transition. To do so, a 100  $\mu\text{s}$  pulse of the repumping laser resonant with the  $(|^5S_{1/2}, F = 1\rangle \rightarrow |^5P_{3/2}, F = 2\rangle)$  transition is sent to pump the atoms into the  $F = 2$  state. After that, a probe resonant with  $(|^5S_{1/2}, F = 2\rangle \rightarrow |^5P_{3/2}, F = 3\rangle)$  is sent on the atoms. The pulses are 17  $\mu\text{s}$  long, with a waist of 2.7 mm along the y-axis. There are two pulses: one with the atoms, called the probe, and one without the atoms, called the reference.

The camera used is an iXon 885D EMCCD camera from Andor, with a 1004x1002 pixel matrix and a pixel size of  $8 \times 8 \mu\text{m}^2$ . After the two-images have been taken, a third image is taken without light in order to record the noise on the camera detector. Also, an interferential filter has been put on the camera in order to block a leak from the plug/dimple beam from reaching the camera detector. Then a two-lens imaging system enables zooming in on the atoms. This system has a magnification coefficient of  $G = 2.17$ . The horizontal camera setup performs time-of-flight imaging, and the time of flight used for the hybride trap or the dressed trap is usually  $\Delta t = 23$  ms.

### 2.4.2 Vertical imaging

For the vertical imaging system, the situation is slightly different. Two different cases should be distinguished: in-situ imaging and time-of-flight imaging. Time-of-flight imaging is done in the same fashion as horizontal imaging. However, for in-situ vertical imaging, the cloud is too dense to be imaged in that way. If the resonant repumping beam is used, only a small fraction of the first atoms will absorb the repumping beam. This will result in a distorted-looking cloud on the image. In order to avoid this situation, a second repumping beam is used. To do so, the frequency of a second laser is locked via beat note with the resonant repumping beam and can be detuned up to 500 MHz. This second beam is usually used exclusively for this imaging purpose. This beam is detuned from the  $|^5S_{1/2}, F = 1\rangle \rightarrow |^5P_{3/2}, F = 2\rangle$  transition of 250 MHz corresponding to a detuning of  $42\Gamma$ . This lower absorption cross-section allows for uniform absorption across the whole cloud.

For the camera, we use a Luca-R EMCCD from Andor with a 1004x1002 pixel matrix and a pixel size of  $8 \times 8 \mu\text{m}^2$ . The vertical imaging has been designed in order to do some in-situ imaging, hence, it requires a greater magnification than the horizontal imaging. Therefore, a four-lens setup is installed to reach a magnification of  $G = 8.4$  with a depth of focus of approximately 70  $\mu\text{m}$ .

Depending on the time of flight deviation, it is crucial to adjust the vertical focus plane. The whole system (camera and telescopes) is then mounted on a three-axis micrometric translation plate, allowing a vertical translation of the bubble imaging setup.

### 2.4.3 Stern-Gerlach procedure

As seen in Chap.1, the dressed state the atoms are trapped in is a linear combination of the Zeeman substates. Therefore, when we shut down the radiofrequency field, the atoms are projected onto the different bare substates. A residual gradient in the static magnetic field can disrupt the imaging process, resulting in the splitting of the cloud into three clouds that overlap each other. The fit applied to the picture can no longer be relevant for the data to be analyzed. One can then choose to isolate the  $m_F = 0$  component, which is unaffected by the

magnetic fields, to perform a relevant fit. The procedure is different for the horizontal and vertical imaging setups.

Let us start by detailing the horizontal case. A delay is induced between the time at which the radiofrequency is switched off and the time the current in the quadrupole coils is switched off. This delay exposes the different bare states to different accelerations. The  $|m_F = 0\rangle$  is not accelerated, whereas the  $|m_F = 1\rangle$  is repealed from the center and the  $|m_F = -1\rangle$  dragged to the center. This physically separates the three sublevels.

For the vertical imaging setup, the situation is different. The three clouds fall along the vertical axis, so to separate them would result in having one cloud out of focus, preventing the experimentalist from seeing the two other clouds. In order to be able to have a full picture of the cloud, the principle is different. All the atoms are adiabatically transferred to the state  $m_F = +1$  by slowly changing the RF fields' dressing frequency in comparison with  $\Omega_0$  but quickly compared with  $\omega_z$ . Then the current in the quadrupole is shut and then the time of flight imaging procedure is performed. This results in having a single cloud even in the presence of a residual gradient. This procedure has been developed when imaging vortex lattices in order to increase the visibility of each vortex. As the analysis of this work has not yet been completed, it is beyond the scope of this PhD and will be developed elsewhere.

#### 2.4.4 Conclusion

In this chapter, the experimental setup has been detailed. At the very beginning, the atoms are evaporated in an oven and then trapped in a 2D MOT. This 2D MOT continuously loads a 3D MOT in a separate vacuum chamber.

Once the 3D MOT is loaded, an experimental sequence can be launched to obtain a Bose-Einstein condensate. The first experimental step is to prepare the atoms for transport. This is accomplished by cooling them, pumping them into the state  $|^5S_{1/2}, F = 1\rangle$ , and loading them in a purely magnetic trap. In order to observe a condensate, we need to physically transport the atoms to the "science cell", a glass cell under higher vacuum, enabling better optical access to the atoms. To cool the atom down, a two-step evaporative cooling phase is performed, which leads to a BEC. Ultimately, the atoms form a BEC that is loaded inside a quadrupole-dressed trap.

At the end of the sequence, an imaging sequence is performed either along the horizontal  $y$ -axis or the vertical axis. To interpret this image, the model used takes into account the high intensity of the probe.

# Chapter 3

## Gravity compensation in the dressed quadrupole trap: spontaneous appearance of a ring-shaped BEC

To end this part, the last study done with the former control system is presented: the gravity compensation inside the dressed quadrupole trap. Working in a low-gravity environment has gained momentum in the cold atom community with initiatives such as the Cold Atom Lab (CAL) on the International Space Station (ISS). The trap in the ISS [83] is designed to trap and cool rubidium and potassium with appropriate cooling techniques [84] and the possibility of a bubble-shaped trap [85]. This microgravity environment has consequences for the BEC, such as modification of the collective modes at the surface of the bubble [28] and the critical temperature at which the BKT transition happens. Vortex-antivortex pairs have interesting properties, such as displaying long-range attraction [86]. Being able to cancel the effect of gravity on Earth has also been the subject of scientific investigations with means as different as a drop tower [87], linear optical potential [88,89] or canceling gravity by compensating the magnetic field gradient [90].

The chapter is a description of an original way to achieve gravity cancellation in the quadrupole-dressed trap. It will begin with an explanation of the gravity compensation mechanism that motivates the experimental work and an explanation of the spontaneous formation of a ring. Then, a first conclusion is drawn from the first results obtained during Yanliang Guo's thesis [76]. The experimental strategy had been rethought and will be presented in the second section, which ends with a presentation of the radio-frequency tuning, a pivotal part of the preparation. In the last section, we present a comparison of the results with a theoretical analysis and discuss the homogeneity of the ring.

### 3.1 Gravity compensation mechanism and first results

#### 3.1.1 Gravity compensation mechanism

The trap used for this study, and described in Chap.1, has a bubble shape squeezed along the vertical axis. To have a maximum of coupling amplitude at the very bottom of the bubble and only one hole, the RF field has to be polarized circularly along the  $z$ -axis with



a  $\sigma^-$  polarization. In that case, the expression of the potential within the rotating wave approximation for atoms sitting exactly on the resonant surface is given by:

$$V_{trap}(z) = \frac{\hbar\Omega_0}{2} \left(1 - \frac{2z}{r_b}\right) + Mg z \quad (3.1)$$

Where  $\Omega_0$  is the maximum of RF coupling and  $r_b$  is the semi-major radius of the bubble in the equatorial plane. One can see three different contributions in (3.1), but only the  $z$ -dependent terms will be detailed in the following paragraph. Gravity pulls the atoms toward the bottom of the trap, whereas the  $z$ -dependent term in the coupling attracts the atom to the top. Another expression for  $V_{trap}(z)$  is:

$$V_{trap}(z) = \frac{\hbar\Omega_0}{2} + \left(Mg - \frac{\hbar\Omega_0}{r_b}\right) z \quad (3.2)$$

$$(3.3)$$

In the previous expression, the expression of  $r_b$  is given by (1.26). To be in a microgravity environment in the trap states means that the gravity is compensated by the attraction of the atoms toward the hole. This condition can be written as:

$$Mg = \frac{\hbar\Omega_0}{r_b} \quad \longrightarrow \quad \Omega_0 = \frac{Mg}{\hbar} r_b = \frac{Mg\omega_{rf}}{\hbar\alpha} \quad (3.4)$$

So to compensate the gravity with a fixed RF field frequency, the parameters one can tune are the magnetic field gradient  $\alpha$  of the trap and the maximum Rabi-coupling  $\Omega_0$ .

### 3.1.2 Spontaneous formation of ring shaped Bose-Einstein condensate

As observed by Yanliang Guo during his PhD [76] on this experiment, when gravity is compensated, the atoms spontaneously form a ring in the trap. This is because the previous description of the system lacks an element: the transverse confinement of the trap. In the direction transverse to the bubble, the Bose-Einstein condensate lies at the fundamental level of the dressed trap in the quasi-2D regime. This trap can be described locally as harmonic, and as such, one has to take into account the zero-point energy. A description of the zero-point energy must be given, and this term is expressed as  $\frac{\hbar\omega_{\perp}(z)}{2}$ . By recalling the results of Sec.1.1.2 and reformulating its results [76]:

$$\omega_{\perp}(z) = \alpha(z) \sqrt{\frac{\hbar}{M\Omega(z)}} \quad (3.5)$$

$$\text{with } \alpha(z) = \alpha \sqrt{1 + \frac{12z^2}{r_b^2}} \quad (3.6)$$

These expressions state that the transverse confinement is not homogeneous, implying changes in the zero-point energy. A close look at the expression (3.5) tells us that the transverse confinement diverges at the very top of the bubble. This is because it is the point where  $\Omega$  vanishes. Instead of looking at the position on the ellipsoid compressed along the  $z$ -axis, it is more convenient to look at the position on a sphere, as detailed in Sec.1.1.2. The dependencies on the angle  $\phi$  have been dropped as the trap is invariant with respect to the rotation around the  $z$ -axis, To avoid any confusion with the time  $t$ , the graphical representation of  $t$  has been

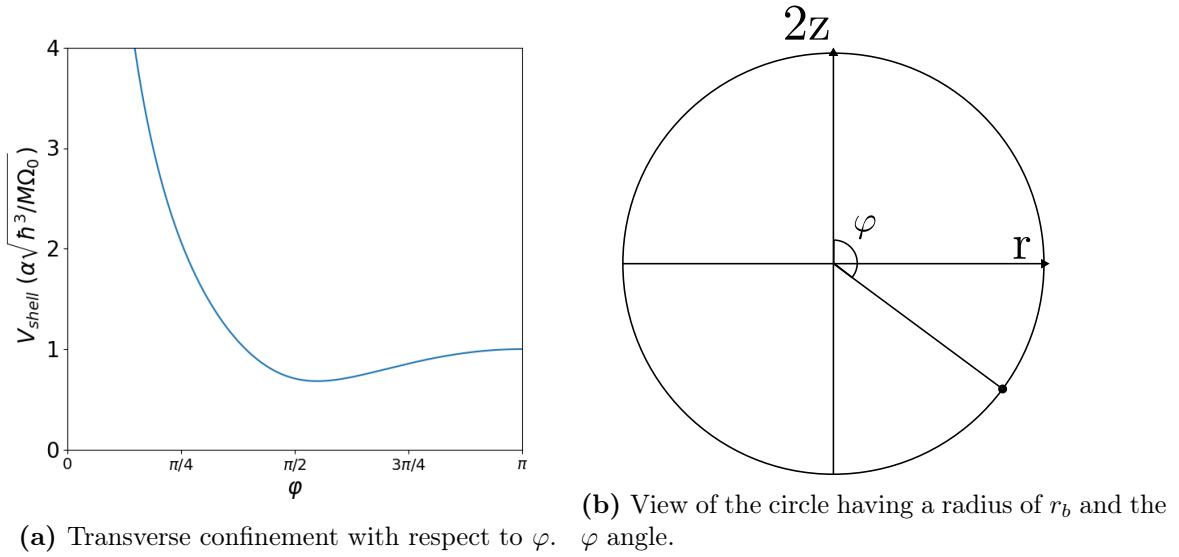


**Figure 3.1** — Transverse confinement representation. These figures are taken from [76].

replaced by  $\varphi$  for clarity's sake. The expression of the full shell potential with respect to  $\varphi$  is given by [76]:

$$V_{shell}(\varphi) = \frac{\hbar\Omega_0}{2} + \left( \frac{\omega_{rf} Mg}{\alpha} - \hbar\Omega_0 \right) \frac{\cos(\varphi)}{2} + \hbar\alpha \sqrt{\frac{\hbar}{M\Omega_0}} \frac{\sqrt{5 + \cos(2\varphi)}}{\sqrt{8} \sin(\frac{\varphi}{2})} \quad (3.7)$$

When the microgravity condition is met, the second term of the equation above cancels, and the transverse confinement variations become dominant. This last term, plotted in Fig.3.1a, has a minimum for  $\varphi = 0.55\pi$ , slightly below the bubble equator. The model described here shows how the atoms form a ring: when gravity is cancelled, the transverse confinement has a minimum, which is where the atoms stay.

## 3.2 Experimental sequence and measurements

Now that the principle has been established, this is the time to give more details about the experimental work done to observe the microgravity regime. This work was done to complete what was started by Yanliang Guo during his PhD [76]. This section will start with a presentation of the first measurements done during Yanliang Guo's PhD time, their limitations, and how the experimental strategy has been modified. After that, the RF field tuning method will be explained.

### 3.2.1 Strategy and sequence description

One must recall that the semi-major radius of the bubble is given by  $r_b = \frac{\omega_{rf}}{\alpha}$  as stated in Chap.1. As the microgravity condition stated in Eq.(3.4), to cancel gravity, one must either increase  $\Omega_0$  or decrease  $r_b$ .

The first measurement during Y. Guo thesis was done by raising the magnetic field gradient. To perform this set of measurements, the gravity compensation sequence started with a BEC loaded in the bubble trap with a gradient of  $\alpha/2\pi = 4.14 \text{ kHz} \cdot \mu\text{m}^{-1}$  with a circularly polarized rf-field along the  $z$ -axis at  $\omega_{rf}/2\pi = 300 \text{ kHz}$  and a fixed maximum coupling

amplitude. The gradient is then ramped up to a larger final value in 300 ms, decreasing  $r_b$ . At the end of the ramp, the trap is switched off, an image is taken by the horizontal camera after a time of flight expansion via absorption imaging technique, and the number of atoms is measured. We observe a dramatic fall of the atom number in the trap when  $r_b$  is below a given threshold that depends on the maximum Rabi coupling [76]. As the atoms are able to explore the full ellipsoid surface, they spend more time close to the top of the bubble, resulting in increased Majorana losses.

A second set of measurements has been done to look at the atomic distribution inside the trap. This time the maximum Rabi coupling,  $\Omega_0$ , was increased at a fixed gradient. Once the atoms are transferred in the bubble trap,  $\Omega_0$  is raised to a final value between  $2\pi \times 79$  kHz and  $2\pi \times 112.6$  kHz. An in-situ image along the vertical axis is taken at the end of the sequence. The results of these measurements were the observation of a ring-shaped atomic cloud, but the estimation of the gravity compensation threshold was incorrect. Therefore, the model developed in Sec.3.1.2 is valid qualitatively, but the experimentally observed threshold was slightly different from the threshold deduced from the model developed in Sec.3.1.2. An important drawback of this method is the requirement of doing an RF polarization tuning for each  $\Omega_0$  value.

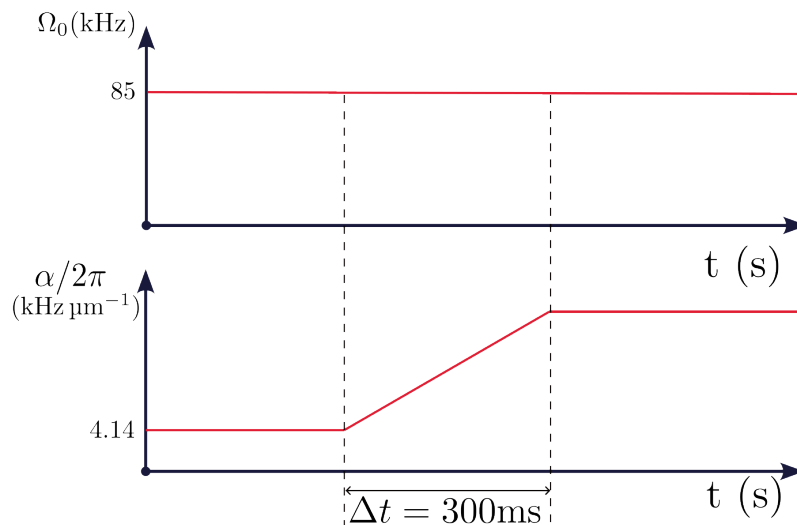


**Figure 3.2** – Schematic representation of the evolution of the maximum coupling and the coupling gradient during the sequence used for the second round of data collection. The maximum coupling amplitude remains constant. The coupling gradient starts at low value ( $\alpha/2\pi = 4.14$  kHz  $\cdot$   $\mu\text{m}^{-1}$ ) and is raised at a higher final value.

To complete our study, we were interested in a systematic study of the whole ring formation pattern. The conclusion from previous sets of measurements was that we observed an inhomogeneous ring. We used the same experimental sequence as the one for the first set of measurements and we used the imaging system along the vertical axis in the in-situ condition. The sequence, displayed in Fig.3.2, starts with a bubble trap loaded with a BEC. The radiofrequency field is circularly polarized with a frequency of 300 kHz and a maximum Rabi coupling of 85 kHz. The gravity compensation condition (3.4) gives a magnetic gradient

value of  $7.54 \text{ kHz} \cdot \mu\text{m}^{-1}$ . Once the atoms are loaded in the trap, the gradient is ramped to a final value in 300 ms. The result of this set of measurements is displayed in Fig.3.3

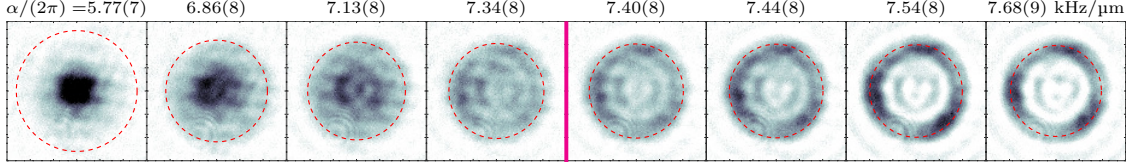


**Figure 3.3** – Formation of the ring-shaped BEC when the gravity is compensated by increasing the magnetic field gradient value. The pink line represents the value at which the gravity is compensated. This figure is taken from ref. [37]

### 3.2.2 Calibration of the radiofrequency field

The key element to observing the ring when gravity is compensated is the radiofrequency field tuning. Let us first give the expression of the magnetic field related to the RF field:

$$\mathbf{B}_{\text{rf}}(t) = B_x \cos(\omega_{\text{rf}}t + \phi_x) \mathbf{e}_x + B_y \cos(\omega_{\text{rf}}t + \phi_y) \mathbf{e}_y + B_z \cos(\omega_{\text{rf}}t + \phi_z) \mathbf{e}_z \quad (3.8)$$

To observe the ring, the polarization must be  $\sigma_-$  along the  $z$ -axis. This translates to  $B_x = B_y$  for the amplitude of the magnetic fields in the  $x - y$  plane and a phase difference of these fields of  $\phi_y - \phi_x = -\frac{\pi}{2}$ . The magnetic field should be zero along the  $z$ -axis, so  $B_z = 0$ . In order to achieve this polarization, there are three different dressing antennas, one along each axis of the experiment, as described in Chap.2.

On a theoretical level, assuming the rf field produced by a coil is homogeneous, one would need only two coils to generate an elliptically polarized rf field in the  $x - y$  plane. However, the experimental situation has been proven more complex during Mathieu de Goër's PhD [64]. The problem comes from the alignment of each coil: there is a small tilt for each axis such that each coil produces a field that is not strictly aligned with the  $x$ ,  $y$  and  $z$ -axis.

To account for these misalignments, the field produced by each antenna is along a vector noted  $\mathbf{u}_i$ , which is different from the Cartesian basis vector  $\mathbf{e}_i$ . The amplitude of the antenna along the axes  $\mathbf{e}_x$  and  $\mathbf{e}_y$  should be the same, but as the antennas are slightly different and the fields are produced along  $\mathbf{u}_x$  and  $\mathbf{u}_y$ , an amplitude correction  $\delta_B$  is introduced. This also applies to the phase difference between these two antennas, which also requires a phase correction,  $\delta_\phi$ . Furthermore, the two previously mentioned coils produce together a small field along the axis  $\mathbf{e}_z$ . This is compensated by the field  $-B_z \cos(\omega_{\text{rf}}t + \phi_z)$  along the  $\mathbf{u}_z$  axis. This coil will be referred to as the vertical antenna. Using these new parameters, one can write Eq.(3.8) for a  $\sigma^-$  polarization, which becomes:

$$\mathbf{B}_{\text{rf}}(t) = B(1 + \delta_B) \cos(\omega_{\text{rf}}t) \mathbf{u}_x + B(1 - \delta_B) \cos(\omega_{\text{rf}}t - \frac{\pi}{2} + \delta_\phi) \mathbf{u}_y - B_z \cos(\omega_{\text{rf}}t + \phi_z) \mathbf{u}_z \quad (3.9)$$

In this expression, the following parameters need to be tuned:

- $\delta_B$  - the amplitude correction in the plane.
- $\delta_\phi$  - the phase correction in the plane.
- $B_z$  - the amplitude of the vertical antenna.

- $\phi_z$  - the phase of the vertical antenna.

The initial tuning had been done following the procedure described in Yanliang Guo's PhD thesis [76], beginning with an unknown polarization close to  $\sigma^-$ . The procedure can be summarized as follows: first,  $\phi_z$  and  $B_z$  are changed in order to obtain two well-balanced spots. As detailed in Sec.1.1.2, when the polarization is elliptical, there are two holes attracting the atoms. This step is detailed in Sec.3.2.2 and aims to set the polarization of the rf-field in the  $x - y$  plane by tuning  $B_z$  and  $\phi_z$ . Once this is done, the polarization is elliptic in the  $x - y$  plane and the goal is now to obtain a circular polarization. The procedure is detailed in Sec.3.2.2 and tunes  $\delta_B$  and  $\delta_\phi$  correctly. After this two-step procedure, the atoms are spread as uniformly as possible along the circle's circumference.

For this procedure to work, the magnetic gradient has to be large enough to observe a ring when the RF field is well tuned. The BEC is then located at the potential minimum described in Eq.(3.7). A shortcoming of this procedure is that the tuning is done at a high value of magnetic gradient. The tuning of the RF field to ensure the most uniform atomic distribution was slightly different for lower magnetic gradient values. For instance, a set of parameters displaying an almost uniform distribution of the atoms along the circle's circumference when the atoms are at the bubble's equator might show an unbalanced cloud when the atoms are located at the bottom of the trap. Therefore, Yanliang Guo's method to tune the RF field needs to be corrected, and as such, the effects of each parameter change on the atomic distribution are described. A mathematical description of these changes is found in ref. [91].

### Tuning of the vertical antenna

The first parameters we changed in the previous method were those related to the vertical antenna.  $B_z$  and  $\phi_z$  exhibit two different behaviors that are easy to identify and distinguish.

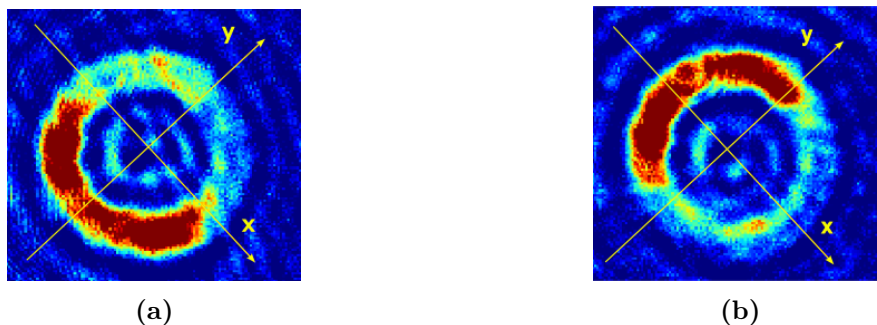


**Figure 3.4** — Illustration of changes in vertical antenna parameters. Fig.a represents the situation where the vertical amplitude is too high, resulting in atoms accumulating on the bottom left part. Fig.b represents the situation where the phase of the vertical antenna is too high, resulting in atoms accumulating on the top left.

But before that, the first step is to describe the physical situation prior to the tuning. The polarization is close to circular but slightly elliptical. The consequence for the atoms is the existence of two holes they are attracted to. When gravity is compensated, this results in having two clouds of atoms that are small and dense. The first step to tuning the RF parameters is to bring the RF polarization into the  $x - y$  plane. This is accomplished by

adjusting the parameters  $B_z$  and  $\phi_z$ . When the polarization is elliptic in the  $x - y$  plane, it results in two holes symmetric with respect to the  $z$ -axis, as described in Sec.1.1.2. The effect on the atoms is to have two clouds of atoms of the same size along the diameter of the circle.

Each parameter controlling the RF field generated by the vertical antenna has a different role. On the one hand,  $B_z$  tunes the balance of the two different spots along an axis going from the top right to the bottom left of the images based on the camera's orientation. When it is poorly tuned, either the atoms accumulate on the top right of the circles when  $B_z$  is too large or on the bottom left when it is too small.

On the other hand, there is the tuning of  $\phi_z$ , which modifies the alignment of the axis formed by the two clouds of atoms. When  $\phi_z$  is too small, the atoms accumulate at the upper left corner of the image; when this parameter is too large, the atoms accumulate at the lower right corner of the circle. These two axes are not arbitrary: they are the two axes along which the antennas in the  $x - y$  plane are oriented.

### Tuning of the in-plane antennas

Once the parameters related to the vertical antenna are correctly tuned, two clouds of similar size along the radius of a circle are observed. It indicates that the RF field's polarization is elliptic and in the  $x - y$  plane. The motivation for this tuning is to pass from an elliptic to a circular polarization. The starting point to tune the parameters  $\delta_\phi$  and  $\delta_B$  is two well balanced spots of atoms.



**Figure 3.5** — Representation of the change in parameters for the in-plane antennas. Fig.a is what happens when  $\delta_\phi$  is not well tuned and the axis between the 2 spots is not along the circle diameter. Fig.b shows a picture where  $\delta_B$  is not well tuned, hence having two spots of atoms.

The starting point to describe the behavior of the atoms is the link between the parameters of the RF field and the holes positions, which is given by Eq.(1.48) of Chap.1. The angle  $\phi$  describes the orientation of the axis defined by the two holes, which is oriented in the  $x - y$  plane. A direct consequence of having two distinct holes is to have two separate clouds of atoms around the circumference of the circle [76]. As each cloud is attracted towards one hole, the  $\phi$  angle also describes the angle between the axis of the antenna and the axes of the two atom clouds:

$$\phi = \frac{1}{2} \arctan(\tan(2\Theta) \cos(\Phi)) \quad (3.10)$$

The  $\Theta$  parameter controls the balance between the antenna generating the RF field along  $\mathbf{u}_x$  and the one generating the RF field along  $\mathbf{u}_y$ .  $\Phi$  is the difference in phase between the two antennas. Given that the desired polarization state is  $\sigma^-$  along the  $z$ -axis,  $\Theta$  has a value close to  $\pi/4$  and  $\Phi$  has a value close to  $\pi/2$ , resulting in  $\Theta = \pi/4 + \delta\Theta$  and  $\Phi = \pi/2 + \delta\Phi$ . Taking this into account and assuming only minor corrections are required, the expression of  $\phi$  is as follows:

$$\phi = \frac{1}{2} \arctan\left(\frac{\sin(\delta\Phi)}{\tan(2\delta\Theta)}\right) \simeq \frac{1}{2} \arctan\left(\frac{\delta\Phi}{2\delta\Theta}\right) \quad (3.11)$$

Eq.(3.11) shows that for a fixed value of the amplitude difference  $\delta\Theta$ , the two clouds rotate along the circle, resulting in a change in the  $\phi$ . The angle  $\phi$  depends on  $\delta\Phi$  with an arctangent behavior. This means the angle value goes from a lower value to an upper value, passing through zero in a certain interval. This interval depends directly on the value of  $\delta\Theta$ , and when the two amplitudes are well-balanced, the two clouds rotate extremely quickly in relation to the phase difference  $\delta\Phi$ .

That is why our goal is to experimentally minimize the width of variation needed to pass from the axis of one antenna to the axis of the other antenna. The value of  $\delta_\phi$  is scanned for each value of  $\delta_B$ . When  $\delta_\phi$  is far detuned, the two atom clouds align along the axis of one of the coils, either  $\mathbf{u}_x$  or  $\mathbf{u}_y$ . During the scan of  $\delta_\phi$ , the span to pass from one axis to the other is noted. The value that minimizes the width of variation is then used.

In practice, one might need to change the value a little for balancing purposes. Indeed, as gravity is gradually compensated, the correct value for the ring-shaped BEC at the bubble's equator can differ slightly from the value of  $\delta\Theta$  for a pancake BEC when the gravity is only partially compensated. Therefore, it is useful to have a phenomenological model of how a change with respect to a certain parameter affects the cloud.

When  $\delta_B$  is too low, the atoms are on the bottom left to top right axis, and when this parameter is too high, the atoms are aligned on the top left to bottom right axis. Because the vertical antenna parameters have been tuned, there are two balanced spots with atoms that are diametrically opposed on the circle, and tuning this parameter will make this axis rotate. For example, in Fig.3.5b, the parameters related to the vertical antenna are well tuned as the two clouds align with the radius of the circle, but  $\delta_B$  is slightly detuned because the axis formed by the clouds is close to the  $\mathbf{u}_x$  axis.

After that, only one parameter needs to be adjusted:  $\delta_\phi$ . This parameter controls the way the atoms spread along the circle's circumference. Starting with a tuned  $\delta_B$ , when  $\delta_\phi$  is far detuned, there are two distinct clouds, whereas when it has the right value, the atoms are almost uniformly distributed along the circle. The idea here is to spread the atoms as uniformly as possible along the circle's circumference. An example of the situation needing to be tuned is given in Fig.3.5a. One can see the two clouds are well balanced in terms of number of atoms, but they do not spread along the circle's circumference.

### 3.2.3 Calibration of the magnetic gradient of the quadrupole trap

The ellipsoid radius depends on  $\alpha$ , the magnetic gradient value, as expressed in Chap.1. This magnetic gradient behaves linearly with respect to the current:  $\alpha = CI$ , and the value of  $C$  is critical for correct trap modeling. The calibration of this parameter is detailed in Yanliang Guo's PhD thesis [76] and this section intends to provide a short description of this procedure.

The first step is to determine the vertical equilibrium position of the cloud that takes into

account gravity:

$$R = \frac{\omega_{\text{rf}}}{2\alpha} \left( 1 + \frac{\epsilon}{\sqrt{1 - \epsilon^2}} \frac{\Omega_0}{\omega_{\text{rf}}} \right) \quad (3.12)$$

Where  $\epsilon = Mg/(2\hbar\alpha)$  and  $\alpha$  is the magnetic field gradient in the horizontal plane at the equator of the ellipsoid. A way to evaluate the radius in the vertical direction is to look at the vertical position of a cloud after a time of flight of 23 ms.

The first step is to determine the magnetic field gradient  $\alpha$  for a given value of  $I$ , the current flowing through the science cell's quadrupole coil. As Eq.(3.12) shows, the initial position of the cloud depends on the RF frequency, and evaluating the vertical position of the cloud gives information on the initial vertical position of the cloud as the time flight duration is always the same. The cloud vertical position is determined by doing a fit and taking the vertical position. To evaluate the vertical equilibrium position of the cloud, a vertical oscillation measurement of the position of the cloud is performed. As the cloud oscillates around the bottom of the trap, this may disrupt the results of the gradient calibration. Once the oscillation measurement is done, a sinusoidal fit is applied to the different positions to determine the vertical position around which the cloud oscillates. By scanning the equilibrium position of the cloud with respect to the rf-frequency, one can obtain the curve displayed in Fig.3.6b. By doing a linear fit on this curve, the value of  $\alpha$  is obtained by looking at the linear coefficient.

Then the same measurement is done for multiple values of quadrupole current. The higher current value was the most important for us, therefore we decided to evaluate the  $\alpha$  values for 52 A, 56 A and 60 A on top of the initial value of the current 28 A when the cloud is loaded onto the bubble at the beginning of the gravity compensation ramp. The Fig.3.6a shows the evolution of  $\alpha$  with respect to the quadrupole current, and by doing a linear fit, one can deduce the value of  $C$ . The numerical value obtained is  $C = 2.090(23) \text{ G} \cdot \text{cm}^{-1} \cdot \text{A}^{-1}$ .

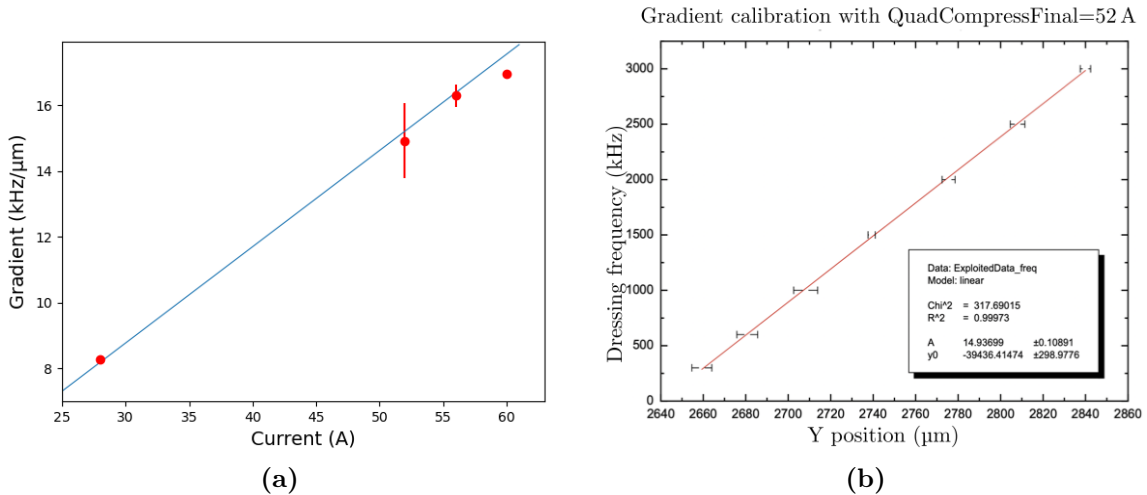


**Figure 3.6** — Fig.3.6a: Evolution of the magnetic field gradient with respect to the current in the quadrupole coils. The red dots represent the measurements done. The blue line represents the linear fit done. Fig.5.2b: Evolution of the dressing frequency with respect to the vertical position of the center of the cloud. The value of the vertical position of the center of the cloud is taken from a fit done after an oscillation measurement.



### 3.3 Results exploitation

Once all the tuning is done, we are able to take measurements. The result for a value of magnetic gradient of  $\alpha/2\pi = 7.54 \text{ kHz} \cdot \mu\text{m}^{-1}$  is shown in the following figure.

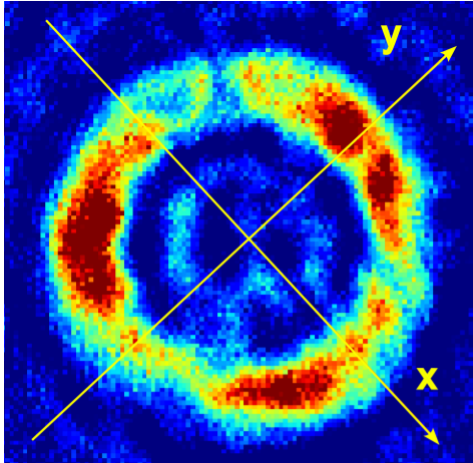


**Figure 3.7** — Ring of atoms when the RF is correctly tuned.

#### 3.3.1 Improved numerical model

A question up in the air at the end of Yanliang Guo's work was the apparent disagreement between the model explained in Sec.3.1.2 and the observation done experimentally. There was a disagreement on the estimation of the quadrupole magnetic gradient needed to compensate for gravity. To describe the potential more precisely, one has to look at the ratio taken into account to apply the rotating wave approximation in Chap.1:  $\frac{\Omega_0}{\omega_{\text{rf}}}$ . The ratio value is 0.28 in the case of the experiment conducted, which does not satisfy the condition  $\frac{\Omega_0}{\omega_{\text{rf}}} \ll 1$  suggesting the rotating wave approximation does not describe well the experimental situation. The inclusion of the non-resonant term is needed.

This numerical work had been done by Romain Dubessy to have a numerical evaluation of the potential detailed in [37]. The starting point is to use a Floquet expansion in order to include the non-resonant coupling terms in a 3D potential. It takes the  $\pm 2$  photons coupling into account in the calculation. This is how the potential referred to as  $V_{3D}^{Fl}(r, \theta)$  in Fig.3.8 is determined in spherical coordinates. This potential takes into account the resonant coupling responsible for the dressing of the atoms, the gravity, and the non-resonant coupling, which had been simplified in Sec.1.1.1. There is no mention of a  $\phi$  dependence because our system is assumed to be rotationally invariant. A numerical resolution of the Gross-Pitaevskii equation provides a solution of the ground state of our system.

However, one can see in Fig.3.8 that  $V_{3D}^{Fl}(r, \theta)$  lacks the positive divergence near the top of the bubble, preventing them from reaching the zero-coupling region. To include the transverse confinement in the potential, a similar approach to what has been developed in Sec.3.1.2 is taken. First, for each value of  $\theta$  a value of  $r$  is found that minimizes  $V_{3D}^{Fl}(r, \theta)$  and by this means one can have a 2D surface that minimizes our 3D potential. Then, for each point on the surface, the Hessian matrix of the potential is numerically computed. The eigenvalues are then computed, and the largest gives the transverse trapping frequency. Ultimately, this

procedure leads to the expression of a 2D potential:

$$V_{2D}^{Fl}(\theta) = V_{3D}^{Fl}(r_{min}(\theta), \theta) + \frac{\hbar\omega_{\perp}(\theta)}{2} \quad (3.13)$$

Where each of the term is evaluated numerically.

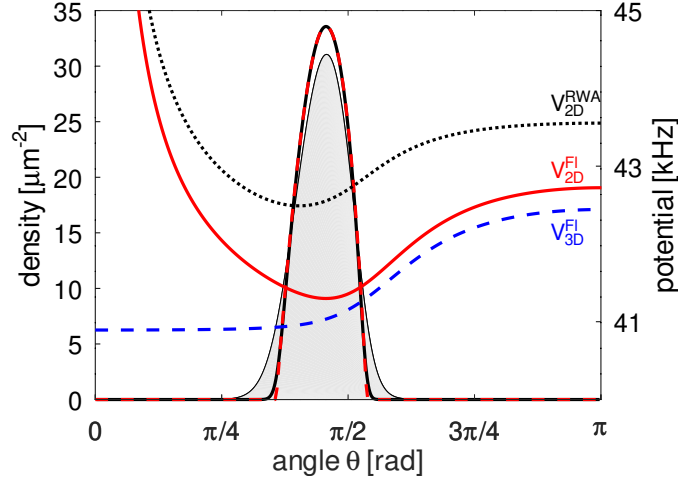


**Figure 3.8** – (color online) Right axis: effective potential on the surface  $V_{2D}^{Fl}(\theta)$  (solid red line),  $V_{3D}^{Fl}(rs(\theta), \theta)$  (dashed blue) and  $V_{2D}^{RWA}(z)$  (dotted black). Left axis: surface density 2D computed with the full 3D model (grey shaded area), the 2D semi-classical model (black solid line) and 2D Thomas- Fermi solution (dashed red line). The trap parameters are:  $\omega/2\pi = 300$  kHz ,  $\Omega_0/2\pi = 85.0(5)$  kHz and  $\alpha/2\pi = 7.68(9)$  kHz  $\cdot \mu\text{m}^{-1}$ .

### 3.3.2 Comparison with analysis

Now that we have a numerical model to describe the experiment, let us compare it with the data. The Fig.3.8 displays the different model used to describe the experiment:  $V_{3D}^{Fl}(r, \theta)$  with a dashed blue line,  $V_{2D}^{Fl}(r, \theta)$  with a black dotted line, and  $V_{2D}^{RWA}(\theta)$  with a plain red line whose expression is given in Eq.(3.7). The first conclusion one can draw from this graph is that the numerical model encompassing the non-resonant coupling terms in 3D fails to accurately describe the experiment: there is no minimum where the atoms would accumulate. Then the 2 different models that take into account the transverse confinement have qualitatively the same behavior: there is a minimum near the bubble's equator. The model that displays the most similarity with the experimental result is the  $V_{2D}^{Fl}(\theta)$  with a minimum close to the experimental threshold observed experimentally. This threshold corresponds to the appearance of the local minimum of density in the center of the cloud of atoms.

As presented in Fig.3.9, one can see the evolution from a connected cloud at the bottom of the trap to a ring in levitation inside the trap. The top row shows the experimental data, the middle row displays a top view of the simulation of the 3D Gross-Pitaevskii equation done by Romain Dubessy and the bottom row shows a side view of that same simulation. Each column corresponds to a gradient value ranging from the lowest value on the left to the highest value on the right. The pink line is a visual representation of the value where the gravity compensation happens in the numerical 2D model. This value is lower than the

naive value  $\alpha_g$  in the chapter, which is  $7.54 \text{ kHz} \cdot \mu\text{m}^{-1}$ , a position at which the ring is already well-formed.

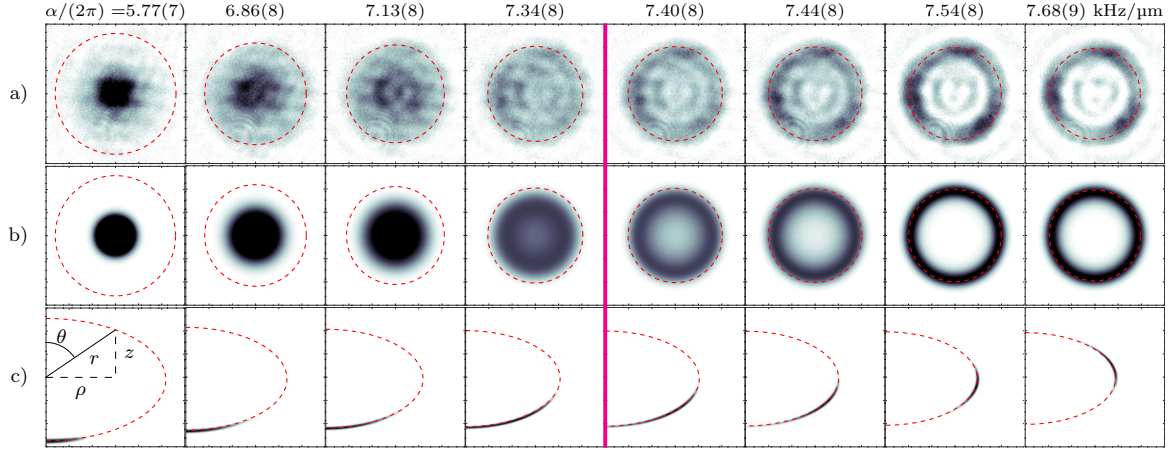


**Figure 3.9** – Scan of the gradient for a maximum Rabi coupling  $\Omega_0/2\pi = 85 \text{ kHz}$ . Each column represents the situation for a given gradient from lowest (left) to highest (right) value. The line (a) represents the experimental photo taken. The line (b) represents a top view of the simulation. The line (c) represents a side view of the simulation. The pictures in line (a) and (b) have a size of  $120 \mu\text{m} \times 120 \mu\text{m}$ . The pictures in line (c) have a size of  $60 \mu\text{m} \times 60 \mu\text{m}$ . The pink line represents the value at which the gravity is compensated. This figure is taken from Ref. [37]

Furthermore, the lifetime in the trap decreases when gravity is overcompensated. The number of atoms with respect to time always follows a double exponential decay with a short decay time of the order of 1 s and a longer decay time of the order of 10 s. As shown in Fig.3.10a, the increase in gradient above a certain threshold leads to a reduction of both lifetimes measured in the trap. Even if the loss mechanism is not fully understood [92], a calculation has ruled out the possibility of 3-body losses. The three-body losses represent the three-body recombination, a mechanism involving the formation of a molecule with two atoms and the excess of energy being transferred to the kinetic energy of a third atom. The expression of the loss of atoms due to this phenomenon is given by:

$$\frac{\partial N(t)}{\partial t} = -K_3 \int n^3(\mathbf{r}, t) d\mathbf{r} \quad (3.14)$$

$$n(\mathbf{r}, t) = |\Psi(\mathbf{r}, t)|^2 \quad (3.15)$$

In the equation (3.15),  $\Psi$  is the wavefunction of the BEC in the trap, which is determined self-consistently. The calculation was done for a ring of atoms at the equator in the bubble. In such a case, two cases were studied: the case where the BEC is strongly confined in the radial direction, and the case where the BEC is in 3D along the ring. For the 3D case, the density profile was given by a Thomas-Fermi profile in 3D:

$$n_{3D}(r, z) = \frac{\mu_{3D}}{g} \left( 1 - \frac{(r - r_0)^2}{R^2} - \frac{z^2}{R_z^2} \right) \quad (3.16)$$

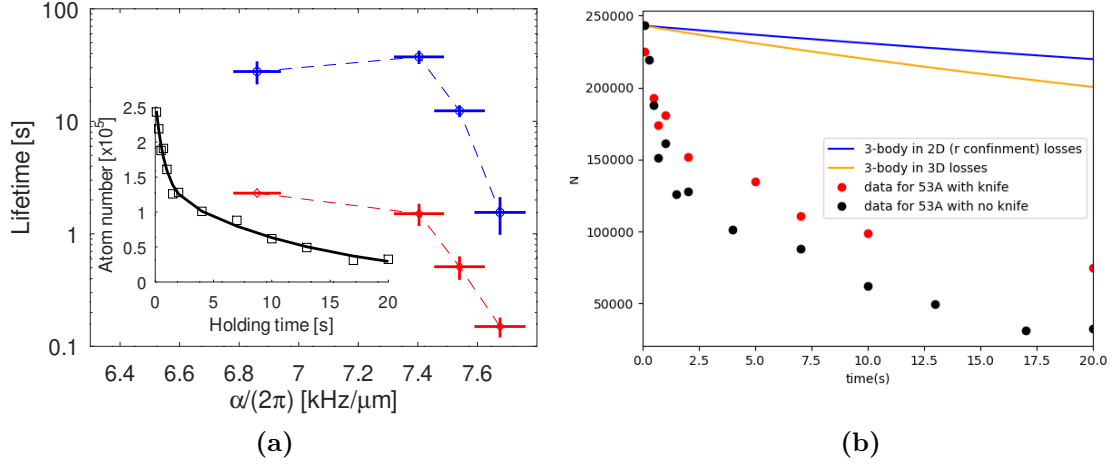


**Figure 3.10** – Fig.a: lifetime evolution with respect to the gradient with two time constants. The blue curve represents the long lifetime and the red curve represents the short lifetime. Inset: Lifetime measurement after a time of flight for a gradient of  $\alpha/2\pi = 7.54 \text{ kHz} \cdot \mu\text{m}^{-1}$ . The square represents the measured number of atoms and the black line represents the double exponential decay model. Fig.b: evolution of the number of atoms when  $\alpha/2\pi = 7.68 \text{ kHz} \cdot \mu\text{m}^{-1}$ . The red and black series of points are experimental measurements of the number of atoms. The red dots represent a serie of measurements with a rf-knife applied during the dressing and the waiting time. The black dots represent a serie of measurements without such rf-knife. There is no qualitative difference these two series of measurements. The blue and orange represents 2 different models of 3-body losses.

Where  $R_z = \sqrt{2\mu/(M\omega_z^2)}$ ,  $R = \sqrt{2\mu/(M\omega_r^2)}$  are the two Thomas-Fermi profiles. The chemical potential in 3D is given by  $\mu_{3D} = \hbar\sqrt{\omega_r\omega_z}\sqrt{2Na_s/(\pi r_0)}$  [57]. By using these expressions and doing the integration, this gives:

$$N = \frac{N_0}{1 + \gamma_{3D}N_0t} \quad \gamma_{3D} = \frac{K_3}{16\pi^3 a_s r_0 a_r^2 a_z^2} \quad (3.17)$$

For the 2D-case, we have made the approximation that the gas was strongly confined along the radius. The density profile was:

$$n_{2D}(r, z) = \frac{\mu}{g_{2D}} \left(1 - \frac{z^2}{R_z^2}\right) \frac{e^{-\frac{(r-r_0)^2}{a_r^2}}}{\sqrt{\pi}a_r} \quad (3.18)$$

In this regime, the interaction strength is modified by  $g_{2D} = g/(\sqrt{2\pi}a_r)$ , and so is the chemical potential  $\mu_{2D} = \hbar(\omega_r\omega_z^2)^{1/3}((3Na_s/r_0)^2/(2(2\pi)))^{1/3}$ . By integration of Eq.(3.15), the three-body losses in two dimensions are given by:

$$N(t) = \frac{1}{(1 + \gamma_{2D}N_0^{4/3}t)^{3/4}} \quad \gamma_{2D} = K_3 \frac{3^{5/6}(a_s r_0^2 a_r^2 a_z^4)^{-2/3}}{35 \times 2^{2/3} \pi^{8/3}} \quad (3.19)$$

The curves representing the 3-body losses in Fig.3.10b are in blue for the 3D regime and in orange for the 2D case with a transverse confinement along the radius. Both are extremely

different from the experimental data, enabling us to rule out three-body recombination as the main loss mechanism when gravity is compensated in the trap.

### 3.3.3 Slightly inhomogeneous ring

As observed in Fig.3.7, there is still an inhomogeneity in the ring. The reader can distinguish three different maxima along the circle's perimeter. An explanation for this inhomogeneity is the finite size of the dressing antennas used to dress the atoms.

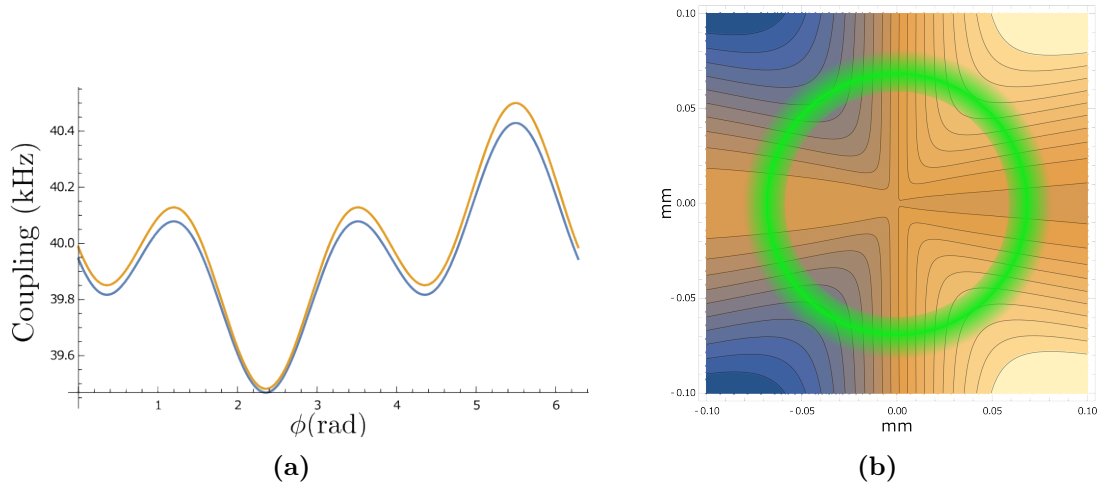


**Figure 3.11** — Fig.a display a graphical representation of the amplitude variation due to the finite size around the circle of atom. The blue curve represents the square coil, the orange curve represents the circle coil. Fig.b display a contour plot of amplitude variation of the finite size of the coils.

A way to explain this inhomogeneity is to look at the order of magnitude of the different elements of the experiment. On one side, the bubble size is about  $100\ \mu\text{m}$  wide, and the size of the dressing antennas is  $1\ \text{cm}$ . By comparing these 2 sizes, one can obtain an estimation of the effect of the inhomogeneity of the field. As the bubble is a hundredth of the size of the coil, this is typically the size of the field inhomogeneity to expect. On the other side, the dressing frequency is of the order  $100\ \text{kHz}$  and the field inhomogeneity would mean a variation in frequency of around  $1\ \text{kHz}$ . This value has to be compared to the chemical potential of the ring, which is around  $1\ \text{kHz}$ . So we have a field inhomogeneity with a value comparable to the chemical potential. This can explain the presence of maxima and minima in the atom density along the circle. A more detailed calculation has been done by H el ene Perrin, which leads to the graphs in Fig.3.11. There are two curves on the graph presented: the blue curve represents the inhomogeneity computed for a square coil, and the orange curve is the inhomogeneity computed for a circular coil. This has to do with the geometry of our dressing coils, they are square-shaped with round edges. One can see they are alike: they display the same number of minima and maxima at the same position, and the only difference is the height of the maxima. There are three different minima, which is in agreement with the observation of the ring having three maxima of density. Also, one can see a difference in the spreading of atoms along the ring. It implies the phase difference is not exactly  $\frac{\pi}{2}$  after

having done the rf-tuning session as the criteria was having the most uniform spread of atom along the circle. Fig.3.11b shows the potential inhomogeneity in the plane. The orange parts show the minima, whereas the blue parts show the maxima. There are three "valleys", which correspond to the minima observed on the function graph.

### 3.4 Conclusion

To conclude this chapter, the result of compensating gravity inside a quadrupole-dressed trap is the spontaneous formation of a ring. When gravity is strictly compensated, this ring is long-lived, and its lifetime decreases when the gradient overcompensates gravity. To fully depict this system, a numerical model has been developed by Romain Dubessy in order to take into account the out-of-resonance terms. This brings a new method to produce a ring-shaped Bose-Einstein condensate. This work is published in the New Journal of Physics [37].



## Part II

# New control system and its applications





# Chapter 4

## The control system: Implementation of the Labscript-Suite

The Chap.2 detailed how to obtain a Bose-Einstein condensate through an experimental sequence. In order to observe a BEC, multiple devices have to be coordinated to do various tasks, such as compressing the magneto-optical trap or sending a radio-frequency field to evaporate the atoms with the highest kinetic energy. For a laboratory setup to produce a BEC, there are multiple requirements, such as being able to communicate with the devices, having a time precision of one microsecond (the shortest pulses in the experimental sequence are the imaging pulses, which last for 17  $\mu\text{s}$ ), and to store the data.

Prior to this system change, the group was using Manip, a homemade software coded in C++ written to interact only with hardware pieces. To start an experimental sequence, a file was edited to choose which steps to run. This file was then compiled, and the instructions it held were run. At the main sequence's end, a picture was taken and displayed on a separate computer from the one executing the sequence. If further analysis were required, the data were sent to a piece of software programmed in Matlab. The setup was functional, yet some shortcomings were observed:

- The system was working on software no longer maintained: Manip was installed on a PC working with Windows XP. If a problem happened, there was a risk of not being able to reinstall the control system on a newer computer.
- Insufficient time precision: the clock had a frequency of 10 kHz leading to a time accuracy of 100  $\mu\text{s}$ , insufficient for the sequence. For example, to circumvent this limitation, a pulse generator was used for the imaging pulses, achieving the time precision required.
- Partial archiving of the results: the former control system did not fully manage the radiofrequency sources. The RF parameters were edited on a dedicated piece of software, and the data were stored in files accessible by Manip. These files were sent to the devices, and their execution was triggered by TTL pulses. The result was that no data were kept except the one written in the lab textbook by the experimentalist.

The team decided to change the control system to the Labscript Suite prior to the beginning of my PhD. This choice was made after a careful comparison of the different options

readily available. The other options were the Cicero word generator [93], an open source control system developed by the MIT cold atom group, or ARTIQ [94], a system developed by M-Lab in collaboration with the ion-storage group at the NIST. The Labscript Suite is an open-source software developed by the quantum fluids group at Monash University in Melbourne. This control system enables the user to edit a sequence file written in Python with a dedicated library and change the values of these parameters using a graphical interface. This graphical user interface was decisive in choosing the Labscript Suite. This chapter introduces the Labscript Suite with a presentation of each of its components. Then the main devices incorporated in the new system are presented, some major hardware updates had been done jointly with the software changes. After, the transcription of the experimental sequence is detailed, along with the adaptation of the data analysis system to the Labscript Suite. Ultimately, some proposals on how the setup can be improved are given.

## 4.1 The new control system: Labscript-Suite

### 4.1.1 General architecture

The Labscript Suite is an open source control system developed by the Monash University cold atoms group [38, 95, 96]. The cornerstone of this system is Labscript, a library they developed in Python that translates high-level instructions given by the experimentalist into low-level instructions understandable by the different devices. In the context of computer science, a library is a set of functions and objects usable by a programmer. `IQuadBEC.constant(t=tBEC,value=28,units='A')` is an example of such an instruction written by the experimentalist in Labscript language, where the output IQuadBEC is set to 28 Ampere at the timecode tBEC. The units here allow the user to change the output expression. The default unit is voltage, but it is often more convenient to express the command in a different unit. As for the example given above, which drives a current supply, it is more useful to express the output in amperes. This change of unit is taken into account via a transfer function coded by the user and assigned to the analog output; this will be detailed in Sec.4.2.2.

One of Labscript's purposes is to write down an experimental sequence in a Python file, and the sequence writing will be detailed in Sec.4.3.1. It also allows the user to get an interface with the different devices in the lab; this work will be detailed in the Sec.4.2. In this same section, a description of the connection table, a key dependency of our system will be given.

Each experimental realization is stored in a HDF5 file called a shot file. This format is the acronym for Hierarchical Data Format, which stores different types of information in a tree structure. The most complex data, such as an image at the end of an experimental sequence, is stored as a dataset, whereas simpler data, such as the value of a parameter, is stored as an attribute. This file is used as a unique vector of information inside the control system, and each experimental realization is stored in a separate file.

This is shown in Fig.4.1 as the red arrows in the scheme, which show the path of a shot file. The shot file will now be referred to either as the shot file or the HDF file. We can see that the control system is composed of four independent pieces of software: Runmanager, BLACS, Runviewer, and Lyse. This section will follow the path of a shot-file through the system, following the red arrow from top to bottom. This will start with Runmanager and the shotfile generation, then BLACS will be introduced and how a shotfile is run, followed by the data analysis system through Lyse, and ultimately Runviewer will be presented. Each of these pieces of software has a graphical user interface (GUI) developed using PyQt, the

Python version of the application programming interface Qt. Also, the pieces of software and their different processes communicate using the ZeroMQ library.

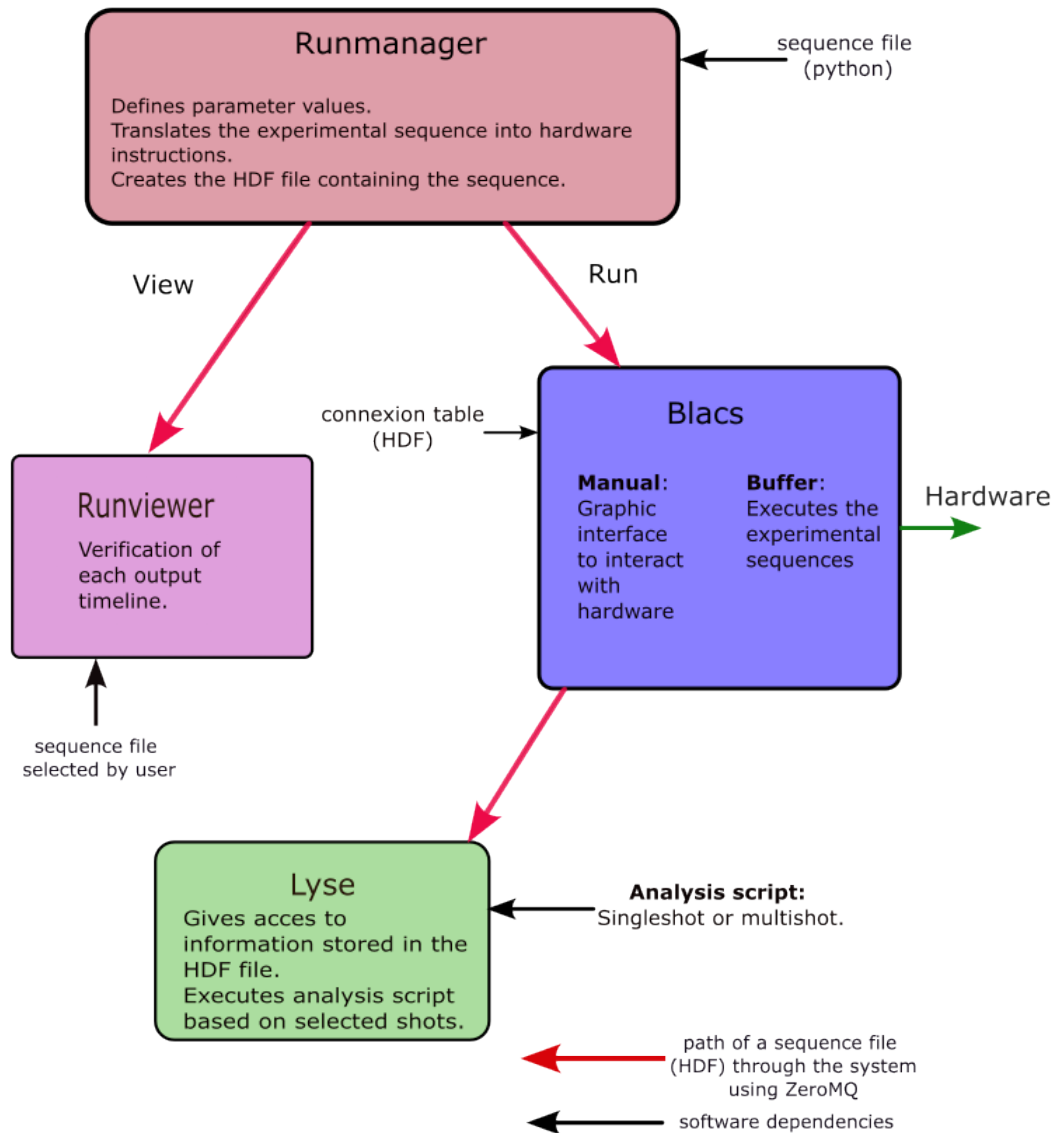


**Figure 4.1** – A scheme of the interaction of the different components of the Labscript Suite. The red arrows show the usual path a HDF shot-file of a sequence takes during a sequence execution. A black arrow pointing toward a box indicates a dependency on the software it points to.

#### 4.1.2 Runmanager

The first piece of software in the system is Runmanager. The experimentalist writes a sequence in a Python file using Labscript to describe the desired sequence. This file cannot be used directly by the system, and the first step is to generate an HDF file associated with the python

file. This is the role of Runmanager: to compile the sequence file. It takes the Python file and the numerical value of each parameter stored in Runmanager to generate the HDF shot file.

The other role of Runmanager is to change the parameters' values easily in the sequence. As presented in Fig.4.2, the different values are available through the graphical user interface of Runmanager and can be easily modified. These values can be organized through groups of parameters, which are accessible through the column on the left of the GUI. The top group in this column gives access to a Python console that displays error codes when an error occurs, either in the compilation process or when a programming error has been made in the sequence file. For each variable, there is a name, the numerical value associated, a unit, which is given only as a visual indication, and an expansion status. This last item refers to the option of scanning the numerical value of a parameter. It is often useful to execute a series of experimental sequences that differ only by the numerical value of one parameter. A series of numerical values can be given as a python tuple, an array of values, and when asked to compile, Runmanager will generate one shot file per value in the tuple. Multiple parameters can be scanned together, the organization of the parallel scan is determined in the Axes group and modifies the expansion item. The numerical value's order can be randomized when the 'shuffle' option is chosen. All the parameters and their values are stored in an HDF file, and multiple HDF files containing parameters can be opened in parallel.

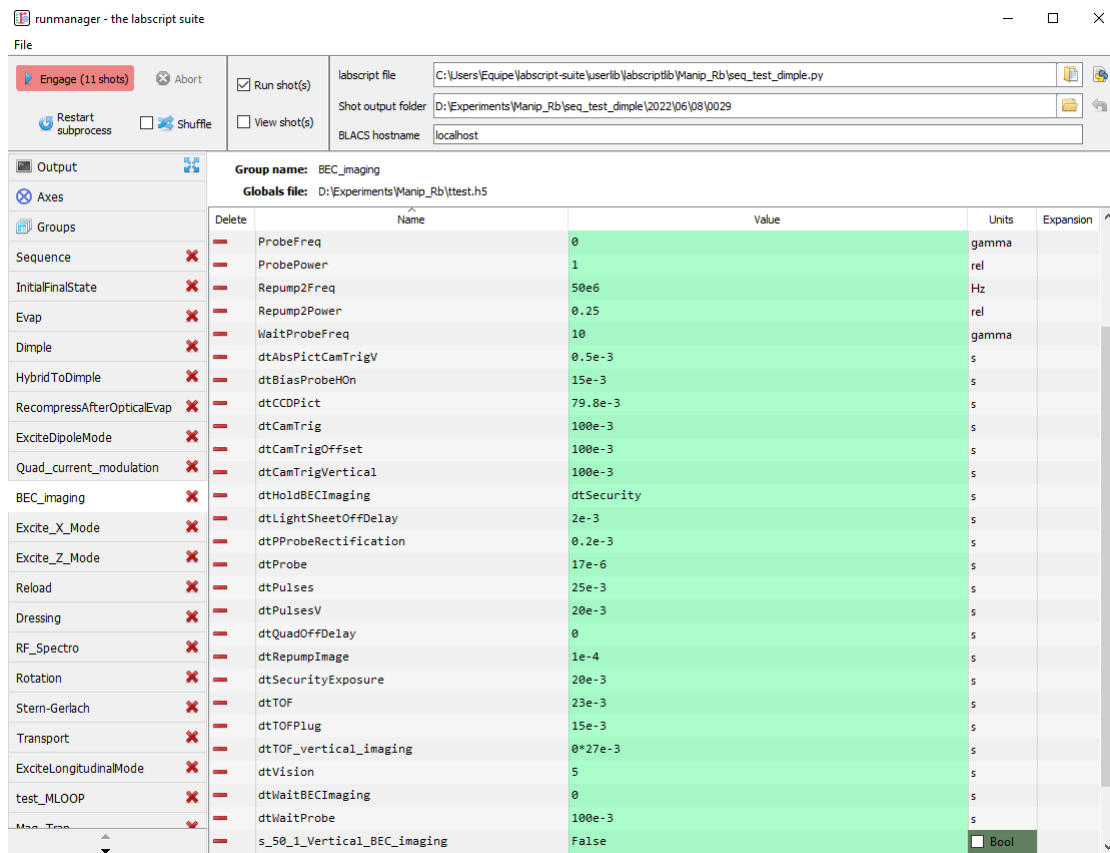


Figure 4.2 — Graphic user interface of Runmanager.

There are multiple options in Runmanager about the compilation, such as whether to run the sequence directly; in that case, the file is sent to BLACS; or to view the file; the file is then sent to Runviewer, a signal visualizer. These paths are shown in Fig.4.1.

### 4.1.3 BLACS

BLACS is the acronym for "Better Lab Apparatus Control System". This is the piece of software responsible for interacting with the different devices. As such, it interacts with the different device drivers, the software interface between the computers, and the devices themselves. Each order given to a device is executed internally by BLACS in a subprocess dedicated to this device. When a problem occurs in the subprocess, it does not prevent BLACS from operating, and the problem is signaled to the user. The interaction between the devices and the system is done by editing the connection table and will be detailed in Sec.4.2. BLACS has two different modes:

- In manual mode, the user can interact directly with devices.
- In buffer mode, the sequence is executed. When this mode is on, the user can no longer interact with the devices, and all actions are prevented by the system in order not to disturb the execution of the sequence.

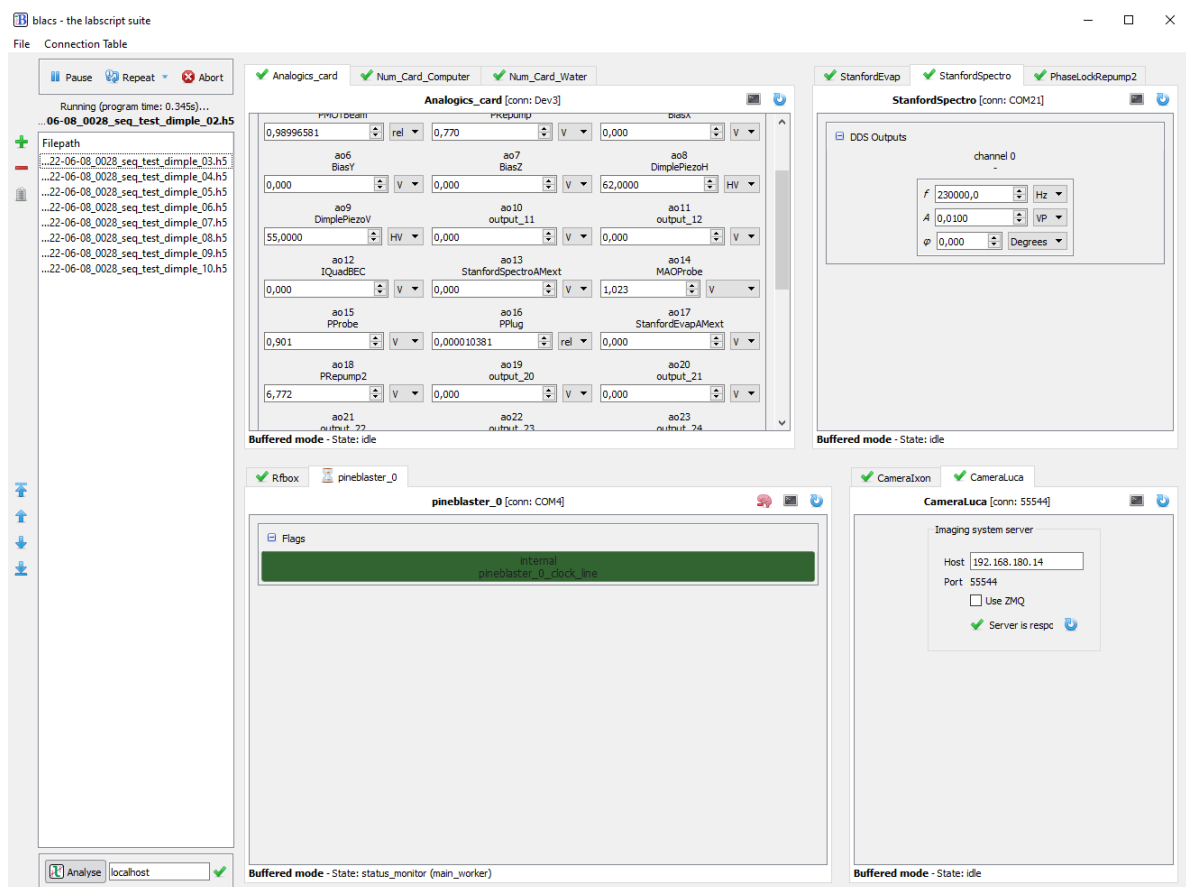


Figure 4.3 — Graphic user interface of BLACS during a sequence with multiple shots.

Once a shotfile has been compiled by Runmanager, BLACS is given a reference to the file as shown in Fig.4.1 by the top "run" red arrow. This reference is stored in the queue, waiting to be executed. The graphical depiction of the queue can be seen in Fig.4.3 on the left part of the graphical user interface. This queue can be managed by the user through the buttons around the left column; as such, it can be paused, and the execution of the HDF file can be repeated or aborted if needed using the top buttons. The buttons on the side of the queue allow the user to empty the queue, reorder it, and add or suppress a specific element. When a sequence is executed, BLACS enters buffer mode and leaves it at the end of the shot execution. After a sequence has been executed, its reference is passed to Lyse for further analysis.

When no sequence are executed, BLACS is in manual mode. In this case, the experimentalist may interact with the different devices using the graphical user interface of BLACS. For instance, in Fig.4.3, in the right panel, each analog output can be changed manually.

#### 4.1.4 Lyse

After the execution of a sequence is finished, the shot file reference is sent to Lyse for the data to be analyzed. Lyse is short for "analysis". It is the part of the piece of software dedicated to data analysis, which is done through analysis scripts coded by the experimentalist. The main analysis script written for the Rubidium experiment at the LPL will be detailed in Sec.4.3.2. The main graphical user interface of Lyse is shown in Fig.4.4 is split into three parts:

- On the top left: interaction with the analysis scripts. The analysis scripts are loaded into the graphical user interface in order to be executed. There are two kinds of analysis scripts: the single-shot routine, which analyzes the data contained in only one script, and the multishot script, which analyzes the data over multiple files. For instance, an analysis script determining the number of atoms on a picture is written as a single-shot analysis script, whereas a script analyzing the oscillation of the cloud from several pictures would be a multi-shot analysis script. The script can be unselected in order not to be applied to the incoming shot files. To write the analysis file, there are certain restrictions on using standard libraries. It is strongly suggested to use numpy [97], scipy [98], and matplotlib [99] in order to perform certain calculations, whereas some libraries are impossible to use without encountering problems (PyQt, for example). The most used analysis script present in Fig.4.4 is AbsorptionImagingAnalysis. Its role will be detailed in Sec.4.3.2 and one of its functions is to copy the image onto the shotfile. As such, it is executed on each incoming file.
- On the bottom left: representation of the numerical value of the parameters in the sequence. The different parameters are written in the shot-file, as described in Sec.4.1.2. When working on the laboratory setup, it is often useful for the experimentalist to check the value of certain parameters. This is possible using this part of Lyse's GUI, which displays a spreadsheet called a dataframe. On top of each column, the name of each parameter is displayed, and the value for each file is loaded. Also, analysis script results can be saved in the shot file and shown in the same dataframe. As there are numerous parameters in a sequence, the experimentalist can choose which parameter to display. It is vital not to display the uninteresting parameters for the user; otherwise, the dataframe becomes confusing and useless. An example of this selection can be viewed in Fig.4.4. The experimentalist was tuning the dimple beam position, and as such, only the parameters related to this part of the experiment are displayed.

The screenshot displays the Labscript-Suite interface. On the left, there are two panels for 'Fullshot routines' and 'Shots'. The 'Shots' panel shows a table with columns for 'name', 'Piezo\_V', 'UDimple', 'UDimple', 'Piezo\_H', 'UDimple', 'UDimple', 'dOpticalExporati', 'dRampExpFin', 'evapFinStop', and 'fit results'. The table contains 28 rows of shot data, with the first row highlighted in blue. The 'fit results' column contains a list of analysis routines and their corresponding parameters.

The main area of the interface shows a detailed view of the selected shot's analysis results. It includes a list of routines and their parameters, such as 'Gaussian Fit done', 'Type of fit : Anisotropic 2D Gaussian', and 'Camera calibration parameters saved on the .h5 file'. The results are displayed in a text-based format, showing the output of various analysis scripts.

name	Piezo_V	UDimple	UDimple	Piezo_H	UDimple	UDimple	dOpticalExporati	dRampExpFin	evapFinStop	fit results
28_2022-06-09_0065_seq_test_dimple_11	68	1	100.0m	62	1	100.0m	12	10	400.0k	[1.43900188e+...
29_2022-06-09_0066_seq_test_dimple_12	68	1	100.0m	62	1	100.0m	12	10	400.0k	[187.4559538 ...
30_2022-06-09_0067_seq_test_dimple_0	68	1	100.0m	62	1	100.0m	12	10	400.0k	[1.26396202e+...
31_2022-06-09_0067_seq_test_dimple_1	68	1	100.0m	62	1	100.0m	12	10	400.0k	[1.82218133e+...
32_2022-06-09_0067_seq_test_dimple_2	68	1	100.0m	62	1	100.0m	12	10	400.0k	[1.58986976e+...
33_2022-06-09_0067_seq_test_dimple_3	68	1	100.0m	62	1	100.0m	12	10	400.0k	[1.30943267e+...
34_2022-06-09_0067_seq_test_dimple_4	68	1	100.0m	62	1	100.0m	12	10	400.0k	[95.34761227 ...
35_2022-06-09_0067_seq_test_dimple_5	68	1	100.0m	62	1	100.0m	12	10	400.0k	[9.92468038e+...
36_2022-06-09_0067_seq_test_dimple_6	68	1	100.0m	62	1	100.0m	12	10	400.0k	[132.9105122 ...
37_2022-06-09_0067_seq_test_dimple_7	68	1	100.0m	62	1	100.0m	12	10	400.0k	[99.27042995 ...
38_2022-06-09_0067_seq_test_dimple_8	68	1	100.0m	62	1	100.0m	12	10	400.0k	[131.7274207 ...
39_2022-06-09_0067_seq_test_dimple_9	68	1	100.0m	62	1	100.0m	12	10	400.0k	[131.67937580...
40_2022-06-10_0063_seq_test_dimple_0	68	1	100.0m	62	1	100.0m	12	10	400.0k	[201.37319929...
41_2022-06-10_0064_seq_test_dimple_00	68	1	100.0m	62	1	100.0m	12	10	400.0k	[139.05018182...
42_2022-06-10_0064_seq_test_dimple_01	68	1	100.0m	62	1	100.0m	12	10	400.0k	[127.52043406...
43_2022-06-10_0064_seq_test_dimple_02	68	1	100.0m	62	1	100.0m	12	10	400.0k	[108.20812424...
44_2022-06-10_0064_seq_test_dimple_03	68	1	100.0m	62	1	100.0m	12	10	400.0k	[129.18328640...
45_2022-06-10_0064_seq_test_dimple_04	68	1	100.0m	62	1	100.0m	12	10	400.0k	[135.12182801...

Figure 4.4 — Graphic user interface of Lyse. The three distinct part are represented: the top left with the scripts choice, the bottom left with the dataframe representation, and the python console on the right.



- On the right: a Python console gives information when the script is executed. This is where the information related to the execution of a script is displayed. When a script cannot be executed because of an error, this is where the error message will print. The experimentalist can also use this part to display the result of an analysis, for instance. As seen in Fig.4.4, the results of the fit are displayed in this console. The reader can see the different physical parameters, such as the spatial extension of the model or the number of atoms detected. The details about the fitting procedure are mentioned in Sec.4.3.2.

### 4.1.5 Runviewer

Runviewer is an optional yet helpful piece of software to visualize the signal delivered to each output. Fig.4.5 shows the window of Runviewer. The top left of the window is dedicated to the file loading, and each file has an assigned color. The checkbox on the left allows the user to choose whether or not to display the data from the file. On the bottom left, the user chooses which signal to display, and the right side of the window displays the different graphs. All these graphs show the evolution of the voltage with respect to time. All the different outputs that can be displayed, whether numerical or analog, are referred to as "channels". For each channel, the graph shows a line of color for each file. As seen in Fig.4.5 for the `pineblaster_0_clock_line` graph, the black line displays the signal of the first file, and the red line is associated with the second file.

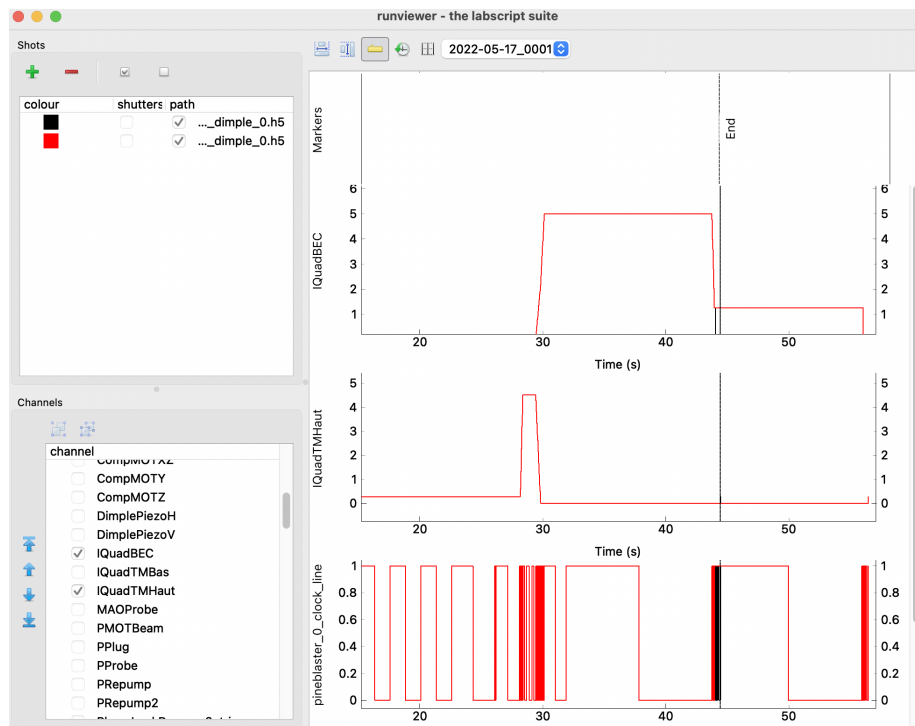


Figure 4.5 – Runviewer's window.

## 4.2 Hardware control

One interesting feature of Labscript Suite is its wide support for different devices. When a specific one is not directly available, there is a clear path to interface with it, as detailed in the online documentation. This opportunity enables the incorporation of many devices specific to the experimental setup; some examples will be detailed in this section.

```

1 from labscript import *
2 from labscript_devices.PineBlaster import PineBlaster
3 from labscript_devices.NI_DAQmx.labscript_devices import NI_PXIe_6738
4 from labscript_devices.NI_DAQmx.labscript_devices import NI_PXIe_6535
5 from labscript_utils.unitconversions import *
6 from Functions_Transferts import *
7
8 ### Our Own Modules / Devices ###
9 from user_devices.CameraRb import CameraRb
10 from user_devices.DDS_Stanford_Static import DDS_Stanford_Static
11 from user_devices.DDS_BBB_RFbox import DDS_BBB_RFbox
12
13 ### Connection table
14 ### Clock
15 PineBlaster(name='pineblaster_0' ,usbport='COM4')
16 ### Analogics
17 NI_PXIe_6738(name='Analogics_card',parent_device = pineblaster_0.clockline ,
18             clock_terminal='/Dev3/PFI0' , MAX_name='Dev3' ,
19             max_A0_sample_rate=400e3)
20 ### Numerics
21 NI_PXIe_6535(name='Num_Card_Computer' ,parent_device=pineblaster_0.clockline ,
22             clock_terminal='/Dev3/PFI0' , MAX_name='Dev2')
23 NI_PXIe_6535(name='Num_Card_Water' ,parent_device=pineblaster_0.clockline ,
24             clock_terminal='/Dev3/PFI0' , MAX_name='Dev1')
25
26 ### Declaration of the numerical outputs:
27 ### Rack facing computer:
28 Shutter( name='ClicClacPlug' ,parent_device=Num_Card_Computer ,
29         connection='port0/line0' , delay=(0,0) , open_state=0)
30 DigitalOut(name='SwitchIGBTs' ,parent_device=Num_Card_Computer ,
31           connection='port0/line3' , inverted=True)
32
33 ### Declaration of the analog outputs:
34 AnalogOut(name='IQuadTMHaut' ,parent_device=Analogics_card ,connection='ao0' ,
35          unit_conversion_class = TF_AlimMOT_TMHaut)
36 AnalogOut(name='IQuadTMBas' ,parent_device=Analogics_card ,connection='ao1' ,
37          unit_conversion_class = TF_AlimMOT_TMBas )
38
39 ### Declation of Camera
40 CameraRb( name='CameraLuca' , parent_device=Num_Card_Water ,
41          connection='port0/line4' , exposure_time=20e-3, BIAS_port = 55544)
42
43 ### Declaration of RF DDS
44 DDS_Stanford_Static(name='StanfordEvap' , parent_device=Num_Card_Computer ,
45                   connection='port2/line0' , com_port='COM20')
46 DDS_BBB_RFbox(name='Rfbox' , parent_device=Num_Card_Computer ,
47              connection='port3/line7' , ip = '192.168.180.50' , port=55566)

```

Listing 4.1 — Extract of the connection table

In order for the Labscript Suite to operate, the experimentalist needs to edit the connection table. This is a Python file listing all the different instruments and their properties that are

interfaced to work in the Labscript Suite system. The role of the connection table is to declare the names of each output that can be used by the system. Once the Python file is written, it is not directly usable by the Labscript Suite. The experimentalist needs to compile it using Runmanager to obtain the HDF version needed for BLACS and Runmanager to operate. An extract of the connection table is displayed in List.4.1; only a small portion of the devices and outputs have been kept for this illustrative example.

The following section presents the new pieces of hardware, starting with the clock, then the numeric and analog output systems, which have been changed, all the RF generators we use, and ultimately the camera workflow.

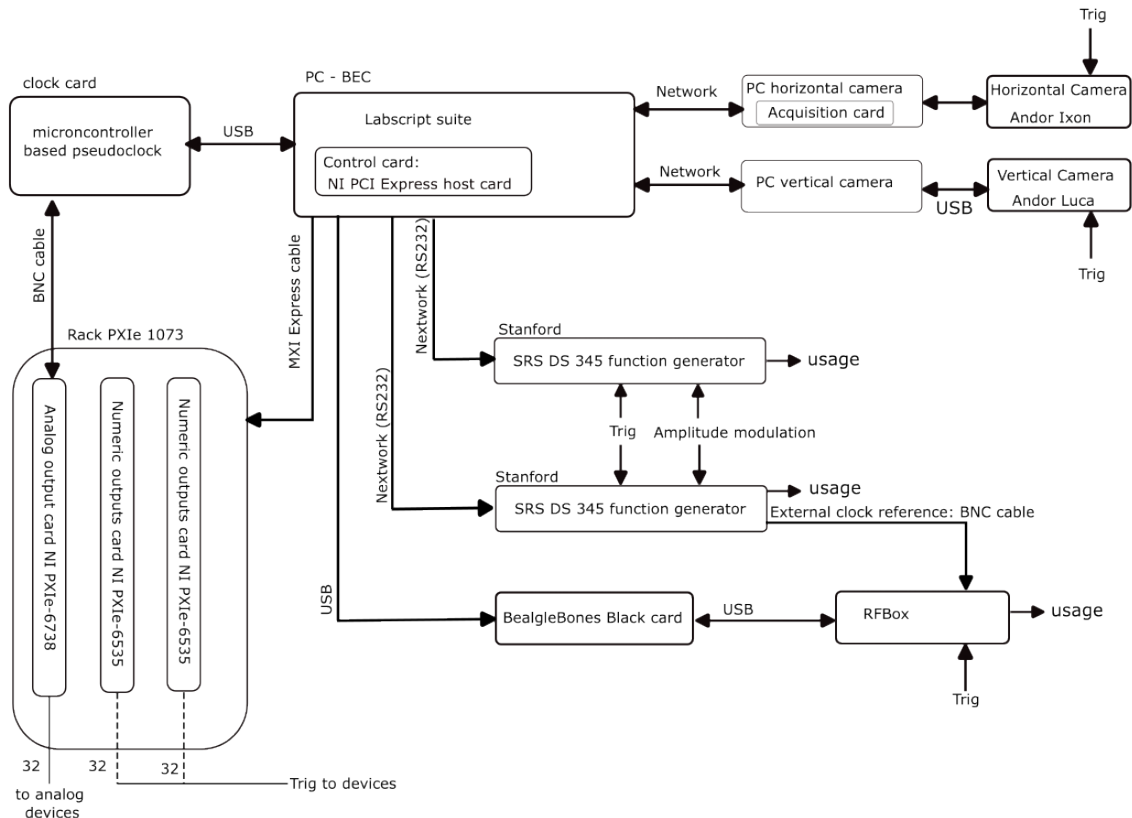


**Figure 4.6** – The interaction scheme of the different devices. Each arrow shows a link between devices, and the direction of the arrow shows the direction of the information flow.

#### 4.2.1 The clock

To achieve Bose-Einstein condensation, a sequence of actions run with accurate timing is needed, requiring coordination of the devices. A common time reference is shared in the form of a clock signal. The clock system has been adapted to the new system requirement:

- In the previous control system, there was a "true" clock generated by one of the output cards. This card was a National Instrument PCI-6713, and the clocking signal was

distributed across the different devices using a dedicated bus. The clock's refreshing rate was set at 10 kHz (time step of 100  $\mu$ s) for all analogical and numerical output. This situation leaves one question open: how to deal with processes needing time precision below 100  $\mu$ s? This was the case for the imaging pulses lasting for a few microseconds. To solve this problem, a pulse generator able to generate microsecond pulses was triggered through the clocked main system.

- In the Labscript Suite, for the system to work a pseudoclock is needed, and a device providing a non-uniform clocking signal is required. This means the signal does not change once per timestep; instead, it changes only when one of the outputs must change. For instance, to generate a 10 ms pulse, there will be a first clock signal at the beginning of the pulse and a second clock signal at the end of the pulse. Fig.4.5 shows a representation of this clock with the channel called `Pineblaster_0_clock_line`. One can see that there are times when no change is made and that at other times the signal changes a lot over a short period of time. This is typically what happens when a ramp is used during the sequence. The algorithm used for the pseudoclock to work is more complex than the case where a "true" clock is used, but it is also more flexible. An example of such flexibility is the ability for the user to adapt the sample rate for each ramp.

To implement the pseudoclock, we use the Texas Instrument EK-TM4C129EXL, a microcontroller card specially programmed to perform this task. The program for the pseudoclock is open source and available on GitHub, as noted in this reference [100].

For our clock to be functional, a calibration of the microcontroller was done by generating a ramp in Labscript Suite and measuring the time between the first change and the last change using an oscilloscope. After measuring this time interval, we compare it to the ramping time set by the user, and then the microcontroller code is changed to reach better accuracy. The main focus of this optimization was to minimize the jitter when executing a sequence. This method of looking at the time precision of the pseudoclock is very far from the usual experimental condition: having a ramp lasting for minutes is not realistic. This method gives an overestimation of the jitter, the cumulative error in the timing, which was 196 ms for a 5 min ramp with a sample rate of 10 kHz.

That is why an estimation of the jitter is needed with "true" experimental conditions. This measurement has been done in parallel with the day-to-day use of the experiment with the sequence defined in Sec.4.3.1. In parallel with the sequence, a numerical output is raised at the start of the sequence and lowered 17 s seconds later. As a comparison, the total sequence lasts for 45 s. Using an oscilloscope, we zoom in on the 17 s time code after the numerical output has been raised; this is our time reference. We measure the difference between the time reference and the lowering of the numerical output. We use a 17 s time difference because the full sequence was too long for the oscilloscope memory, and the first part of the sequence is where the most instructions are given, hence the biggest contribution to the time jitter. This time jitter corresponds to a relative error of  $0.4 \times 10^{-6}$  which is acceptable and allows the setup to be fully functional.

### 4.2.2 Numerical and analog outputs

The change in output management devices was one of the main motivations to change the software. This system needed some changes as the connections were aging. In the former system, the output cards were directly inserted inside the computer; there were three different output cards, each of which was connected to a box into which the BNC cables were plugged.

A drawback of this system was its heterogeneity: the different analog outputs did not have the same resolution, and special care was given to the output attribution depending on how sensitive an output was to obtaining a BEC. Also, some cards were failing with random offsets appearing on the outputs.

The output connections in the new system take a different approach. As detailed in Fig.4.6, a PXIe 1073 rack is used to host one PXIe-6738 card for the analog outputs and two PXIe-6535 cards for the numerical outputs. The rack is connected using a NI PCI Express host card inside the computer. In total, this provides 64 (two times 32) numerical outputs and 32 analog outputs with a 16-bit resolution. In order to coordinate all these outputs, the pseudoclock signal is sent to the PXIe-6738 card via a TTL cable.

Specifically, the analog outputs deliver a voltage signal to the different devices. The commands sent to the devices are sent in volts unless stated otherwise. It is often more comfortable to work with a unit that matches the delivered signal used by the device that is driven, and to perform this task, a transfer function is available to the user. For each device driven by an analogical output, a transfer function has been coded that allows the user to specify which unit suits the given command best. Multiple units can be given to the same device; an example is the frequency-shift command sent to the AOM: the user can give a command either in MHz or in numbers of D2 transition linewidth. A detailed usage for the sequence will be provided in Sec.4.3.1 and in Fig.4.3 where the choice is given to the user to select in which units the command will be passed to the device.

The output cards are connected to three home-made connector boxes realized by the lab's electronic workshop. This enables the experimentalist to plug in the BNC cables connecting the devices to the laboratory control system. However, as output cards are sensitive electronic devices, to protect the cards and the connectors from ground loops, optocouplers are installed on each BNC connector. This isolates the control system, preventing electrical damage.

### 4.2.3 Radio-frequency generation

The RF generation system uses three main devices. There are two Stanford SRS DS 345 function generators (commonly referred to as Stanford) on the one hand, and on the other hand, a homemade DDS [64] from the lab's electronic workshop. They have different purposes for the experiment.

The Stanfords are used for two reasons: to perform one of the RF ramps for evaporative cooling and to have a small RF signal used for trap spectroscopy. There is one device for each function. These function generators are driven using serial ports, which are no longer used in modern computers. To get around this problem, the devices are connected to the local network with a serial-to-Ethernet adapter and talk to each other over the network with special software. To interact with these devices in the Labscrip Suite, the classes dedicated to the interface between the control system and the Stanford SRS were coded, demonstrating the ability to implement devices specific to the setup.

The homemade DDS is the main device generating radio-frequency signals. Its role is pivotal, as it generates the first RF evaporation field and the dressing RF field. It can generate two kinds of signals: a ramp, which is a linear signal in part, such as the evaporative cooling ramp; and a pattern, which provides much more complex signals. An example of such a signal is the radiofrequency signal used to set the BEC into rotation using the rotating bucket method described in Ref. [64]. The instructions to be executed by the homemade DDS are generated as arrays. As an example, to execute a sequence where the Bose-Einstein condensate is generated, loaded in the bubble trap, and then set into rotation, the DDS will receive a

array for the evaporation signal, another array for the bubble trap loading procedure, and a last array for the rotation pattern. The problem we are facing is that the DDS has limited memory, and only one array can be loaded at a time. To tackle this problem, a development card with a microprocessor was added to the setup, acting as a buffer memory for the DDS. As such, the radiofrequency arrays are generated at the beginning of the sequence and stored in the buffer memory during the sequence. Before the radiofrequency signal is needed, the file is loaded onto the DDS, and then the ramp or pattern is executed at a convenient time. The DDS can only do one thing at a time, and when a ramp instruction is loaded, another ramp can not be executed in parallel. This results in dead times in the sequence, which need to be taken into account. The loading time of a ramp was measured to be around 100 ms whereas the loading time of a pattern to set the trap into rotation is around 2 s. A rotation pattern has to be carefully implemented as the loading time is a dead time. For the experimenter to be able to load the pattern, he or she must add some waiting time before the execution time.

The signals to load and start the ramp are sent through TTL pulses. This organization is specific to this setup and requires a dedicated device in the Labscript Suite to interact with. The classes to interact with the device through Labscript Suite have been written by Romain Dubessy and the DDS, and the card forms a single device to be interacted with.

#### 4.2.4 Camera workflow

The two cameras are controlled separately. An Andor Ixon camera, responsible for the horizontal imaging, is controlled through an acquisition card, whereas an Andor Luca camera, responsible for the vertical imaging, is controlled using a USB connection. These cameras are driven by a different computer than the one running the Labscript Suite. They are controlled directly with a driver written in C++ by Romain Dubessy, who also wrote the Python interface between the camera drivers and the Labscript Suite. Both these devices are not clocked; they are not synchronized with the pseudoclock. The two cameras have a special sequence to start the image acquisition procedure that is triggered using a TTL pulse, synchronized with the light probe pulses at the end of the sequence. At the end of the experimental sequence executed by BLACS, the image files are stored on the computer controlling the camera.

### 4.3 Adaptation of the software to our requirements

The control system has now been presented in Sec.4.1 and the new devices have been introduced in Sec.4.2. It is time to explain the different choices made during the system change.

Firstly, the transcription of the sequence will be explained, along with the requirements for the sequence file to comply with Labscript Suite. The main idea behind this transcription is to use the new system's features, like the ability to change the variable values using Runamanager, while making minimal changes to the sequence structure.

Secondly, the main data analysis script will be detailed. In order to take advantage of Labscript Suite, the previous data analysis system has been adapted to the new system. This has been done through a single-shot analysis script for Lyse, then copying the images in the HDF file and allowing the experimentalist to manipulate the image via a graphical user interface. On top of that, some basic analysis can be performed.

### 4.3.1 Transcription of the sequence

The main sequence has been transcribed from the previous system to the new one. It has been concluded while using the previous system that using a single, modular sequence is more practical than working with multiple sequence files, each focused on one task. The organization of the file is important, and before the sequence, strictly speaking, there are two preparation steps. The first step required by the Labscript Suite formalism is the local connection table. It is a subset of the global connection table presented in the introduction to Sec.4.2. Every device and output mentioned in the file must be defined in the local connection table; otherwise, the sequence compilation is not possible. The second sequence step is the definition of the RF ramps and patterns, in order for them to be edited through Runmanager.

The sequence starts with the instruction `start()`. The first step is the initialization of the time variable and the definition of the numerical value of each output at the start of the sequence. After that, some numerical values are changed in certain situations. An example of such a change is the time of flight, which can be adjusted to the cloud temperature depending on the sequence. The rest of the sequence is a succession of instruction blocks, starting with a boolean value and followed by instructions. An example of a block is given below:

```

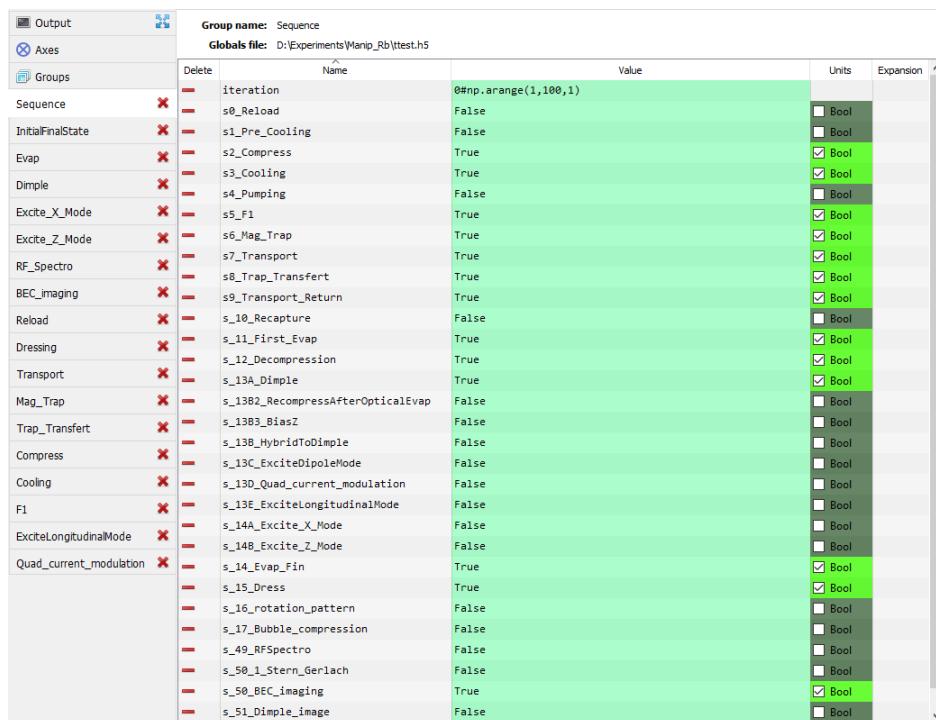
1 ##### Compression of the MOT:
2 if s2_Compress :
3     ### Description
4     print("2- MOT Compression" )
5     ### Wait
6     t+=dtCompressWait
7     ### Do
8     t+=-dtLowerRepump
9     PRepump.constant(t=t,value=PRepumpLow)
10    t+=dtLowerRepump
11    if dtCompress>0 :
12        IQuadTMBas.ramp(t=t,duration=dtCompress,initial=IMOT_TM_Bas,
13                        final=MOTCompress*RapportBasHaut,
14                        samplerate=10000,units='A')
15        IQuadTMHaut.ramp(t=t,duration=dtCompress,initial=IMOT_TM_Haut,
16                        final=MOTCompress,samplerate=10000,
17                        units='A')
18        if s1_Pre_Cooling :
19            BeatNote.ramp(t=t,duration=dtCompress,initial=PrecoolFreq,
20                        final=CompressFreq,samplerate=10000,units='gamma')
21        else:
22            BeatNote.ramp(t=t,duration=dtCompress,initial=MOTWait,
23                        final=CompressFreq,samplerate=10000,units='gamma')
24        PMOTBeam.ramp(t=t,duration=dtCompress,initial=MOTPower,
25                    final=CompressPower,samplerate=10000,units='rel')
26        t+=dtCompress
27    else:
28        IQuadTMBas.constant(t=t,value=MOTCompress*RapportBasHaut,units='A')
29        IQuadTMHaut.constant(t=t,value=MOTCompress,units='A')
30        BeatNote.constant(t=t,value=CompressFreq,units='gamma')
31        PMOTBeam.constant(t=t,value=CompressPower,units='rel')
32        print(f"WARNING:dtCompress has an invalid value. Value:{dtCompress}s.
33              Should be stricly superior to 0.")
34    ### Hold
35    t+=dtCompressHold

```

Listing 4.2 — Example of instruction bloc: the MOT compression bloc

The code example in List.4.2 gives an illustration of Labsript syntax adapted to the sequence. As presented in Sec.4.2.2, the commands given to analogical outputs such as IQquadTMBas specifies a units. For IQquadTMBas, as it drives a current supply, it is more convenient to use the ampere as a unit. The presence of a boolean at start was to use the Runmanager interface while having to do as little code edition as possible. The booleans related to the sequence blocks, such as is s2\_Compress in the code displayed, are grouped together in a dedicated group, as seen in Fig.4.7. The number inside their names orders them according to their places in the sequence, thus preserving the structure of the group. Runmanager has a very visual representation of a boolean with a box that can be ticked when true or unselected when false. On top of that, during the transcription, a security was added in order not to have any problem with the compilation and execution of a ramp: in case the ramp passed a zero or negative ramping time, the instruction is changed, and a warning message is displayed in the Runmanager python console. At the very end of the sequence, the system is set in the same state as the initial one, which allows a MOT to be loaded continuously.

In order to be easily managed, the variables related to each block or group of blocks are stored inside a dedicated group in order. This organization allows for efficient management of variables.



Group name: Sequence		Globals file: D:\Experiments\Wanip_Rb\ltest.hs			
	Delete	Name	Value	Units	Expansion
Sequence	<input checked="" type="checkbox"/>	iteration	0#np.arange(1,100,1)		
InitialFinalState	<input checked="" type="checkbox"/>	s0_Reload	False	<input type="checkbox"/> Bool	
Evap	<input checked="" type="checkbox"/>	s1_Pre_Cooling	False	<input type="checkbox"/> Bool	
Dimple	<input checked="" type="checkbox"/>	s2_Compress	True	<input checked="" type="checkbox"/> Bool	
Excite_X_Mode	<input checked="" type="checkbox"/>	s3_Cooling	True	<input checked="" type="checkbox"/> Bool	
Excite_Z_Mode	<input checked="" type="checkbox"/>	s4_Pumping	False	<input type="checkbox"/> Bool	
RF_Spectro	<input checked="" type="checkbox"/>	s5_F1	True	<input checked="" type="checkbox"/> Bool	
BEC_imaging	<input checked="" type="checkbox"/>	s6_Mag_Trap	True	<input checked="" type="checkbox"/> Bool	
Reload	<input checked="" type="checkbox"/>	s7_Transport	True	<input checked="" type="checkbox"/> Bool	
Dressing	<input checked="" type="checkbox"/>	s8_Trap_Transfert	True	<input checked="" type="checkbox"/> Bool	
Transport	<input checked="" type="checkbox"/>	s9_Transport_Return	True	<input checked="" type="checkbox"/> Bool	
Mag_Trap	<input checked="" type="checkbox"/>	s10_Recapture	False	<input type="checkbox"/> Bool	
Trap_Transfert	<input checked="" type="checkbox"/>	s11_First_Evap	True	<input checked="" type="checkbox"/> Bool	
Compress	<input checked="" type="checkbox"/>	s12-Decompression	True	<input checked="" type="checkbox"/> Bool	
Cooling	<input checked="" type="checkbox"/>	s13A_Dimple	True	<input checked="" type="checkbox"/> Bool	
F1	<input checked="" type="checkbox"/>	s13B2_RecompressAfterOpticalEvap	False	<input type="checkbox"/> Bool	
ExciteLongitudinalMode	<input checked="" type="checkbox"/>	s13B3_BiasZ	False	<input type="checkbox"/> Bool	
Quad_current_modulation	<input checked="" type="checkbox"/>	s13B_HybridToDimple	False	<input type="checkbox"/> Bool	
		s13C_ExciteDipoleMode	False	<input type="checkbox"/> Bool	
		s13D_Quad_current_modulation	False	<input type="checkbox"/> Bool	
		s13E_ExciteLongitudinalMode	False	<input type="checkbox"/> Bool	
		s14A_Excite_X_Mode	False	<input type="checkbox"/> Bool	
		s14B_Excite_Z_Mode	False	<input type="checkbox"/> Bool	
		s14_Evap_Fin	True	<input checked="" type="checkbox"/> Bool	
		s15_Dress	True	<input checked="" type="checkbox"/> Bool	
		s16_rotation_pattern	False	<input type="checkbox"/> Bool	
		s17_Bubble_compression	False	<input type="checkbox"/> Bool	
		s49_RFSpectro	False	<input type="checkbox"/> Bool	
		s50_1_Stern_Gerlach	False	<input type="checkbox"/> Bool	
		s50_BEC_imaging	True	<input checked="" type="checkbox"/> Bool	
		s51_Dimple_image	False	<input type="checkbox"/> Bool	

Figure 4.7 — Display of the sequence group content.

Some other sequences have been written, but their focus was different; their aim was to do a specific calibration requiring a sequence. This is the case, for example, for the shutter timing calibrations or the molasses expansion observation.



### 4.3.2 Data Analysis

Prior to the control system transition, a data analysis system had been coded by the research team to display the absorption images and do a first step of analysis. This system was split into two parts. To visualize the results, a first piece of software called "Vision" was created in C++ and was only available in Windows XP. A more in-depth analysis was done by a second piece of software developed using Matlab. To adapt this whole system was tedious, and it was quicker to analyze the team's needs and code a new analysis script. Here are the main elements wanted to use the new system optimally:

- The shot file should be used as a unique vector of information: Having all the information in the same file and ordered according to the Labscrip Suite hierarchy makes it easier to use all the possibilities of Lyse. As such, the image files should be copied into the HDF file.
- The image files obtained after the sequence have to be processed in order to observe the atoms: Three files are generated after a sequence in order to have an absorption picture. These files contain images of the pulse with and without the atoms, and the last picture is taken without either light or atoms to take into consideration the noise on the camera. On top of that, an algorithm that reduces the fringes on the absorption image [101] is added to reduce the noise on the images. The expressions used for the analysis are presented in Sec.2.4.
- Display and manipulation of the image: In total, there are four different images to display. The result of the calculation presented above is the main picture to display, but it is often useful to look at the raw data taken, for monitoring purposes.
- Quantitative analysis of the images: In order to have quantitative information, one must compare the result to a theoretical model. Therefore, a fitting tool must be easily available to the user.

All these needs were considered, and an analysis script was written. I developed a script using Matplotlib for the graphical interface and the curve plot using Numpy [97] for the calculus performed on matrices and Scipy [98] for the fitting routines. All of the above operations are written in a single-shot script used in Lyse. The graphical user interface of this script is shown in Fig.4.8. The large picture on the left is the zoomed-in picture, which is referred to as the region of interest. On the left side and at the bottom are the integrated profiles, displayed by blue lines. On the right side, there is a representation of the full absorption image, which shows two different rectangles on it. The green rectangle shows the area of interest, and the white rectangle shows the background compensation area, which is used as a reference by the algorithm that gets rid of the fringes. Both of these areas can be modified by the user through the graphical user interface using a rectangle selector on the full picture and the three buttons at the bottom of the full image. On top of the full image, there are three smaller images that display the raw data from absorption imaging. The rightmost image is the pulse with the atom, the middle image is the pulse without the atoms, and the leftmost image displays the image without the atoms. These images are useful to detect when there is a problem with the light pulses and the shutter. Ultimately, the slider at the bottom determines the extremes of the color code of the image that often need to be adapted.

At first, the script only displayed the results, but we quickly realized that being able to fit the data without having to edit the script was a valuable feature. As such, I added the radio

button at the bottom of the full absorption picture. It allows the user to modify the fit model directly using the graphical interface. Only the region of interest is analyzed by the fitting procedure. Once a fit is done, some additional curves are plotted on top of the integrated profiles. As it can be observed in Fig.4.8, there are an orange solid curve and a green dashed curve displayed on the integrated profiles. This is because a bimodal fit has been applied to analyze the image, considering there is a part of the cloud that is thermal and the rest of the cloud is condensed. The orange curve represents the full contribution of the model, whereas the dashed green curve is the contribution of the thermal part. The physical quantities, such as the temperature of the cloud or its extension, are extracted from the fit, displayed in the Python console of Lyse, and stored in the shotfile. This allows the experimentalist to access the data from the fit using other analysis scripts, which has proven useful, for example, when looking at oscillations of the cloud in the trap.

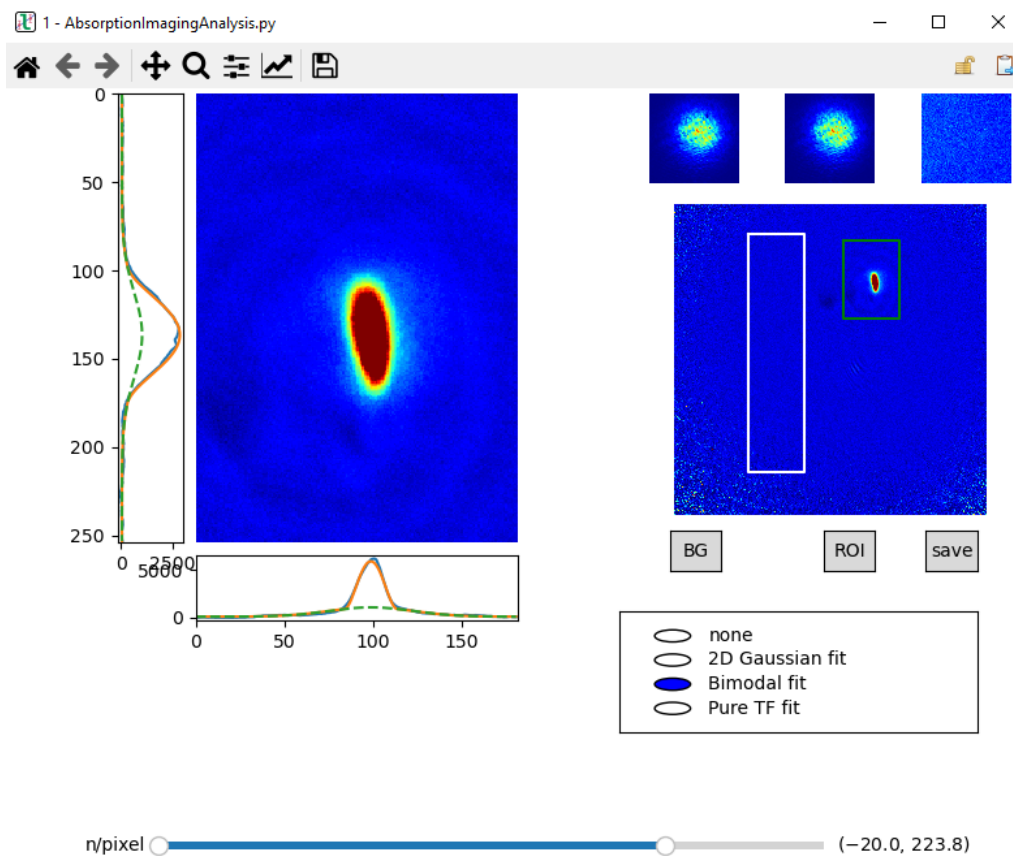


Figure 4.8 – Display of our main analysis script.

## 4.4 Conclusion and future improvements

The transition to the new control system has been successfully implemented. The set-up is fully functional, and all the different devices previously used in the old control system are usable with the Labscript Suite. The new control system is also more efficient at acquiring data. To give the reader an idea of this improvement, before the transition we were taking around

200 images a day, a figure that has been increased by a factor of 3 with the new system. This is mainly due to an easier handling of the parameters related to the radiofrequency control, and the generation of multiple shot files and their sequential executions, which drastically reduce the dead times between sequence executions.

The new control system is useful and efficient, but the situation can still be improved. In order to do so, the next step is to integrate a laser lock management system inside the Labscrip Suite. By having an automated check of the laser lock status before the execution of the sequence, the reliability of the system would be increased as the sequence would be executed only when the lasers are locked. The ideal solution would be an automated relock procedure. This would ensure that any long set of measurements could still be used without the need for a constant check by the experimentalist.

# Chapter 5

## Optimization of the experiment via machine-learning algorithms

The new control system, Labsript Suite, enables the experimentalist to use the different features, increasing the performance of the experiment. However, the experiment tuning process remains a long process that one wishes to optimize. A way to achieve this aim is to use a machine-learning algorithm to optimize the experiment according to a given criterion. These algorithms are becoming increasingly popular amongst the physics community and lead to an increase in performance in atomic physics like optimizing a magneto-optical trap [48], producing a BEC in the shortest time span [102] or finding suitable constraints for a cosmological model [103].

On the laboratory experimental setup, some repetitive optimization tasks are done every day, such as the fine-tuning of the plug position. The optimization criterion was always the same: having the largest number of atoms at the lowest temperature possible. The results given by the machine learning algorithm to perform this kind of optimization had been demonstrated [53], we decided to follow these first results to automate these optimizations.

First, a description of the interactions between Labsript-Suite, the new control system, and M-LOOP [104], the machine learning package chosen, will be presented, along with a description of the cost to minimize. Then, the algorithms used to optimize the experiment will be described. Ultimately, the experimental optimization session will be detailed and the results commented.

### 5.1 Implementation specificity

#### 5.1.1 M-LOOP and its interaction with the Labsript-Suite

One of the new desirable features that would be interesting to have is the automatic optimization of the experiment given a certain criterion. The aim is to automate a part of the repetitive tasks done on a day-to-day basis by the experimentalist in order to be more efficient. A concrete example of such a task would be tuning the dimple beam position described in Sec.2.2.2: this task consists in finding the position of the dimple beam that maximizes the number of atoms in the BEC in the hybrid trap. It is a simple task done once or twice a day and takes from a few minutes up to an hour.

In order to implement this automation, M-LOOP [104] was chosen. It is a Python library developed by Australian scientists working on cold atom experiments. M-LOOP is the acronym for machine-learning online optimization package. Machine-learning refers to the type of algorithm used to perform the optimization, and online optimization refers to an optimization where there is a lack of knowledge about the problem [105]. A direct consequence is the potential non-existence of an improved solution to such a problem. Moreover, the library has a visualization option, enabling the experimentalist to see the result of its optimization sequence. Different algorithms have been implemented, such as differential evolution, Gaussian process regression, and the Nelder-Mead algorithm, to name a few.

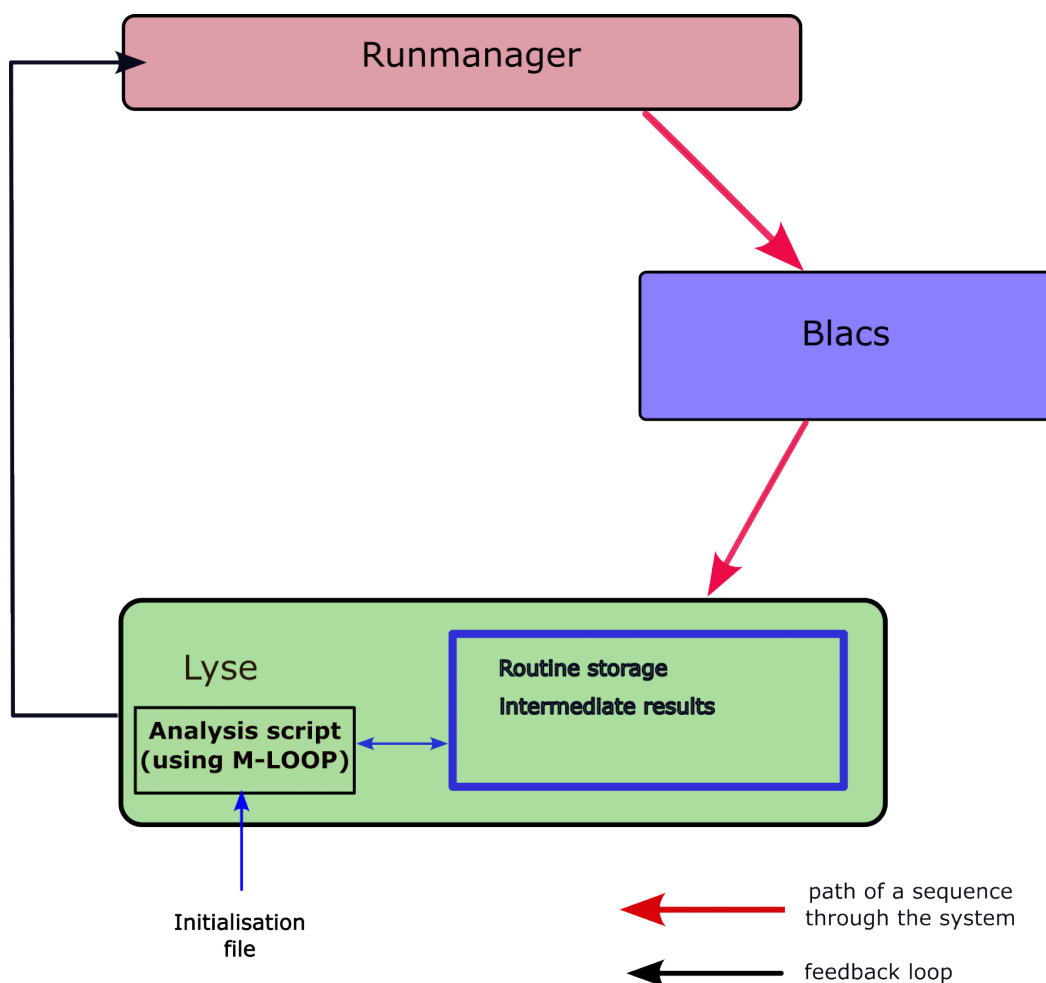


**Figure 5.1** — Representation of M-LOOP integration with the feedback loop and the routine storage.

The integration of M-LOOP inside the Labscript Suite is done via the project called `analysislib-mloop` [106]. This project is used through script by Lyse, as shown in Fig.5.1. For the sequence to be compiled without the intervention of the experimentalist, Runmanager is controlled remotely by Lyse using a command line in the analysis script. Also, a routine

storage is used to store intermediate calculations during the optimization session. This routine storage allows the user to store some information for the analysis of multiple files that are not stored inside the shot files.

The experimentalist prepares an optimization session by editing a configuration file. As we are dealing with online optimization, a stopping criterion needs to be defined before the session starts. This is done by defining two quantities: the maximum number of runs in the session and the maximum number of runs without improvement. The experimentalist also details the upper and lower bounds for each parameter (based on his knowledge of the experiment). In this configuration file, the parameters selected to be changed in the optimization session are set. For each parameter, three values must be given: the upper bound, the lower bounds and the initial value for the first run of the session. The algorithm used to optimize this session can be changed in this file. The experimentalist must be cautious that every parameter is defined and active in Runmanager. And most importantly, the name of the cost to optimize is defined.

### 5.1.2 Construction of a cost to minimize

For the algorithm to work, one must define a criterion to optimize, which in optimization language translates into a cost to minimize. We decided to maximize the number of atoms in the Bose-Einstein condensate. This corresponds to maximizing the central density after a time of flight, as the BEC expands more slowly than the thermal cloud surrounding it.

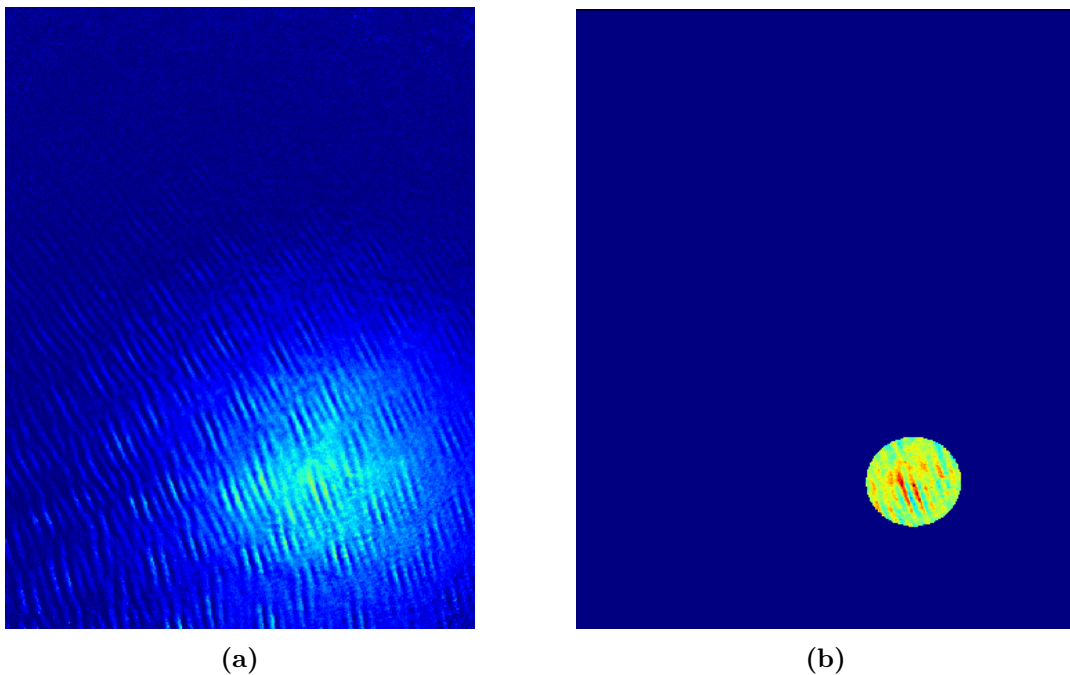


**Figure 5.2** — Illustration of the difference between the absorption imaging picture and the cost picture. The situation corresponds to the image taken after the first stage of evaporative cooling. 5.2a is an absorption imaging picture. 5.2b is the area over which the cost associated with the picture taken in 5.2a is calculated.

As detailed in Sec.4, to extract the physical quantities of the cloud, a fit is performed

on the final picture. From the information given by the fit, physical quantities such as the temperature are determined. This brings a level of complexity to the cost evaluation: if the cost is based on the physical quantities, when the fit procedure fails, the cost is meaningless. It happens when the number of atoms is low and the cloud is wide. In such a situation, the fit analysis is often incorrect. So the question is: how to build a cost that is robust to a fit failure and enables the experimentalist to increase the phase-space density? The strategy for the cost evaluation relies uniquely on studying the atomic density of the cloud [53]. The global aim is to maximize the number of atoms inside a given area, resulting in maximizing the phase-space density of the cloud.

Let me detail the automatic procedure to determine the cost step by step. First the position of the maximum atomic density is determined. Its coordinate are deduced from the atomic density integrated profile along the camera axis. It has been observed experimentally that using the integrated profile to determine the maximum reduces the sensitivity to the pixel-to-pixel fluctuation. Then a circle mask is applied around the position of the previously determined maximum: all the pixels inside the circle are left untouched, whereas the pixels outside the circle are set to zero. Then the number of atoms detected on each pixel is added, this quantity is called  $\Sigma$ . Therefore,  $\Sigma$  is the number of atoms inside the mask. In order to have a decreasing function with respect to the increasing atom number and because the cost should be sensitive to large improvements over this measurement and almost ignore small changes, the cost used to evaluate a picture is given by:

$$\text{Cost} = -\log(\max(\Sigma, 1)) \quad (5.1)$$

The deep blue part of Fig.5.2b is all the pixels set to zero, and the colorful circle is the area contributing to the cost.

## 5.2 Presentation of the algorithms

Here, the algorithms used during the optimization session are presented. Only the Gaussian process regression had been used directly for optimization purposes. The differential evolution algorithm had been used to initialize the Gaussian process regression algorithm by providing a set of data to initialize the optimization session.

### 5.2.1 Differential evolution

The differential evolution algorithm is an algorithm that mimics the mechanism of natural selection [107]. The idea is to look for improvements in a starting population via hybridization and spontaneous mutation.

The situation starts with a set of configurations generated randomly:  $\{\mathbf{X}_1, \mathbf{X}_2, \dots, \mathbf{X}_i\}$ . The set of configurations is known as the population. The first step of the algorithm is to select randomly 3 elements amongst the population noted as  $\mathbf{X}_p$ ,  $\mathbf{X}_q$ , and  $\mathbf{X}_r$  and to construct a new vector  $\mathbf{V} = \mathbf{X}_p + (\mathbf{X}_q - \mathbf{X}_r)$ . Then the next configuration to be tested,  $\mathbf{X}_{new}$ , is determined by selecting each component randomly from either  $\mathbf{V}$  or  $\mathbf{X}_i$ . The cost associated with this new configuration,  $Y_{new}$ , is determined by running it experimentally. Finally, if the cost  $Y_{new} < Y_i$ , the new pair takes the place of the pair  $\{\mathbf{X}_i, Y_i\}$ , and if that is not the case, the new pair is dismissed. The process is repeated a certain number of times. This algorithm is not expansive in terms of calculation, but it converges slowly towards an optimum.

On the experiment, this algorithm is used to ‘train’ the main algorithm, which is the Gaussian Process Regression detailed in Sec.5.2.2. This algorithm needs a collection of data to be used, therefore the differential evolution algorithm is applied to select a set of couples  $\{\mathbf{configuration}, \text{cost}\}$ .

### 5.2.2 Gaussian Process Regression

The Gaussian process regression (GPR) takes a different approach: based on the previous measurements done on the experiment, the algorithm makes an educated guess on which configuration to evaluate next. The main idea is to exploit the previously acquired data to infer a new configuration to optimize a given criterion. I will start by introducing some elements of probability theory. Then the foundational concept of this algorithm is presented: the Gaussian Process. It is followed by a small derivation on how the inference is done in order to extract new information about the problem. Ultimately, the algorithm applied to the experiment is detailed with an example, and a way to incorporate the fluctuation in the measurements is presented. This part is based on chapter 2 of [108].

First, this algorithm relies on probability theory, and more precisely, on conditional probability. The main idea is to look at the likelihood of event A occurring given that event B has already taken place. This probability is denoted by the mathematical expression  $P(A|B)$  and its expression is:

$$P(A|B) = \frac{P(A \cap B)}{P(B)} \quad \text{if } P(B) \neq 0 \quad (5.2)$$

The use of conditional probability is ubiquitous in numerous fields requiring statistical analysis. Its application includes analyzing the efficacy and dependability of drug testing protocols. Another key mathematical object to introduce is the multivariate normal distribution. A normal distribution is one of the best-known mathematical objects: it is a probability distribution with a bell-shaped curve that peaks at a given value  $m$  and a width  $\sigma$ . The full mathematical expression of a random variable  $X$ ’s normal probability distribution function with respect to the value  $x$  is:

$$f_X(x) = \frac{1}{\sqrt{2\pi}\sigma} \exp\left(\frac{-(x-m)^2}{2\sigma^2}\right) \quad (5.3)$$

And the probability to find the variable  $X$  between  $x = a$  and  $x = b$  is:

$$P(a < X < b) = \int_a^b \frac{1}{\sqrt{2\pi}\sigma} \exp\left(\frac{-(x-m)^2}{2\sigma^2}\right) dx \quad (5.4)$$

Now suppose the reader is interested in having multiple random variables all following the same joint probability distribution. The previous definition needs to be extended to pick a random vector. To fully determine the multivariate normal distribution, one should specify:

- The mean vector  $\boldsymbol{\mu}$ : a vector of  $n$  component,  $n$  being the number of random element desired. This is the central value centered on which the random vector peaks.
- The covariance matrix  $\Sigma$ : a square matrix of size  $n$ . This matrix’s elements each have their own meaning. The diagonal elements determine the variance, or the width, of the distribution of each component. The off-diagonal terms represent the covariance, a measure of how two components of the random vector evolve with respect to one another. If the covariance is positive between the variables A and B, when the variable A increases, the variable B increases. If the covariance is negative, when A increases,



the variable  $B$  decreases.

The  $\Sigma$  matrix is symmetric and positive semidefinite.

The probability density function of the  $n$ -dimensional multidimensional Gaussian is:

$$f_{\mathbf{X}}(x_1, \dots, x_n) = \frac{1}{\sqrt{(2\pi)^n \det(\Sigma)}} \exp(-(\mathbf{x} - \boldsymbol{\mu})^T \Sigma^{-1} (\mathbf{x} - \boldsymbol{\mu})/2) \quad (5.5)$$

As a normal distribution is fully defined by its mean and variance, another notation is  $X \sim \mathcal{N}(m, \sigma)$  for the one dimensional case and  $\mathbf{X} \sim \mathcal{N}(\boldsymbol{\mu}, \Sigma)$  for the multidimensional case. This means  $X$  ‘follows’ the distribution specifies afterward.

Let us now formulate the problem. We start with a set of data composed of pairs of configurations and costs; this is the training data set. It is noted  $\mathcal{D} = \{(\mathbf{x}_i, y_i) | i = 1, \dots, n\} = \{X, \mathbf{y}\}$  where  $X$  is the matrix with the  $n$  configuration vectors and  $\mathbf{y}$  is the vector with the  $n$  associated costs. We don’t know how our cost function will behave a priori. This means the cost function is considered random but repeatable, which means if the same configuration is evaluated twice, the same result will be obtained. The cost  $y$  is defined as follows:

$$y = f(\mathbf{x}) \quad (5.6)$$

And no fluctuation is considered at first.

To model the cost function, a Gaussian process is used; it is a collection of random variable where a finite number of these random variables share a joint Gaussian distribution [108, 109]. This object is fully specified by its:

- mean function:

$$m(\mathbf{x}) = \langle f(\mathbf{x}) \rangle \quad (5.7)$$

- covariance function:

$$k(\mathbf{x}, \mathbf{x}') = \langle (f(\mathbf{x}) - m(\mathbf{x}))(f(\mathbf{x}') - m(\mathbf{x}')) \rangle \quad (5.8)$$

Where  $\langle X \rangle$  is the average value of  $X$ . The Gaussian process is related to the function  $f(\mathbf{x})$  by:

$$f(\mathbf{x}) \sim \mathcal{GP}(m(\mathbf{x}), k(\mathbf{x}, \mathbf{x}')) \quad (5.9)$$

The Gaussian process is a generalization to an infinite dimension of a multidimensional normal distribution. By convention, the mean function is set to 0, and the covariance function used is:

$$k(\mathbf{x}, \mathbf{x}') = \exp\left(-\frac{1}{2} \sum_{i=1}^n \eta_i (x_i - x'_i)^2\right) \quad (5.10)$$

This is known as the radial basis function. In the expression (5.10),  $\mathbf{x}$  and  $\mathbf{x}'$  are two configurations expressed as vectors of size  $n$ , which is the number of parameters in the optimization sequence. The terms  $x_i$  (respectively  $x'_i$ ) refers to the  $i$ -th component of the vector the  $\mathbf{x}$  (respectively  $\mathbf{x}'$ ). Finally, the terms  $\eta_i$  are inversely proportional to the square of the characteristic length scale associated with the  $i$ -th element of the vector.

This allows us to associate a normal distribution with the cost vector. Also, one wishes to evaluate the function at the arbitrary configuration  $\mathbf{x}_*$  and to have an estimation of the associated cost before the evaluation of  $f(\mathbf{x}_*)$ . The starting point is to write the joint Gaussian distribution associated to the set of data composed of the  $D$  vectors of the training data set

plus the expression of our arbitrary point  $\mathbf{x}_*$  based on the property of the Gaussian process. Because the cost functions follows the Gaussian process, the cost vector then follows the normal distribution. This normal distribution is given by Eq.(5.11) where the mean has been set to 0 based on the properties of the Gaussian process. The covariance function  $k$ , given by Eq.(5.10), allows one to write the normal distribution's covariance matrix.

$$\begin{bmatrix} \mathbf{y} \\ y_* \end{bmatrix} \sim \mathcal{N}(\mathbf{0}, \begin{pmatrix} k(\mathbf{x}_1, \mathbf{x}_1) & \cdots & k(\mathbf{x}_1, \mathbf{x}_D) & k(\mathbf{x}_1, \mathbf{x}_*) \\ \vdots & \ddots & \vdots & \vdots \\ k(\mathbf{x}_D, \mathbf{x}_1) & \cdots & k(\mathbf{x}_D, \mathbf{x}_D) & k(\mathbf{x}_D, \mathbf{x}_*) \\ k(\mathbf{x}_*, \mathbf{x}_1) & \cdots & k(\mathbf{x}_*, \mathbf{x}_D) & k(\mathbf{x}_*, \mathbf{x}_*) \end{pmatrix}) \quad (5.11)$$

To simplify the notation we set:

- The covariance matrix of the training data set  $K = K(X, X)$  where the covariance matrix  $K(X, X')$  between two data sets  $X$  and  $X'$  that can be of different sizes  $D$  and  $D'$  is defined by

$$K(X, X') = \begin{pmatrix} k(\mathbf{x}_1, \mathbf{x}'_1) & \cdots & k(\mathbf{x}_1, \mathbf{x}'_{D'}) \\ \vdots & \ddots & \vdots \\ k(\mathbf{x}_D, \mathbf{x}'_1) & \cdots & k(\mathbf{x}_D, \mathbf{x}'_{D'}) \end{pmatrix}$$

- The covariance vector  $\mathbf{k}_*^T = (k(\mathbf{x}_*, \mathbf{x}_1) \cdots k(\mathbf{x}_*, \mathbf{x}_D)) = K(\mathbf{x}_*, X) = K(X, \mathbf{x}_*)^T$
- The variance associated to the new configuration  $k_* = k(\mathbf{x}_*, \mathbf{x}_*)$

There is now a full expression for the joint multivariate Gaussian distribution of the cost vector. However, there is only one element worthy of interest in this vector: the cost  $y_* = f(\mathbf{x}_*)$ . To go a step further, a property of the Gaussian normal distribution is needed, the conditional marginalization property of the joint normal distribution [110]. It states that an  $n$ -dimensional normal distribution noted  $\mathcal{N}(\boldsymbol{\mu}, \Sigma)$  can be partitioned into a  $p$ -dimensional and a  $q$ -dimensional normal distribution with  $n = p + q$ :

$$\mathbf{x} = \begin{bmatrix} \mathbf{x}_1 \\ \mathbf{x}_2 \end{bmatrix} \sim \mathcal{N}(\boldsymbol{\mu}, \Sigma) \quad \boldsymbol{\mu} = \begin{bmatrix} \boldsymbol{\mu}_1 \\ \boldsymbol{\mu}_2 \end{bmatrix} \quad \Sigma = \begin{bmatrix} \Sigma_{11} & \Sigma_{12} \\ \Sigma_{12} & \Sigma_{22} \end{bmatrix} \quad (5.12)$$

In Eq.(5.12):

- $\boldsymbol{\mu}_1$  is a vector with  $p$  terms and  $\boldsymbol{\mu}_2$  is a vector with  $q$  terms.
- $\Sigma_{11}$  is a  $p \times p$  matrix,  $\Sigma_{12}$  is a  $p \times q$  matrix,  $\Sigma_{21}$  is a  $q \times p$  matrix,  $\Sigma_{22}$  is a  $q \times q$  matrix. All these matrices are sub-matrices of  $\Sigma$ .

In such a case, the distribution of  $\mathbf{x}_1$  conditioned to  $\mathbf{x}_2$  is the joint normal distribution  $\mathcal{N}(\bar{\boldsymbol{\mu}}, \bar{\Sigma})$  where:

$$(\mathbf{x}_1 | \mathbf{x}_2) \sim \mathcal{N}(\bar{\boldsymbol{\mu}}, \bar{\Sigma}) \quad \bar{\boldsymbol{\mu}} = \boldsymbol{\mu}_1 + \Sigma_{12} \Sigma_{22}^{-1} (\mathbf{x}_2 - \boldsymbol{\mu}_2) \quad \bar{\Sigma} = \Sigma_{11} - \Sigma_{12} \Sigma_{22}^{-1} \Sigma_{21} \quad (5.13)$$

Using Eq.(5.13), one can write the conditional probability of  $f(\mathbf{x}_*)$  taking into account the training dataset with parameters  $X$  and associated results  $\mathbf{f}$  and the new configuration  $\mathbf{x}_*$ , which is:

$$(f(\mathbf{x}_*) | \mathbf{x}_*, X, \mathbf{f}) \sim \mathcal{N}(\mathbf{k}_*^T K^{-1} \mathbf{f}, k_* - \mathbf{k}_*^T K^{-1} \mathbf{k}_*) \quad (5.14)$$

Therefore, Eq.(5.14) is the probability distribution of the cost at a given configuration  $\mathbf{x}_*$ . Before going any further, a few elements need to be pointed out. First, we have a probability density distribution based on the training data set and the new configuration expression. Also, the normal distribution in one dimension is specified by its mean and its variance, and the mean of the Gaussian is also its most probable outcome. This means the mean value of the distribution specified in Eq.(5.14) gives an estimation of the cost for every configuration the experimentalist wants to consider. Similarly, the variance of this probability density function gives the value of the width of the distribution around the mean value. It can be viewed as an estimation of the uncertainty on the expected results as defined by the mean value. In short, with this normal distribution, the experimentalist has an estimation of the cost and the uncertainty associated with it for each point in the configuration space.

A risk function, based on the probability density function of the cost, determines which configuration to evaluate next. The choice of this risk function reflects the strategy the experimentalist wishes to implement to minimize the cost [111]. In the case of the acquisition function used by M-LOOP, the cost function finds the minimum of the cost determined by:

$$\mathcal{R}_{\mathcal{L}}(f(\mathbf{x}_*)|\mathbf{x}_*) = \text{Expected Cost} + \text{Uncertainty} \quad (5.15)$$

The quantity  $\mathcal{R}_{\mathcal{L}}$  is referred to as the risk. The cost is the mean value of the probability density distribution function, and the uncertainty is its standard deviation, the square root of the variance. Using Eq.(5.14), this risk writes in our case  $\mathcal{R}_{\mathcal{L}}(f(\mathbf{x}_*)|\mathbf{x}_*) = \mathbf{k}_*^T K^{-1} \mathbf{f} + \sqrt{k_* - \mathbf{k}_*^T K^{-1} \mathbf{k}_*}$ . The aim is to minimize this function, so find:

$$y_{min}|\mathbf{x}_* = \underset{y_{est}}{\operatorname{argmin}}(\mathcal{R}_{\mathcal{L}}(y_{est}|\mathbf{x}_*)) \quad (5.16)$$

In the expression above,  $y_{est}$  is the estimated value of the function. Because the exact value of the function is unknown, one can only rely on the estimations obtained by using the Gaussian Process for both cost and uncertainty. It is worth reminding the reader that our cost is negative and the value of the standard deviation of the normal distribution function is necessarily positive; therefore, an increase in the standard deviation is detrimental to the risk function. This strategy can be understood as the will to prioritize a moderate, almost certain gain — a small improvement with low uncertainty - over a hypothetical great improvement - large improvement with a large uncertainty. Once  $y_{est}$  is determined, the experiment runs it and the associated cost is computed. The pair composed of the new configuration and its cost is added to the set of data, and the algorithm starts once again by doing a regression with the updated set of pairs composed of configuration and cost.

An example of the way the GPR operates is given in Fig.reffig:illustrateGPR. The function  $f(x) = x \sin(x)$  is the function unknown to the GPR and the aim is to find a minimum on the curve based on the data obtained. The red dots are the points already evaluated and where the function behavior is known. Based on these data, a probability density function is determined using Gaussian process regression. Using this probability density function, the mean of the cost function is determined for each point and is represented as the dark blue line on the graphs. Because the model is probabilistic, this mean has a certain confidence interval associated with it, and the light blue area around the mean value represents the zone around the mean where it is estimated that there is 95% chance for the value of the function to be in that range. Using the acquisition function, the next point to evaluate is determined to be close to  $x = 5$  as it is the point where there is a maximum chance to find a point having a lower value with the most certainty given the data known in Fig.5.3a. Once the function is

evaluated, the situation becomes 5.3b. The uncertainty area becomes smaller around the last point evaluated.

The advantages of the Gaussian process algorithm are its quick convergences and the low amount of data to be initialized. Also, after the session has finished, the length-scale value will be known, which gives the experimentalist some information about which parameters are the most important. The drawback is that this algorithm is computationally intensive and becomes slow when there are dozens of parameters in the optimization session.

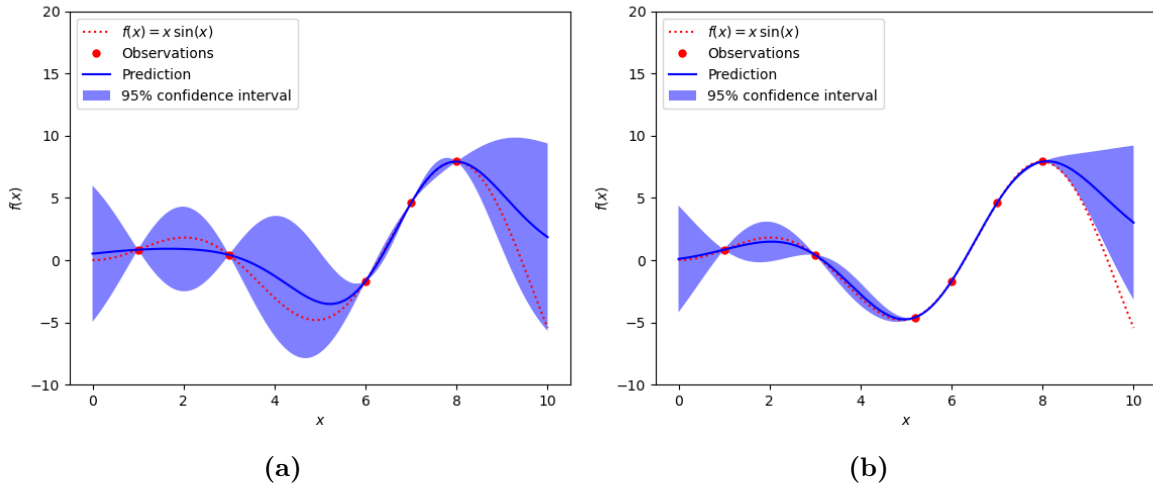


**Figure 5.3** — Illustration of an example of decision-making using Bayesian optimization using a function of one variable. 5.3a represents the situation before the next point is determined. 5.3b represents the situation after the new configuration has been evaluated.

The situation depicted in Fig.5.3 is an example given without noise, that is to say there is no fluctuation on the experiment. This situation does not faithfully represent an experimental realization on the laboratory setup because two identical realizations of the sequence lead to slightly different absorption imaging pictures, thereby, associating slightly different costs. One of the Gaussian process regression interesting feature for the experimentalist is its ability to take into account the noise on measurements. This is done by modifying the expression of cost by introducing a small noise,  $\epsilon$ :

$$y = f(\mathbf{x}) + \epsilon \quad \epsilon \sim \mathcal{N}(0, \sigma_\epsilon) \quad (5.17)$$

The fluctuation is assumed to be Gaussian, centered around 0, and with a variance  $\sigma_\epsilon$ . In order to take these fluctuations into account, one needs to slightly change the covariance function:

$$\text{cov}(y_a, y_b) = k(\mathbf{x}_a, \mathbf{x}_b) + \sigma_\epsilon^2 \delta_{a,b} \quad (5.18)$$

This leads to an additional term inside the covariance matrix of Eq.(5.11) which becomes:

$$\begin{bmatrix} \mathbf{y} \\ y_* \end{bmatrix} \sim \mathcal{N}(\mathbf{0}, \begin{pmatrix} K + \sigma_\epsilon^2 I_D & \mathbf{k}_* \\ \mathbf{k}_*^\top & k_* \end{pmatrix}) \quad (5.19)$$

In Eq.(5.19),  $I_D$  refers to the identity matrix of dimension  $D$ . The change in the covariance matrix brings a change in the probability density function, which becomes:

$$f(\mathbf{x}_*)|\mathbf{x}_*, X, \mathbf{f} \sim \mathcal{N}(\mathbf{k}_*^T(K + \sigma_\epsilon^2 I_D)^{-1}\mathbf{f}, k_* - \mathbf{k}_*^T(K + \sigma_\epsilon^2 I_D)^{-1}\mathbf{k}_*) \quad (5.20)$$

We get a prediction very similar to the noiseless prediction, the main difference being the addition of a term in the inverse matrix to determine both the variance and the mean. Up until now, we did not implement the possibility of adding an uncertainty to the cost function in the experiments we performed. This could be relevant for a future improvement of the optimization procedure.

### 5.3 Results obtained using machine-learning algorithms

The results presented here show the results obtained following various optimization sessions. This section had been modified after the defense to incorporate the latest set of data. A presentation of each series of optimization will be presented alongside a problem which had been discovered during a careful investigation of our data.

#### 5.3.1 Transfer from the hybrid trap to the dressed trap: Identification of an important parameter

In parallel with the implementation of M-LOOP, the change of BEC production in the science cell was implemented. The hybrid trap was done by plugging a blue-detuned laser beam focused on the trap center and is now done by attracting the atoms away from the trap center. Both of these methods are presented in Sec.2.2.2. Once a Bose-Einstein condensate had been observed in the new hybrid trap, referred to as the dimple trap, many attempts had been made to load the BEC in the dressed trap. In order to improve the dressed trap loading, an optimization session concerning the dressing ramp and the progressive extinction of the dimple laser beam was run. This corresponds to a session with six parameters, and the part of the sequence that is optimized is shown in Fig.5.4. The optimization session may be summarized by attempting to answer the question: How to synchronize the dimple's extinction with an adapted radiofrequency ramp?

The first conclusion drawn from this attempt was the need to change the geometry of the cost window. Due to the strong anisotropy of the oblate BEC, the cloud is strongly confined in the vertical direction of the trap inside the bubble and after a 23 ms time of flight the anisotropy inverts and the cloud expands more in the vertical direction, resulting in an oval-shaped cloud on the imaging system for the BEC [112]. In order to take this effect into account, the geometry of the cost window has been changed to an oval shape.

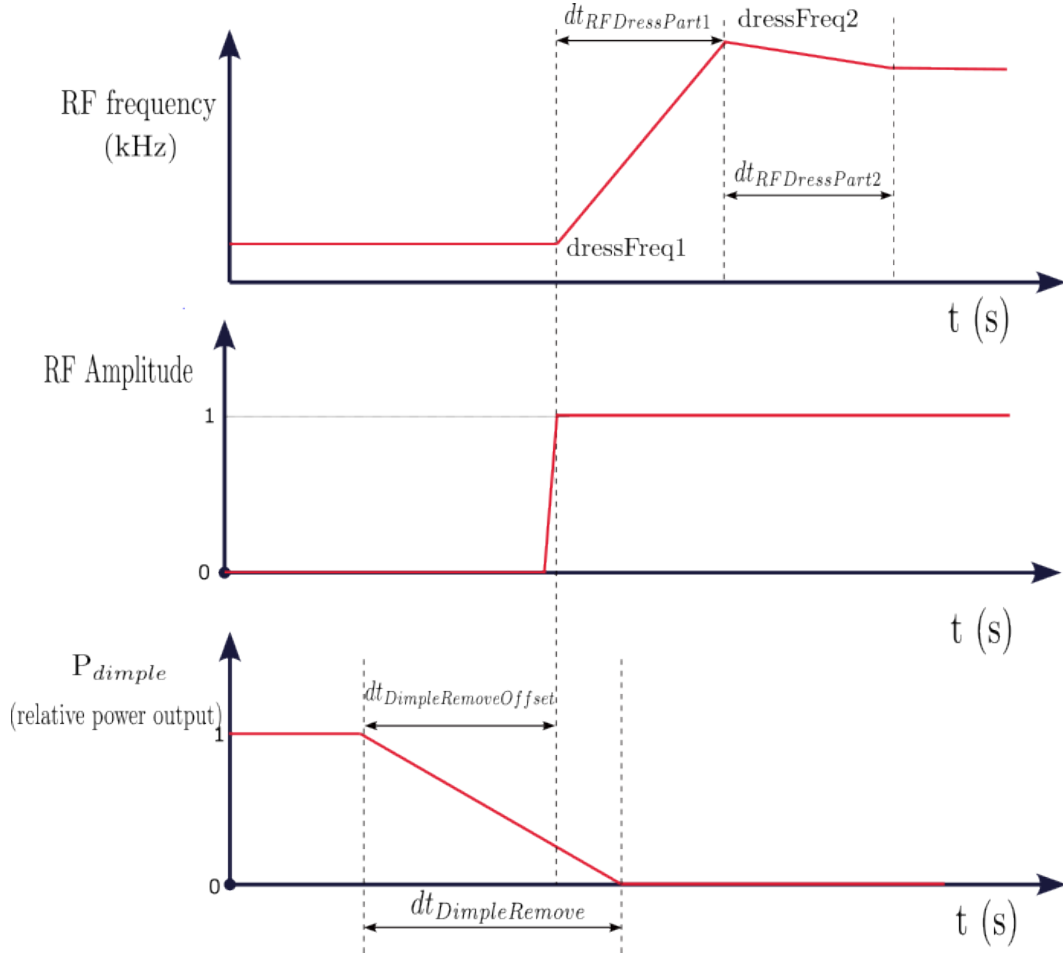


**Figure 5.4** — Representation of the sequence's signals.

The optimization session is organized in two phases. First, a training phase of 20 shots is performed with the differential evolution algorithm. Then the Gaussian process is used to determine which configuration should be evaluated next. Each fifth sequence, the differential evolution algorithm is used to determine the next shot. The cost evolution with respect to the number is shown in Fig.5.5 where the cyan triangles represent the configurations determined with differential evolution algorithm and the blue dots are the configurations obtained with the Gaussian process regression. This session stopped after 180 iterations. This number has been determined to have optimization session which lasts for at most 3 hours, in order to avoid some drifts of the experiments which can not be compensated by the experimentalist during the optimization session.

At the end of the optimization sequence, MLOOP provides various information. Amongst these information, we are particularly interested in the best configuration evaluated during the session and the sensitivity estimation for each parameters. This sensitivity estimation is obtained by looking at the characteristic length scale for each parameters, the shorter this length-scale is, the more sensitive the parameter is. These information are shown in Tab.5.1 but they are not directly coming from MLOOP.

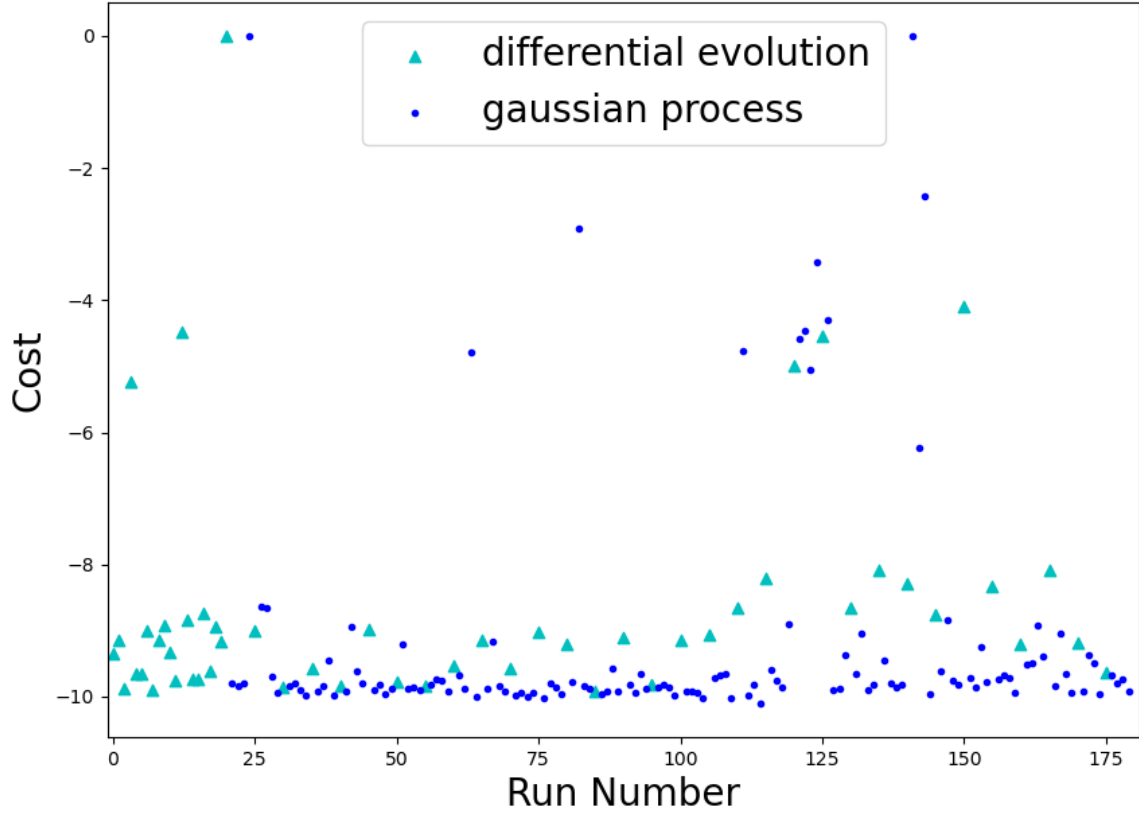


**Figure 5.5** – Graph displaying the evolution of the cost with respect to the Run number for the trap transfer optimization.

Actually, during the data analysis phase, we discovered that the parameters analysis by MLOOP was different from the situation described in Sec.5.2.2: the covariance function used during the optimization session was the following:

$$k(\mathbf{x}_i, \mathbf{x}_j) = \exp\left(-\frac{1}{2} \frac{d(\mathbf{x}_i, \mathbf{x}_j)^2}{l^2}\right) \quad (5.21)$$

Showing that the characteristic length scale was imposed to the same for all parameters.

In order to get information about the individual characteristic length scale of each parameter, I perform a posterior analysis on the data, which is a Gaussian process regression using the whole set of data from the optimization session. This is the ultimate step of the optimization session, but this last step is not equivalent to the full optimization session: as MLOOP performs an online optimization, the data are analyzed throughout the optimization session to determine the next configuration to be evaluated. Therefore, analyzing the whole set of data a posteriori is not equivalent to using the Gaussian process regression algorithm to optimize the experiment, as the analysis lacks the step-by-step component of the GPR optimization session.

variable name (unit)	Pre-optimization configuration	Post-optimization configuration	Length-scale (dimensionless)	$\Delta P_j$
dressFreq1 (kHz)	276.49	207.62	0,17433	200 kHz - 300 kHz
dressFreq2 (kHz)	331.83	300.00	10,0	300 kHz - 400 kHz
dtRfDressPart1 (ms)	130.05	87.07	0,01813	50 ms - 500 ms
dtRfDressPart2 (ms)	312.7	66.1	0,26817	50 ms - 500 ms
dtDimpleRemove (ms)	345.19	209.78	0,07165	50 ms - 500 ms
dtDimpleRemove Offset (ms)	319.67	297.22	0,05492	50 ms - 600 ms
costs	-9.353	-10.106		

**Table 5.1** – The variables optimized for the transfer procedure. For each of them, there is the starting value and the optimized value. The initial and final costs are also given.

In Tab.5.1, I choose to display the dimensionless characteristic length-scales in order to compare the length-scale of each parameter. They are defined by  $\tilde{l}_j = l_j/\Delta P_j$  where  $\Delta P_j$  is the allowed range of variation fixed by the experimentalist. One of the parameters stands out: dressFreq2, which has a large dimensionless characteristic length-scale, which means the variation of this parameter, in its allowed range, does not change the cost of a realization. The most sensitive parameter, the parameter having the lowest dimensionless characteristic length-scale, is dtRfDressPart1 highlighting, the sensitivity of this parameter. Then, the dtDimpleRemove and dtDimpleRemoveOffset are the most sensitive, insisting on the importance of the coordination between the dimple beam shutting down and the RF field being switched on.

The optimization of this part of the experiment had been successful, as it doubled the number of atoms in the BEC, passing from  $5 \times 10^4$  to  $10^5$ . This illustrates a case where the M-LOOP package can be useful: when a modification is implemented on the experiment and an optimization has to be done where we have very little knowledge on the behavior of the cost with the parameters, the algorithm can save time by exploring more efficiently the space of possible parameters and finding an optimum in a shorter time.

### 5.3.2 Pre-transport phases: an optimization with numerous parameters

Once M-LOOP had been implemented within the new control system, optimization of the pre-transport stage of the sequence was tried. This part of the sequence is described in Sec.2.2.1. As a reminder, this corresponds to the pre-compression phase, the molasses and Sisyphus cooling phase, the pumping to  $F = 1$  stage and the final compression stage before transport. In total, this optimization sequence takes into account the 15 parameters presented in Tab.5.2. In order to analyse the cloud profile on the camera, the cloud has to be translated and transferred in the quadrupole science cell, up to the first evaporation stage. This is the first stage at which a picture of the atom can be taken with our imaging system of magnification 2.4 and with 15 ms.



The first attempts gave a mixed result: M-LOOP ran the optimization sequence, which converged toward an optimum, but the cloud of atoms was indistinguishable from the cloud prior to the optimization sequence. The cost associated with both of these situations was  $-14.8$ . Because we wanted to be sure that an improvement could be found using machine learning on the laboratory set-up, the parameters had been changed to a degraded configuration, corresponding to a cost of  $-11.4$  for a circle with a radius of  $500\mu\text{m}$ . During the redaction time, we realized there was a problem with the characteristic length-scale for each parameter, this problem has been detailed in Sec.5.3.1.

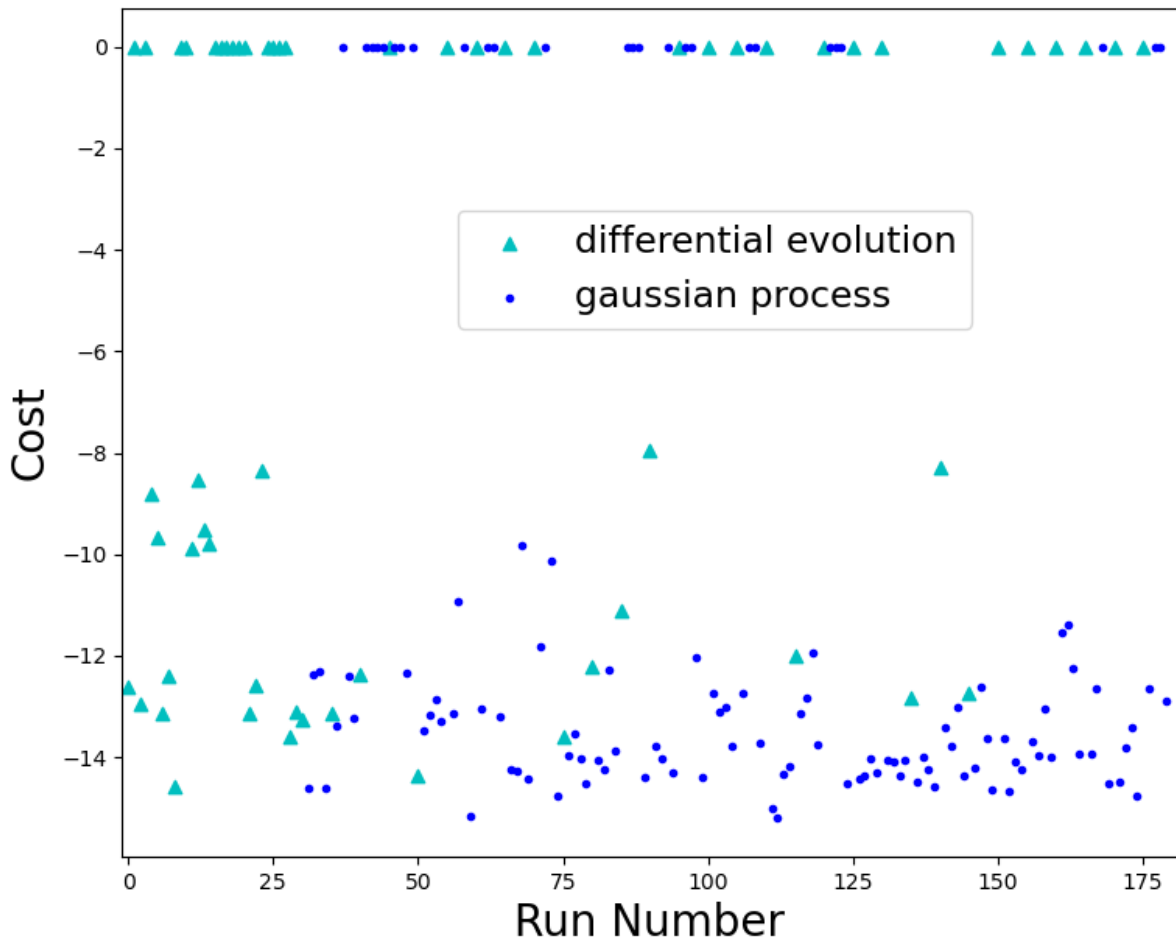


**Figure 5.6** — Graph displaying the evolution of the cost with respect to the Run number.

Once the thesis had been submitted, by changing the script used by Lyse to run MLOOP, I was able to run an optimization session for this problem with independent length-scale. This session of optimization led us to the graph presented in Fig.5.6 which shows the evolution of the cost with respect to the run number inside the optimization sequence. Each point represents an experimental sequence, and one can see that a point has two different colors: either purple or blue. These two colors refer to the kind of algorithm used to determine the cost evaluated: the cyan triangles represent the configuration determined with the differential evolution algorithm, whereas the blue dots are the configuration determined using the Gaussian process regression. The optimization session starts with the execution of 31 se-

variable name (unit)	Pre-optimization configuration	Post-optimization configuration	Length-scale (dimensionless)	$\Delta P_j$
PRepumpLow (relative output power)	0.1228	0.074211	0.127863	0 - 0.7
dtCool (ms)	0.01951	0.039006	0.174819	5 ms - 50 ms
MOTCompress (A)	96.72	74.971733	0.226653	23 A - 180 A
RapportBasHaut (dimensionless)	1.089	1.031691	0.352091	1.0 - 1.2
dtQuadMinOn (ms)	0.001153	0.005000	0.542579	0 ms - 10 ms
CompressPower (relative output power)	0.7493.	1.0	0.672400	0 - 1.0
dtSisyphus (ms)	0.005138	0.001	1.031072	1 ms - 10 ms
dtF1 (ms)	0.004565	0.001	10.0	1 ms - 10 ms
dtLowerRepump (ms)	0.000629	0.033553	10.0	0 ms - 50 ms
CompressFreq ( $\Gamma$ )	-5.11.	-8.0	10.0	$-8 \times \Gamma - 0 \times \Gamma$
MolassesFreq ( $\Gamma$ )	-20.1.	-10.0	10.0	$-30 \times \Gamma - -10 \times \Gamma$
SisyphusPower (relative output power)	0.8701	0.676249	10.0	0.5 - 1.0
IQuadMax (A)	336.6	355.706584	10.0	200 A - 390 A
dtCompress (ms)	0.00294	0.002	10.0	2 ms - 30 ms
dtQuadRamp (ms)	0.2545	0.219858	10.0	75 ms - 300 ms

**Table 5.2** – The variables optimized. For each of them, we give the starting value and the optimized value.

quences determined with the differential evolution algorithm as the initialization phase. The Gaussian process regression algorithm then determined the next configuration almost always: every fifth sequence, a configuration is determined using the differential evolution algorithm that is why there are cyan triangles after the training session. This session stopped because the maximum number of sequences had been reached for an optimization session (which was 180 sequences). The best situation discovered during this sequence was similar to the starting configuration (prior to degradation), with a configuration close to the discovered optimum. This allows for the different values to be compared to one another.

In the end, the different parameters have been ordered in increasing order in Tab.5.2: the lower the value, the more sensitive the parameter is determined to be, compared with the allowed range. Similarly to the value presented in Sec.5.3.1, the maximum value of a characteristic length-scale is 10, therefore all the parameters below dtSisyphus are deemed not sensitive at all. Also, the most sensitive parameters, PRepumpLow, dtCool and MOTCompress are the parameters of the molasses phase, indicating how sensitive this part of the sequence is.

Furthermore, the parameter `RapportBasHaut` is a correction applied to the down coil during the transport from the MOT chamber to the science cell. The differential tube is about 2 mm wide, it is therefore crucial to tune the cloud's height correctly during the transport phase.

To conclude the part on the pre-transport optimization phase, let me sum up the main elements we can draw from these experiments. First, when the configuration is altered by the experimentalist, MLOOP finds better configurations with lower costs than the initial configuration. Then, for a part of the sequence that had been optimized over the years, such as the pre-transport phase, MLOOP doesn't find a greatly superior configuration. Ultimately, using the Gaussian Process Regression algorithm with MLOOP gives an estimation of the sensitivity of each parameter through the characteristic length scale.

## 5.4 Conclusion on machine learning uses

In the laboratory, machine learning has been successfully implemented. It executes the desired optimization session, and hence, certain tasks could be partially automated, such as the dimple position adjustment. Ideally, the main algorithm used to execute machine learning optimization, the Gaussian regression process, provides information on the sensitivity of each parameter.

By performing an optimization of the pre-transport phase, no increase in the number of atoms was observed. This part of the sequence had already been optimized by the team in an efficient manner.

The use of the machine-learning algorithm was much more interesting on the newly implemented dimple hybrid trap. When transitioning from a plugged trap to a dimple trap, the optimization session has been programmed to optimize the transfer from the dimple trap to the dressed trap. In this way we improved the atom number loaded in the dressed trap by a factor of two. A further analysis of the two optimization runs we performed allow us to access the sensitivity of the sequence to the various parameters, which is interesting information for future improvements of the sequence and even of the setup. If we find that a parameter is especially sensitive, we can modify the setup in order to stabilize this parameter in the best possible way and reduce its noise, if any (power supplies, laser frequency stabilization, etc.).

# Conclusion

This manuscript shows the work done during my PhD in the BEC team of the LPL, which had a two-fold goal: on the one hand, the implementation of a new control system and the wise use of its new features; on the other hand, the study of gravity compensation on the laboratory experimental setup.

The main achievement in this manuscript is the implementation of a new control system, the Labscript Suite, which modified deeply the modus operandi deeply. All the information about an experimental sequence is now stored in a unique information vector: the HDF file. The graphic user interface enables the rapid change of numerical values of parameters, and some new features such as the randomized generation of shot files prevent certain biases from appearing on the set of data. With the execution of the instruction of the sequence on one hand and an interface to interact with the different devices on the other, some repetitive tasks such as the calibration of a new device or the scanning of a parameter are easier to do. The data analysis has been simplified and has become more versatile. The user may write some short script to a perform very specific task previously took longer to do, such as display the evolution of the number of atoms during a parameter scan. This new system has been fully implemented and works as intended, and the different options described previously help to greatly increase the setup productivity. As a comparison, with the previous control system, it took a day to execute 200 sequences, whereas for a similar task, these same sequences are done in less than 4 hours. Also, the time precision of the system has been improved, and our imaging pulses are sent directly using the output system. This simplifies the setup as it is no longer necessary to use dedicated devices to execute short pulses. The next step to improving the experiment is to increase the autonomy of the setup: when data are taken, the role of the experimentalist is to make sure nothing perturbs the execution of the measurements. Therefore, one must always check that the lasers are locked; otherwise, the atoms can no longer be trapped or imaged. This requires the full attention of the experimentalist and is exhausting when done all day long. A solution would be to implement a laser lock management system that can detect when a laser lock breaks and lock it back on the reference automatically.

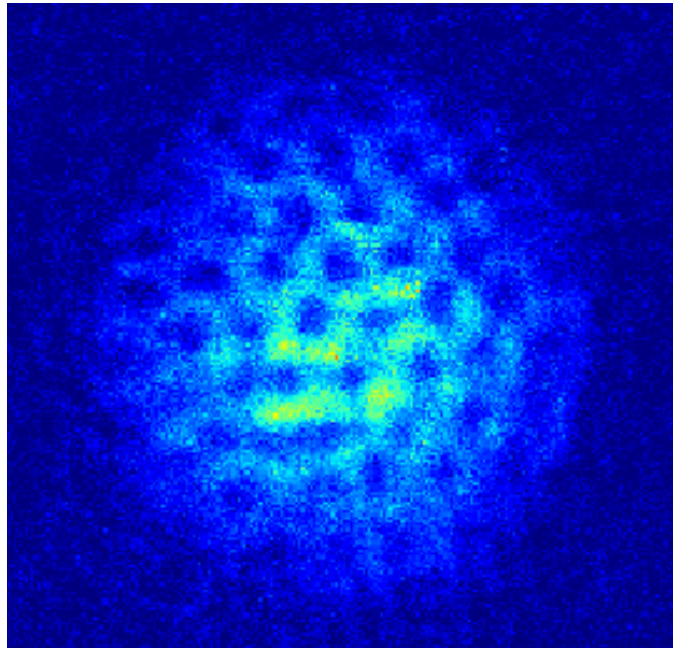
With the new control system, some machine-learning algorithms have been implemented. Thanks to the M-LOOP library, different optimizations on the experiment had been done in order to maximize the number of atoms at the end of the sequence. We tested this optimization on sequence part prior to the transport of the atom. No improvement was found in terms of the number of atoms, which indicates our setup was optimally tuned prior to the optimization session. These optimizations had also been done while implementing a new trapping solution

for the atom; the algorithm being used to optimize the atom transfer to the dressed trap. In such a situation, the machine-learning solution has been interesting. It increases by a factor of two the number of atoms in the dressed trap. Up until now, we did not make use of the ability to independently adjust the characteristic lengths of each parameter that we optimized. We plan to upgrade our program to implement this possibility in the near future, as it would allow the user to determine which parameters are the most sensitive during an optimization session. Even without this refinement, the machine-learning algorithm appears to be an efficient means to obtain information on a newly implemented devices. It has been useful in optimizing a certain part of our sequence, but a more comprehensive study can be done. This can be done by investigating other algorithms, such as neural networks, to do the same task and comparing the efficiency of the different algorithms. Finally, other uses of machine learning can be investigated. One of the critical aspects of our experiment is the absorption imaging technique, which is prone to certain types of imaging noise. Some algorithms have been tested to reduce the noise on the images and improve the quality of the imaging system in the setup [113].

On top of this technical improvement, I worked on a systematic study of gravity cancellation inside the quadrupole dressed trap. This work started during Yanliang Guo's PhD and continued through mine. Inside the trap, the atoms are pushed to the bottom of the bubble by gravity and feel an attraction towards the holes on top of the bubble. By increasing the attraction toward the zero of coupling, the gravity effects are cancelled. This was done for the atoms to spread on the whole surface of the bubble, but instead it was observed that the atoms spontaneously form a ring. This is due to the inhomogeneous transverse confinement. The ring shaped BEC has been observed during Yanliang Guo's PhD. While a qualitative interpretation was given, evidencing the role of the zero-point energy of the transverse motion, a quantitative comparison to the data remained to be done. To this aim, a numerical model has been developed by Romain Dubessy that takes into account terms beyond the rotating wave approximation. This model fit the data particularly well, as seen in Chap. 3. This enables us to look at the influence of a microgravity environment on a BEC inside a trap. As the micro-gravity environment for cold atoms is studied more and more with a scientific project such as the Cold Atom Lab (CAL) on the ISS [114], this result shows the influence a spatially inhomogeneous coupling has on a BEC. In fact, even for experiments in the microgravity of the ISS, it is necessary to take into account the variation of zero-point energy in the trap as it becomes the most important phenomenon inside the trap. A potential next step to investigate physics in a microgravity environment would be to set the ring shaped cloud into rotation. It is expected that a modification of the cloud topology would lead to a new vortex distribution when this cloud is set into rotation [29, 115].

Finally, I want to mention an experimental project I have been involved in: the study of vortex lattices in the Bose-Einstein condensate. This part of the work had not been mentioned in the PhD because the data are currently being analyzed. As presented in this manuscript, the Bose-Einstein condensate is a superfluid, and when it is set into rotation, instead of having rotating flow, some vortex appears inside the trap as presented in Chap.1. When they appear in the trap, they spontaneously form a lattice with a triangle-shaped cell in the trap with more or less disorder. Models to describe the behavior of the lattice had been studied extensively by theoreticians since the 1970s [18, 116]. It is predicted that a lattice with a triangular unit cell will be formed, and this lattice will be destroyed by the appearance of defects undergoing phase transition from the lattice, which has a translational order and a rotational order, to a hexatic phase, where the translational order is destroyed while the orientational order is

preserved. During this data acquisition period, we saw the appearance of the vortices at the bottom of the trap. A wide scan had been done over the parameters related to rotation and different situations were observed regarding the vortices: some pictures displayed well organized vortex lattice as can be seen in the figure below and in other cases the vortices were disorganized. These experiments had been the first ones done right after the Labscript Suite was implemented in the new setup. The goal is to perform a more systematic study of the vortex melting phenomenon that was observed qualitatively during the PhD of Mathieu de Goër [64]. The data are currently under analysis by the team, and a tentative comparison with existing models is ongoing.



An example of a vortex lattice obtained by rotating a trap deformation.



# Bibliography

- [1] C. J. PETHICK and H. SMITH, *Bose-Einstein Condensation in Dilute Gases*. Cambridge University Press, deuxième édition (2008).
- [2] LEV PITAEVSKII and SANDRO STRINGARI, *Bose-Einstein Condensation and Superfluidity*. Oxford University Press (jan 2016). <https://doi.org/10.1093%2Facprof%3Aoso%2F9780198758884.001.0001> .
- [3] P. KAPITZA, “Viscosity of Liquid Helium below the  $\lambda$ -Point”. *Nature* **141** (3558), 74–74 (Jan 1938).
- [4] J. F. ALLEN and A. D. MISENER, “Flow of Liquid Helium II”. *Nature* **141** (3558), 75–75 (Jan 1938).
- [5] F. LONDON, “On the Bose-Einstein Condensation”. *Phys. Rev.* **54**, 947–954 (Dec 1938).
- [6] KAMERLINGH ONNES H., “The superconductivity of mercury”. *Comm. Phys. Lab. Univ. Leiden* **122**, 122–124 (1911).
- [7] J. BARDEEN, L. N. COOPER and J. R. SCHRIEFFER, “Theory of Superconductivity”. *Phys. Rev.* **108**, 1175–1204 (Dec 1957).
- [8] CLAUDE N. COHEN-TANNOUJJI, “Nobel Lecture: Manipulating atoms with photons”. *Rev. Mod. Phys.* **70**, 707–719 (Jul 1998).
- [9] STEVEN CHU, “Nobel Lecture: The manipulation of neutral particles”. *Rev. Mod. Phys.* **70**, 685–706 (Jul 1998).
- [10] WILLIAM D. PHILLIPS, “Nobel Lecture: Laser cooling and trapping of neutral atoms”. *Rev. Mod. Phys.* **70**, 721–741 (Jul 1998).
- [11] WOLFGANG KETTERLE and N. J. VAN DRUTEN, “Evaporative Cooling of Trapped Atoms”. *Advances in Atomic Molecular and Optical Physics* **37**, 181–236 (janvier 1996).
- [12] M. H. ANDERSON, J. R. ENSHER, M. R. MATTHEWS, C. E. WIEMAN and E. A. CORNELL, “Observation of Bose-Einstein Condensation in a Dilute Atomic Vapor”. *Science* **269** (5221), 198–201 (1995).



- [13] K. B. DAVIS, M. O. MEWES, M. R. ANDREWS, N. J. VAN DRUTEN, D. S. DURFEE, D. M. KURN and W. KETTERLE, “Bose-Einstein Condensation in a Gas of Sodium Atoms”. *Phys. Rev. Lett.* **75**, 3969–3973 (Nov 1995).
- [14] K. W. MADISON, F. CHEVY, W. WOHLLEBEN and J. DALIBARD, “Vortex Formation in a Stirred Bose-Einstein Condensate”. *Phys. Rev. Lett.* **84**, 806–809 (Jan 2000).
- [15] J. R. ABO-SHAER, C. RAMAN, J. M. VOGELS and W. KETTERLE, “Observation of Vortex Lattices in Bose-Einstein Condensates”. *Science* **292** (5516), 476–479 (2001).
- [16] C. RAMAN, M. KÖHL, R. ONOFRIO, D. S. DURFEE, C. E. KUKLEWICZ, Z. HADZIBABIC and W. KETTERLE, “Evidence for a Critical Velocity in a Bose-Einstein Condensed Gas”. *Phys. Rev. Lett.* **83**, 2502–2505 (Sep 1999).
- [17] V. L. BEREZINSKIĬ, “Destruction of Long-range Order in One-dimensional and Two-dimensional Systems having a Continuous Symmetry Group I. Classical Systems”. *Soviet Journal of Experimental and Theoretical Physics* **32**, 493 (janvier 1971).
- [18] J M KOSTERLITZ and D J THOULESS, “Ordering, metastability and phase transitions in two-dimensional systems”. *Journal of Physics C: Solid State Physics* **6** (7), 1181–1203 (apr 1973).
- [19] Z. HADZIBABIC, P. KRÜGER, M. CHENEAU, B. BATTELIER and J. DALIBARD, “Berezinskii-Kosterlitz-Thouless crossover in a trapped atomic gas”. *Nature* **441**, 1118 (2006).
- [20] LAURENT SANCHEZ-PALENCIA, “Quantum simulation: From basic principles to applications: Foreword”. *Comptes Rendus Physique* **19** (6), 357–364 (2018). Quantum simulation / Simulation quantique.
- [21] MARKUS GREINER, OLAF MANDEL, TILMAN ESSLINGER, THEODOR W. HÄNSCH and IMMANUEL BLOCH, “Quantum phase transition from a superfluid to a Mott insulator in a gas of ultracold atoms”. *Nature* **415** (6867), 39–44 (Jan 2002).
- [22] T LAHAYE, C MENOTTI, L SANTOS, M LEWENSTEIN and T PFAU, “The physics of dipolar bosonic quantum gases”. *Reports on Progress in Physics* **72** (12), 126 401 (nov 2009).
- [23] L. CHOMAZ, D. PETTER, P. ILZHÖFER, G. NATALE, A. TRAUTMANN, C. POLITI, G. DURASTANTE, R. M. W. VAN BIJNEN, A. PATSCHEIDER, M. SOHMEN, M. J. MARK and F. FERLAINO, “Long-Lived and Transient Supersolid Behaviors in Dipolar Quantum Gases”. *Phys. Rev. X* **9**, 021 012 (Apr 2019).
- [24] D. R. YENNIE, “Integral quantum Hall effect for nonspecialists”. *Rev. Mod. Phys.* **59**, 781–824 (Jul 1987).
- [25] L. AMICO, M. BOSHIER, G. BIRKL, A. MINGUZZI, C. MINIATURA, L.-C. KWEK, D. AGHAMALYAN, V. AHUFINGER, D. ANDERSON, N. ANDREI, A. S. ARNOLD, M. BAKER, T. A. BELL, T. BLAND, J. P. BRANTUT, D. CASSETTARI, W. J. CHETCUTI, F. CHEVY, R. CITRO, S. DE PALO, R. DUMKE, M. EDWARDS, R. FOLMAN, J. FORTAGH, S. A. GARDINER, B. M. GARRAWAY, G. GAUTHIER, A. GÜNTHER, T. HAUG, C. HUFNAGEL, M. KEIL, P. IRELAND, M. LEBRAT,

- W. LI, L. LONGCHAMBON, J. MOMPART, O. MORSCH, P. NALDESI, T. W. NEELY, M. OLSHANI, E. ORIGNAC, S. PANDEY, A. PÉREZ-OBOL, H. PERRIN, L. PIROLI, J. POLO, A. L. PRITCHARD, N. P. PROUKAKIS, C. RYLANDS, H. RUBINSZTEIN-DUNLOP, F. SCAZZA, S. STRINGARI, F. TOSTO, A. TROMBETTONI, N. VICTORIN, W. VON KLITZING, D. WILKOWSKI, K. XHANI and A. YAKIMENKO, “Roadmap on Atomtronics: State of the art and perspective”. *AVS Quantum Science* **3** (3), 039 201 (2021). <https://doi.org/10.1116/5.0026178>.
- [26] C. RYU, P. W. BLACKBURN, A. A. BLINOVA and M. G. BOSHIER, “Experimental Realization of Josephson Junctions for an Atom SQUID”. *Phys. Rev. Lett.* **111**, 205 301 (Nov 2013).
- [27] NATÁLIA S MÓLLER, F EDNILSON A DOS SANTOS, VANDERLEI S BAGNATO and AXEL PELSTER, “Bose–Einstein condensation on curved manifolds”. *New Journal of Physics* **22** (6), 063 059 (jun 2020).
- [28] KUEI SUN, KARMELA PADAVIĆ, FRANCES YANG, SMITHA VISHVESHWARA and COURTNEY LANNERT, “Static and dynamic properties of shell-shaped condensates”. *Phys. Rev. A* **98**, 013 609 (Jul 2018).
- [29] KARMELA PADAVIĆ, KUEI SUN, COURTNEY LANNERT and SMITHA VISHVESHWARA, “Vortex-antivortex physics in shell-shaped Bose-Einstein condensates”. *Physical Review A* **102** (4) (oct 2020).
- [30] DAVID C. AVELINE, JASON R. WILLIAMS, ETHAN R. ELLIOTT, CHELSEA DUTENHOFFER, JAMES R. KELLOGG, JAMES M. KOHEL, NORMAN E. LAY, KAMAL OUDRHIRI, ROBERT F. SHOTWELL, NAN YU and ROBERT J. THOMPSON, “Observation of Bose–Einstein condensates in an Earth-orbiting research lab”. *Nature* **582** (7811), 193–197 (2020).
- [31] Y. COLOMBE, E. KNYAZCHYAN, O. MORIZOT, B. MERCIER, V. LORENT and H. PERRIN, “Ultracold atoms confined in rf-induced two-dimensional trapping potentials”. *Europhysics Letters* **67** (4), 593 (aug 2004).
- [32] KARINA MERLOTI, ROMAIN DUBESSY, LAURENT LONGCHAMBON, AURÉLIEN PERRIN, PAUL-ERIC POTTIE, VINCENT LORENT and HÉLÈNE PERRIN, “A two-dimensional quantum gas in a magnetic trap”. *New Journal of Physics* **15**, 033 007 (2013). 1303.2474.
- [33] HÉLÈNE PERRIN and BARRY M. GARRAWAY, “Trapping Atoms With Radio Frequency Adiabatic Potentials”. In *Advances In Atomic, Molecular, and Optical Physics* pages 181–262, Elsevier (2017).
- [34] R. DUBESSY, C. DE ROSSI, T. BADR, L. LONGCHAMBON and H. PERRIN, “Imaging the collective excitations of an ultracold gas using statistical correlations”. *New Journal of Physics* **16** (12), 122 001 (2014).
- [35] CAMILLA DE ROSSI, ROMAIN DUBESSY, KARINA MERLOTI, MATHIEU DE GOËR DE HERVE, THOMAS BADR, AURÉLIEN PERRIN, LAURENT LONGCHAMBON and HÉLÈNE PERRIN, “Probing superfluidity in a quasi two-dimensional Bose gas through its local dynamics”. *New Journal of Physics* **18** (6), 062 001 (jun 2016).

- [36] YANLIANG GUO, ROMAIN DUBESSY, MATHIEU DE GOËR DE HERVE, AVINASH KUMAR, THOMAS BADR, AURÉLIEN PERRIN, LAURENT LONGCHAMBON and HÉLÈNE PERRIN, “Supersonic Rotation of a Superfluid: A Long-Lived Dynamical Ring”. *Phys. Rev. Lett.* **124**, 025 301 (Jan 2020).
- [37] YANLIANG GUO, EMMANUEL MERCADO GUTIERREZ, DAVID REY, THOMAS BADR, AURÉLIEN PERRIN, LAURENT LONGCHAMBON, VANDERLEI SALVADOR BAGNATO, HÉLÈNE PERRIN and ROMAIN DUBESSY, “Expansion of a quantum gas in a shell trap”. *New Journal of Physics* (2022).
- [38] P. T. STARKEY, C. J. BILLINGTON, S. P. JOHNSTONE, M. JASPERSE, K. HELMERSON, L. D. TURNER and R. P. ANDERSON, “A scripted control system for autonomous hardware-timed experiments”. *Review of Scientific Instruments* **84** (8), 085 111 (aug 2013).
- [39] PETER E. GASKELL, JEREMY J. THORN, SEQUOIA ALBA and DANIEL A. STECK, “An open-source, extensible system for laboratory timing and control”. *Review of Scientific Instruments* **80** (11), 115 103 (2009).
- [40] ELIA PEREGO, MARCO POMPONIO, AMELIA DETTI, LUCIA DUCA, CARLO SIAS and CLAUDIO E. CALOSSO, “A scalable hardware and software control apparatus for experiments with hybrid quantum systems”. *Review of Scientific Instruments* **89** (11), 113 116 (2018).
- [41] MORITZ AUGUST and XIAOTONG NI, “Using recurrent neural networks to optimize dynamical decoupling for quantum memory”. *Phys. Rev. A* **95**, 012 335 (Jan 2017).
- [42] SANDESH S. KALANTRE, JUSTYNA P. ZWOLAK, STEPHEN RAGOLE, XINGYAO WU, NEIL M. ZIMMERMAN, M. D. STEWART and JACOB M. TAYLOR, “Machine learning techniques for state recognition and auto-tuning in quantum dots”. *npj Quantum Information* **5** (1), 6 (Jan 2019).
- [43] FLORENT LECLERCQ, “Bayesian optimization for likelihood-free cosmological inference”. *Phys. Rev. D* **98**, 063 511 (Sep 2018).
- [44] JOËL AKERET, ALEXANDRE REFREGIER, ADAM AMARA, SEBASTIAN SEEHARS and CASPAR HASNER, “Approximate Bayesian computation for forward modeling in cosmology”. *Journal of Cosmology and Astroparticle Physics* **2015** (08), 043–043 (aug 2015).
- [45] CHANGHOON HAHN, MOHAMMADJAVAD VAKILI, KILIAN WALSH, ANDREW P. HEARIN, DAVID W. HOGG and DUNCAN CAMPBELL, “Approximate Bayesian computation in large-scale structure: constraining the galaxy–halo connection”. *Monthly Notices of the Royal Astronomical Society* **469** (3), 2791–2805 (04 2017).
- [46] DANIEL S. KERMANY, MICHAEL GOLDBAUM, WENJIA CAI, CAROLINA C.S. VALENTIM, HUIYING LIANG, SALLY L. BAXTER, ALEX MCKEOWN, GE YANG, XIAOKANG WU, FANGBING YAN, JUSTIN DONG, MADE K. PRASADHA, JACQUELINE PEI, MAGDALENE Y.L. TING, JIE ZHU, CHRISTINA LI, SIERRA HEWETT, JASON DONG, IAN ZIYAR, ALEXANDER SHI, RUNZE ZHANG, LIANGHONG ZHENG, RUI HOU, WILLIAM SHI, XIN FU, YAOU DUAN, VIET A.N. HUU, CINDY WEN, EDWARD D. ZHANG, CHARLOTTE L. ZHANG, OULAN LI, XIAOBO WANG, MICHAEL A. SINGER,

- XIAODONG SUN, JIE XU, ALI TAFRESHI, M. ANTHONY LEWIS, HUIMIN XIA and KANG ZHANG, “Identifying Medical Diagnoses and Treatable Diseases by Image-Based Deep Learning”. *Cell* **172** (5), 1122–1131.e9 (2018).
- [47] W. ROHRINGER, D. FISCHER, M. TRUPKE, J. SCHMIEDMAYER and T. SCHUMM, “Stochastic Optimization of Bose-Einstein Condensation Using a Genetic Algorithm”. In *Stochastic Optimization*, edited by IOANNIS DRITSAS chapter 1, IntechOpen, Rijeka (2011).
- [48] A. D. TRANTER, H. J. SLATYER, M. R. HUSH, A. C. LEUNG, J. L. EVERETT, K. V. PAUL, P. VERNAZ-GRIS, P. K. LAM, B. C. BUCHLER and G. T. CAMPBELL, “Multiparameter optimisation of a magneto-optical trap using deep learning”. *Nature Communications* **9** (1), 4360 (Oct 2018).
- [49] ZACHARY VENDEIRO, JOSHUA RAMETTE, ALYSSA RUDELIS, MICHELLE CHONG, JOSIAH SINCLAIR, LUKE STEWART, ALBAN URVOY and VLADAN VULETIĆ, “Machine-learning-accelerated Bose-Einstein condensation” (2022). <https://arxiv.org/abs/2205.08057> .
- [50] EMINE ALTUNTAŞ and I. B. SPIELMAN, “Self-Bayesian aberration removal via constraints for ultracold atom microscopy”. *Phys. Rev. Research* **3**, 043087 (Oct 2021).
- [51] AXEL U. J. LODE, RUI LIN, MIRIAM BÜTTNER, LUCA PAPARIELLO, CAMILLE LÉVÊQUE, R. CHITRA, MARIOS C. TSATSOS, DIETER JAKSCH and PAOLO MOLIGNINI, “Optimized observable readout from single-shot images of ultracold atoms via machine learning”. *Phys. Rev. A* **104**, L041301 (Oct 2021).
- [52] D. ZEIDLER, S. FREY, K.-L. KOMPA and M. MOTZKUS, “Evolutionary algorithms and their application to optimal control studies”. *Phys. Rev. A* **64**, 023420 (Jul 2001).
- [53] A J BARKER, H STYLE, K LUKSCH, S SUNAMI, D GARRICK, F HILL, C J FOOT and E BENTINE, “Applying machine learning optimization methods to the production of a quantum gas”. *Machine Learning: Science and Technology* **1** (1), 015007 (feb 2020).
- [54] O. ZOBAY and B. M. GARRAWAY, “Two-Dimensional Atom Trapping in Field-Induced Adiabatic Potentials”. *Physical Review Letters* **86** (7), 1195–1198 (2001).
- [55] Y COLOMBE, E KNYAZCHYAN, O MORIZOT, B MERCIER, V LORENT and H PERRIN, “Ultracold atoms confined in rf-induced two-dimensional trapping potentials”. *Europhysics Letters (EPL)* **67** (4), 593–599 (aug 2004).
- [56] T. SCHUMM, S. HOFFERBERTH, L. M. ANDERSSON, S. WILDERMUTH, S. GROTH, I. BAR-JOSEPH, J. SCHMIEDMAYER and P. KRÜGER, “Matter-wave interferometry in a double well on an atom chip”. *Nature Physics* **1** (1), 57–62 (sep 2005).
- [57] OLIVIER MORIZOT, YVES COLOMBE, VINCENT LORENT, HÉLÈNE PERRIN and BARRY M. GARRAWAY, “Ring trap for ultracold atoms”. *Physical Review A* **74** (2) (aug 2006).
- [58] W H HEATHCOTE, E NUGENT, B T SHEARD and C J FOOT, “A ring trap for ultracold atoms in an RF-dressed state”. *New Journal of Physics* **10** (4), 043012 (apr 2008).

- [59] PH W COURTEILLE, B DEH, J FORTÁGH, A GÜNTHER, S KRAFT, C MARZOK, S SLAMA and C ZIMMERMANN, “Highly versatile atomic micro traps generated by multifrequency magnetic field modulation”. *Journal of Physics B: Atomic, Molecular and Optical Physics* **39** (5), 1055–1064 (feb 2006).
- [60] N. LUNDBLAD, P. J. LEE, I. B. SPIELMAN, B. L. BROWN, W. D. PHILLIPS and J. V. PORTO, “Atoms in a Radio-Frequency-Dressed Optical Lattice”. *Physical Review Letters* **100** (15) (2008).
- [61] HÉLÈNE PERRIN, “Spins and field - lecture 1 - Les Houches lectures on adiabatic potentials” (September 2013). [http://www-lpl.univ-paris13.fr/bec/bec/Teaching/lecture1\\_2013.pdf](http://www-lpl.univ-paris13.fr/bec/bec/Teaching/lecture1_2013.pdf) .
- [62] C. COHEN-TANNOUJJI, “Atomes ultrafroids - Piègeage non dissipatif et refroidissement évaporatif” (1996). <http://www.phys.ens.fr/~cct/college-de-france/1996-97/1996-97.htm> .
- [63] HÉLÈNE PERRIN, “Adiabatic Potentials - lecture 2 - Les Houches lectures on adiabatic potentials” (September 2013). [http://www-lpl.univ-paris13.fr/bec/bec/Teaching/lecture2\\_2013.pdf](http://www-lpl.univ-paris13.fr/bec/bec/Teaching/lecture2_2013.pdf) .
- [64] MATHIEU DE GOËR DE HERVE, *Superfluid dynamics of annular Bose gases*. Theses, Université Sorbonne Paris Cité (octobre 2018).
- [65] FRANCO DALFOVO, STEFANO GIORGINI, LEV P. PITAEVSKII and SANDRO STRINGARI, “Theory of Bose-Einstein condensation in trapped gases”. *Reviews of Modern Physics* **71** (3), 463–512 (1999).
- [66] S. STRINGARI, “Collective Excitations of a Trapped Bose-Condensed Gas”. *Physical Review Letters* **77** (12), 2360–2363 (1996).
- [67] L.D. LANDAU, “46 - THE THEORY OF SUPERFLUIDITY OF HELIUM II”. In *Collected Papers of L.D. Landau*, edited by D. TER HAAR pages 301–330, Pergamon (1965).
- [68] V. L. BEREZINSKY, “Destruction of long range order in one-dimensional and two-dimensional systems having a continuous symmetry group. II. Quantum Systems”. *Sov. Phys. JETP* **32**, 34–610 (1971).
- [69] NIKOLAY PROKOF’EV, OLIVER RUEBENACKER and BORIS SVISTUNOV, “Critical Point of a Weakly Interacting Two-Dimensional Bose Gas”. *Phys. Rev. Lett.* **87**, 270 402 (Dec 2001).
- [70] D. S. PETROV, D. M. GANGARDT and G. V. SHLYAPNIKOV, “Low-dimensional trapped gases”. *Journal de Physique IV (Proceedings)* **116**, 5–44 (oct 2004).
- [71] J. HADZIBABIC, Z. AND DALIBARD, “Two-dimensional Bose fluids: An atomic physics perspective”. *Rivista del Nuovo Cimento della Societa Italiana di Fisica* **34** (6), 389–434 (2011). CONDENSED MATTER PHYSICS, SUPERCONDUCTIVITY AND SUPERFLUIDITY.
- [72] MARKUS HOLZMANN, “Universal correlations and coherence in quasi-two-dimensional trapped Bose gases”. *Physical Review A* **81** (4) (2010).

- [73] THOMAS LIENNARD, *Construction d'un montage de condensation de Bose-Einstein de rubidium et étude théorique d'un superfluide en rotation dans un anneau*. Theses, Université Paris-Nord - Paris XIII (décembre 2011).
- [74] KARINA MERLOTI, *Condensat de Bose-Einstein dans un piège habillé: modes collectifs d'un superfluide en dimension deux*. Theses, Université Paris-Nord - Paris XIII (décembre 2013).
- [75] CAMILLA DE ROSSI, *Gaz de Bose en dimension deux : modes collectifs, superfluidité et piège annulaire*. Theses, Laboratoire de Physique des Lasers, Université Paris 13 (novembre 2016).
- [76] YANLIANG GUO, *Annular quantum gases in a bubble-shaped trap: from equilibrium to strong rotations*. Theses, Université Sorbonne Paris Nord (janvier 2021).
- [77] P. A. ALTIN, G. R. DENNIS, G. D. McDONALD, D. DÖRING, J. E. DEBS, J. D. CLOSE, C. M. SAVAGE and N. P. ROBINS, "Collapse and three-body loss in a  $^{85}\text{Rb}$  Bose-Einstein condensate". *Phys. Rev. A* **84**, 033 632 (Sep 2011).
- [78] M. H. ANDERSON, J. R. ENSHER, M. R. MATTHEWS, C. E. WIEMAN and E. A. CORNELL, "Observation of Bose-Einstein Condensation in a Dilute Atomic Vapor". *Science* **269** (5221), 198–201 (juillet 1995).
- [79] D. A. STECK, "Rubidium 87 D-line Data". available online at <http://steck.us/alkalidata> ( Version 2.2.2, last revised 9 July 2021).
- [80] ROMAIN DUBESSY, KARINA MERLOTI, LAURENT LONGCHAMBON, PAUL-ERIC POTTIE, THOMAS LIENNARD, AURÉLIEN PERRIN, VINCENT LORENT and HÉLÈNE PERRIN, "Rubidium-87 Bose-Einstein condensate in an optically plugged quadrupole trap". *Physical Review A* **85**, 1, 013 643 (2012). 1112.0660.
- [81] ETTORE MAJORANA, "Atomi orientati in campo magnetico variabile". *Il Nuovo Cimento* **9** (2), 43–50 (feb 1932).
- [82] LAURIANE CHOMAZ, *Coherence and superfluidity of Bose gases in reduced dimensions : from harmonic traps to uniform fluids*. Theses, Ecole normale supérieure - ENS PARIS (novembre 2014).
- [83] ETHAN R. ELLIOTT, MARKUS C. KRUTZIK, JASON R. WILLIAMS, ROBERT J. THOMPSON and DAVID C. AVELINE, "NASA's Cold Atom Lab (CAL): system development and ground test status". *npj Microgravity* **4** (1) (aug 2018).
- [84] HUBERT AMMANN and NELSON CHRISTENSEN, "Delta Kick Cooling: A New Method for Cooling Atoms". *Physical Review Letters* **78** (11), 2088–2091 (1997).
- [85] R. A. CAROLLO, D. C. AVELINE, B. RHYNO, S. VISHVESHWARA, C. LANNERT, J. D. MURPHREE, E. R. ELLIOTT, J. R. WILLIAMS, R. J. THOMPSON and N. LUNDBLAD, "Observation of ultracold atomic bubbles in orbital microgravity". *Nature* **606** (7913), 281–286 (may 2022).
- [86] KARMELA PADAVIĆ, KUEI SUN, COURTNEY LANNERT and SMITHA VISHVESHWARA, "Vortex-antivortex physics in shell-shaped Bose-Einstein condensates". *Phys. Rev. A* **102**, 043 305 (Oct 2020).

- [87] H. MÜNTINGA, H. AHLERS, M. KRUTZIK, A. WENZLAWSKI<sup>4</sup>, S. ARNOLD, D. BECKER, K. BONGS, H. DITTUS, H. DUNCKER, N. GAALLOUL, C. GHERASIM, E. GIESE, C. GRZESCHIK, T. W. HÄNSCH, O. HELLMIG, W. HERR, S. HERRMANN, E. KAJARI, S. KLEINERT, C. LÄMMERZAHN, W. LEWOCZKO-ADAMCZYK, J. MALCOLM, N. MEYER, R. NOLTE, A. PETERS, M. POPP, J. REICHEL, A. ROURA, J. RUDOLPH, M. SCHIEMANGK, M. SCHNEIDER, S. T. SEIDEL, K. SENGSTOCK, V. TAMMA, T. VALENZUELA, A. VOGEL, R. WALSER, T. WENDRICH, P. WINDPASSINGER, W. ZELLER, T. VAN ZOEST, W. ERTMER, W. P. SCHLEICH and E. M. RASEL, “Interferometry with Bose-Einstein Condensates in Microgravity”. *Physical Review Letters* **110** (9) (2013).
- [88] KOSUKE SHIBATA, HIDEHIKO IKEDA, RYOTA SUZUKI and TAKUYA HIRANO, “Compensation of gravity on cold atoms by a linear optical potential”. *Physical Review Research* **2** (1) (2020).
- [89] O. ZOBAY and B. M. GARRAWAY, “Atom trapping and two-dimensional Bose-Einstein condensates in field-induced adiabatic potentials”. *Phys. Rev. A* **69**, 023 605 (Feb 2004).
- [90] A. E. LEANHARDT, T. A. PASQUINI, M. SABA, A. SCHIROTZEK, Y. SHIN, D. KIELPINSKI, D. E. PRITCHARD and W. KETTERLE, “Cooling Bose-Einstein Condensates Below 500 Picokelvin”. *Science* **301** (5639), 1513–1515 (2003).
- [91] MATHIEU DE GOËR DE HERVE, YANLIANG GUO, CAMILLA DE ROSSI, AVINASH KUMAR, THOMAS BADR, ROMAIN DUBESSY, LAURENT LONGCHAMBON and HÉLÈNE PERRIN, “A versatile ring trap for quantum gases”. *Journal of Physics B: Atomic, Molecular and Optical Physics* **54** (12), 125 302 (jun 2021).
- [92] KATHRYN A. BURROWS, HÉLÈNE PERRIN and BARRY M. GARRAWAY, “Nonadiabatic losses from radio-frequency-dressed cold-atom traps: Beyond the Landau-Zener model”. *Physical Review A* **96** (2) (2017).
- [93] AVIV KESHET and WOLFGANG KETTERLE, “A distributed, graphical user interface based, computer control system for atomic physics experiments”. *Review of Scientific Instruments* **84** (1), 015 105 (2013). <https://doi.org/10.1063/1.4773536>.
- [94] SÉBASTIEN BOURDEAUDUCQ, ROBERT JÖRDENS, PETER ZOTOV, JOE BRITTON, DANIEL SLICHTER, DAVID LEIBRANDT, DAVID ALLCOCK, AARON HANKIN, FLORENT KERMARREC, YANN SIONNEAU, RAGHAVENDRA SRINIVAS, TING REI TAN and JUSTIN BOHNET, “ARTIQ 1.0” (mai 2016). <https://doi.org/10.5281/zenodo.51303>.
- [95] CHRISTOPHER JAMES BILLINGTON, *State-dependent forces in cold quantum gases*. PhD thesis, Monash University (4 2019).
- [96] PHILIP THOMAS STARKEY, *A software framework for control and automation of precisely timed experiments*. PhD thesis, Monash University (7 2019).
- [97] CHARLES R. HARRIS, K. JARROD MILLMAN, STÉFAN J. VAN DER WALT, RALF GOMMERS, PAULI VIRTANEN, DAVID COURNAPEAU, ERIC WIESER, JULIAN TAYLOR, SEBASTIAN BERG, NATHANIEL J. SMITH, ROBERT KERN, MATTI PICUS, STEPHAN HOYER, MARTEN H. VAN KERKWIJK, MATTHEW BRETT, ALLAN HALDANE,

- JAIME FERNÁNDEZ DEL RÍO, MARK WIEBE, PEARU PETERSON, PIERRE GÉRARD-MARCHANT, KEVIN SHEPPARD, TYLER REDDY, WARREN WECKESSER, HAMEER ABBASI, CHRISTOPH GOHLKE and TRAVIS E. OLIPHANT, “Array programming with NumPy”. *Nature* **585** (7825), 357–362 (septembre 2020).
- [98] PAULI VIRTANEN, RALF GOMMERS, TRAVIS E. OLIPHANT, MATT HABERLAND, TYLER REDDY, DAVID COURNAPEAU, EVGENI BUROVSKI, PEARU PETERSON, WARREN WECKESSER, JONATHAN BRIGHT, STÉFAN J. VAN DER WALT, MATTHEW BRETT, JOSHUA WILSON, K. JARROD MILLMAN, NIKOLAY MAYOROV, ANDREW R. J. NELSON, ERIC JONES, ROBERT KERN, ERIC LARSON, C J CAREY, ÍLHAN POLAT, YU FENG, ERIC W. MOORE, JAKE VANDERPLAS, DENIS LAXALDE, JOSEF PERKTOLD, ROBERT CIMRMAN, IAN HENRIKSEN, E. A. QUINTERO, CHARLES R. HARRIS, ANNE M. ARCHIBALD, ANTÓNIO H. RIBEIRO, FABIAN PEDREGOSA, PAUL VAN MULBREGT and SCI-PY 1.0 CONTRIBUTORS, “SciPy 1.0: Fundamental Algorithms for Scientific Computing in Python”. *Nature Methods* **17**, 261–272 (2020).
- [99] J. D. HUNTER, “Matplotlib: A 2D graphics environment”. *Computing in Science & Engineering* **9** (3), 90–95 (2007).
- [100] P. T. STARKEY and C. J. BILLINGTON, “Pseudoclock - github repository”.
- [101] C. F. OCKELOEN, A. F. TAUSCHINSKY, R. J. C. SPREEUW and S. WHITLOCK, “Detection of small atom numbers through image processing”. *Physical Review A* **82** (6) (dec 2010).
- [102] ZACHARY VENDEIRO, JOSHUA RAMETTE, ALYSSA RUDELIS, MICHELLE CHONG, JOSIAH SINCLAIR, LUKE STEWART, ALBAN URVOY and VLADAN VULETIĆ, “Machine-learning-accelerated Bose-Einstein condensation” (2022). <https://arxiv.org/abs/2205.08057> .
- [103] FLORENT LECLERCQ, “Bayesian optimization for likelihood-free cosmological inference”. *Physical Review D* **98** (6) (2018).
- [104] P. B. WIGLEY, P. J. EVERITT, A. VAN DEN HENGEL, J. W. BASTIAN, M. A. SOORIYABANDARA, G. D. McDONALD, K. S. HARDMAN, C. D. QUINLIVAN, P. MANJU, C. C. N. KUHN, I. R. PETERSEN, A. N. LUITEN, J. J. HOPE, N. P. ROBINS and M. R. HUSH, “Fast machine-learning online optimization of ultra-cold-atom experiments”. *Scientific Reports* **6** (1) (may 2016).
- [105] PATRICK JAILLET and MICHAEL R. WAGNER, *Online Optimization*. Springer Publishing Company, Incorporated (2012).
- [106] R. P. ANDERSON, “Analysislib - MLOOP github repository”.
- [107] RAINER STORN and KENNETH PRICE, “Differential Evolution – A Simple and Efficient Heuristic for Global Optimization over Continuous Spaces”. *J. of Global Optimization* **11** (4), 341–359 (dec 1997).
- [108] CARL EDWARD RASMUSSEN and CHRISTOPHER K. I. WILLIAMS, *Gaussian processes for machine learning.*, pages I–XVIII, 1–248. Adaptive computation and machine learning, MIT Press (2006).



- 
- [109] JIE WANG, “An Intuitive Tutorial to Gaussian Processes Regression” (2020). <https://arxiv.org/abs/2009.10862> .
- [110] RICHARD VON MISES, “CHAPTER IX - ANALYSIS OF STATISTICAL DATA”. In *Mathematical Theory of Probability and Statistics*, edited by RICHARD VON MISES pages 431–493, Academic Press (1964).
- [111] ERIC BROCHU, VLAD M. CORA and NANDO DE FREITAS, “A Tutorial on Bayesian Optimization of Expensive Cost Functions, with Application to Active User Modeling and Hierarchical Reinforcement Learning” (2010). <https://arxiv.org/abs/1012.2599> .
- [112] Y. CASTIN and R. DUM, “Bose-Einstein Condensates in Time Dependent Traps”. *Physical Review Letters* **77** (27), 5315–5319 (1996).
- [113] GAOYI LEI, CHENCHENG TANG and YUEYANG ZHAI, “Fringe removal algorithms for atomic absorption images: A survey”. *Chinese Physics B* **31** (5), 050 313 (may 2022).
- [114] N. LUNDBLAD, R. A. CAROLLO, C. LANNERT, M. J. GOLD, X. JIANG, D. PASELTINER, N. SERGAY and D. C. AVELINE, “Shell potentials for microgravity Bose–Einstein condensates”. *npj Microgravity* **5** (1) (dec 2019).
- [115] LEONARDO BRITO, ALEX ANDRIATI, LAURO TOMIO and ARNALDO GAMMAL, “Breakup of rotating asymmetric quartic-quadratic trapped condensates”. *Phys. Rev. A* **102**, 063 330 (Dec 2020).
- [116] B. I. HALPERIN and DAVID R. NELSON, “Theory of Two-Dimensional Melting”. *Phys. Rev. Lett.* **41**, 121–124 (Jul 1978).

## Résumé

Dans cette thèse est présentée l'implémentation d'un système de contrôle d'une expérience d'atomes ultra-froids. Celui-ci permet d'accélérer l'acquisition de données et d'utiliser des algorithmes d'apprentissage automatique pour optimiser le fonctionnement de l'expérience. Les caractéristiques du nouveau système sont présentées ainsi que la suite logicielle permettant le contrôle et l'analyse des données. Les différents algorithmes utilisés sont décrits ainsi que les premiers résultats d'optimisation obtenus. Dans l'expérience, un condensat de Bose-Einstein de gaz d'atomes de rubidium est confiné à la surface d'un ellipsoïde de révolution. Cette géométrie originale de piégeage provient de l'habillage des atomes par un champ radiofréquence dans un piège quadrupolaire magnétique.

Dans cette géométrie il est possible de compenser l'effet de la gravité, et je présente les résultats expérimentaux obtenus. Nous observons la formation spontanée d'un anneau condensé proche de l'équateur de la bulle, et nous interprétons ce comportement par un effet de l'énergie de point zéro du confinement transverse. Un modèle plus élaboré nécessitant l'introduction de termes au-delà de l'approximation de l'onde tournante est comparé aux données expérimentales.

**Mots-clefs :** Condensation de Bose-Einstein, potentiel adiabatique, microgravité, système de contrôle, Labscript Suite, optimisation, apprentissage automatique

## Abstract

This thesis presents the implementation of a control system for an ultra-cold atom experiment. This system allows for the acceleration of data acquisition and the use of machine learning algorithms to optimize the operation of the experiment. The characteristics of the new system are presented, as well as the software suite allowing the control and analysis of the data. The different algorithms used are described, as well as the first optimization results obtained. In the experiment, a Bose-Einstein condensate of rubidium atoms is confined to the surface of an ellipsoid of revolution. This original trapping geometry comes from the dressing of the atoms by a radiofrequency field in a magnetic quadrupole trap.

In this geometry, it is possible to compensate for the effect of gravity, and I present the experimental results obtained. We observe the spontaneous formation of a condensed ring near the equator of the bubble, and we interpret this behavior as an effect of the zero point energy of the transverse confinement. A more elaborate model requiring the introduction of terms beyond the rotating wave approximation is compared to the experimental data.

**Keywords:** Bose-Einstein condensation, adiabatic potential, radiofrequency dressed atoms, microgravity, control system, Labscript Suite, optimization, machine learning